Université Pierre et Marie Curie
Universita' della Calabria

Ecole doctorale 38PM
Ecole doctorale « Physique et Chimie des Materiaux »

Dipartimento di Fisica, Universita' della Calabria,
Institute des Nano Sciences de Paris

Auto-assemblage de défauts structurels et de nano-objets dans des films cristaux liquides

Self-assembly of structural defects and nano-objects in liquid crystal films

Par: Iryna Gryn

Thèse de doctorat de physique

Dirigée par M. Bruno Zappone et Mme. Emmanuelle Lacaze

Présentée et soutenue publiquement le 21 décembre 2015

Devant un jury composé de :
Zappone, Bruno (directeur de thèse)
Lacaze, Emmanuelle, (co-directrice de thèse)
Carbone, Luigi
Bellini, Tommaso
Bramati, Alberto
Blach, Jean François (Rapporteur)
Doru, Constantin (Rapporteur)

UNIVERSITÀ DELLA CALABRIA

UNIVERSITA' DELLA CALABRIA

Dipartimento di Fisica

Scuola di Dottorato

Scienza e Tecnica Bernardino Telesio

Indirizzo

Fisica

Con il contributo di

Univeristé Pierre et Marie Curie, Paris (France)

Co-supervisore: Prof.ssa Emmanuelle Lacaze

CICLO

XXVII

SELF-ASSEMBLY OF STRUCTURAL DEFECTS AND NANO-OBJECTS IN LIQUID CRYSTAL FILMS

Settore Scientifico Disciplinare: **FIS/07 Fisica Applicata**

Direttore: Ch.mo Prof. Roberto Bartolino

Firma _____

Supervisore: Dr. Bruno Zappone

Firma _____

Dottorando: Dott.ssa Iryna Gryn

Firma _____

Acknowledgments

Here I would like to express my great appreciation to the people, whose contribution made this thesis possible. First of all I would like to thank my supervisor Dr. Bruno Zappone for his continuous assistance, for all fruitful discussions and for his patient encouragement to my development as a scientist. His intellectual support throughout my study and research allowed me to overcome a lot of challenging problems and successfully cope with formulated research directions. The completion of this thesis would not have been possible without his generous efforts.

I greatly appreciate my co-supervisor Prof. Emmanuelle Lacaze for her vast knowledge and skills in many areas, assistance at all levels of my research. She introduced me into the field of X-ray diffraction, Plasmon resonance, dark-field microscopy and so on. Without her contribution in analysis of the data, discussions and interpreting of the results I may not have ever pursued this challenging area of physics. Working in the Institute des Nano-Sciences de Paris under her supervision significantly enriched my experience and I owe her my sincere gratitude.

I am also very grateful to all people who were involved in my scientific activity, especially to O. Marchenko for his teaching me the first knowledge about liquid crystals and supporting during the entering to the graduate school. Many thanks also go to Maria. P. De Santo and Gia Petriashvili for the help with spectrometer measurements and fruitful discussions; Michele Giokondo and Tiziana Ritacco for supporting me with confocal fluorescent microscopy and nanoscribe facilities; Pasquale Pagliusi for providing OTS and helping with the polarizing optical microscopy; Carlo Versace for the help with ITO sputtering; Michel Goldman and Denis Limagne for instructing me about X-ray diffraction, setup installation and its following exploitation; Olivier Plucheri for his help with LSPR measurements. Your collaboration with me was my pleasure and honor. I sincerely hope to have a chance to collaborate with you in my future research career.

The most of all I would like to thank my family for the support they provided me through my entire life. During all this years your advises and personal examples were the most important driving force for me. Thank you for your love, for the understanding and for the patience.

At last but not least I would like to thank for the financial support of my research activity provided by PhD scholarship from Graduate School “Bernardino Telesio”, Joint French-Italian PhD program (Cotutela) with the Université Pierre et Marie Curie and Eiffel excellence scholarship program.

Fall 2015 Iryna Gryn

Index

Introduction

The development of nanotechnology over the last decades has drawn the attention of both scientists and engineers to the self-assembly of matter into ordered structures at micro- and nanometer scales. The term "self-assembly" is used to describe the phenomenon of spontaneous organization of particles or building blocks into larger structures and patterns via specific interactions. Self-assembly is an equilibrium thermodynamic process where a balance is established between repulsive and attractive forces, and the free energy of the assembled system is lower than that of the random structure[1].

Self-assembly of small units into large-scale functional structures is one of the defining features of biological systems: collagen proteins are assembled in long robust fibers in bones and cartilage, lipids form bilayers in vesicles, cell membranes and myelin sheaths, and mineral particles combine with proteins to form the bright opalescent coating of sea shell, keratin can self-assemble into hair, DNA and viruses can spontaneously fold into functional 3D structures of complex topology[2-4]. The vast majority of biological systems, like for instance, single cells or tendons also exhibit hierarchy[5,6], that is the ability to generate ordered structures over multiple length scales and, in principle, multiple contributions to properties. This natural phenomenon has stimulated researchers to fabricate synthetic hierarchical materials mimicking natural analogies.

Self-assembly and the ability to generate order from the "bottom up" (i.e from building blocks to large-scale structures) is in contrast with the traditional approach to the fabrication of micro- and nano-structured materials and devices. In the "top-down" approach, nano- objects are either individually manipulated or organized using ordered matrices and hosts that are microfabricated. Lithographic methods, such as ultraviolet, X-ray, zone-plate array lithography, ion and electron beam lithography are commonly used to create sub-micron size 1D or 2D reliefs[7-10]. 3D photonic crystals can be produced by interference lithography[11]. Scanning probe microscopy such as atomic force microscope (AFM) or scanning tunneling microscope (STM) are used to fabricate patterns with smaller units[12], approaching the atomic level resolution[13]. A (5–50) nm resolution can be achieved by nanografting, dip-pen and nano imprint techniques[14].

Although lithography provide a high precision in nanoscale fabrication, it is time-consuming and expensive in terms of equipment and specialized personnel. On the other hand, the self-assembly "bottom-up" fabrication is typically achieved using standard bench-top equipment and inexpensive organic materials, can be a quite rapid and sometimes reversible process. The inherent capacity to self-assemble into nanostructures is exhibited by many soft materials, including colloids[15-17], surfactants[18-21], membranes[22-25], biomaterials[26-28], polymers[29-32], their composites[33,34] and liquid crystals (LC)[35-39]. The thermodynamic stability of self-assembled soft materials is typically based on weak molecular interactions[40], such as van der Waals interaction, dipolar and quadruple interactions, hydrogen bonding and electrostatic interactions, which can also be often find in living systems[41]. The weak nature of interactions results in flexibility of the formed systems, allowing rearrangements of the structures in response to small perturbations or stimuli imposed by the external environment. The latter feature is of the great interest from both fundamental and application standpoints, giving a possibility to control the assembly process and thus properties of created structures by varying external parameters.

The thermodynamics of the self-assembly process can be described at constant temperature T and pressure by a Gibbs free energy equation: $\Delta G = \Delta H - T\Delta S$. The enthalpy change ΔH is mainly determined by intermolecular interactions between the structural parts of assembling system, and ΔS is due to the appearance of order, i.e. a decrease of symmetry changes in ordered structure formation. The self-assembly is spontaneous in the sense that ΔG is negative[42]. Small structural units will nucleate and grow and their life-time increase as they minimize the system free energy via increasing attractive forces between the units, till the equilibrium state is achieved and the nanoordered structure is formed.

From the fundamental point of view liquid crystals (LCs) are representative materials for investigating self-assembly processes in soft matters. Their structural architecture resembles many biological objects, such as proteins, viruses, lipids, fibers, amyloids, carbohydrates and nucleic acids[41]. LCs show spontaneous breaking of symmetry and topological defects in close analogy with phenomena studied in cosmology, fundamental particle theories and condense matter physics[43]. The molecular organization and symmetry of LC phases strongly depends on the temperature or concentration,

respectively for thermotropic and lyotropic LCs[44]. As the temperature of a thermotropic LC is decreased, the symmetry of the material varies from the continuous orientational and transitional symmetry of isotropic liquids to discrete crystalline symmetry, passing through various "mesophases" with intermediate symmetries. A mesophase spontaneously breaks one or more symmetries of the phase at lower temperature. Symmetry breaking can be described by introducing an order parameter and is characterized by the appearance of topological defects - points, lines and surfaces – where order id deeply altered or removed[42]. The observation of defect formation and evolution in LCs provides theoretical and optical models for numbers of existing systems, from elementary particles to small biological cells and viruses. It is believed that symmetry breaking occurred in the early universe and defects such as strings, vortex lines and walls were formed, seeding the giant objects of today's universe[43].

From a technological point of view, it is hard to imagine the modern world without LCs. Since their discovery in 1888 by Friedrich Reinitzer and the invention of the twisted nematic field-effect in 1970 by George H. Heilmeier[45], LCs have become part of our daily life, being widely utilized in technological devices, such as thin flat displays, digital watches, calculators, smart windows, thermometers, various sensors and solar cells[46-51]. LCs are also used for optical imaging and recording[52], in optical fibers[53-57], in photonic integrated circuits[58,59] and as lasing media[60-62].

The popularity of LCs is due to the anisotropy of their optical, electromagnetic and mechanical properties and thus anisotropic respond of the materials. LC are made of anisometric molecules that show positional and orientational order. Molecules can be aligned along specific directions using suitable boundary conditions and external fields. Therefore, for instance, a typical LC display works on the principle of blocking light, exploiting a possibility to reorient LC molecules by electric field. A display consists of many small panels (pixels) and each pixel includes a twisted LC sandwiched between two polarized plates coated with transparent electrodes and oriented in a way that polarized light can pass through it. An electric field application to a particular pixel makes LC molecules to align with a field (to untwist), so that the light will not be able to pass and the area will become dark compared to others[44,63].

In some cases, the distortions induced by boundary conditions and external fields result in an extensive nucleation of topological defects [44] that self-assemble in large-area

patterns[42]. Examples are schlieren and marble textures in nematics (Nem); oily streaks, Grandjean and fingerprint textures in cholesterics (N*); linear and focal conic domains in smectics (Sm) and many others[64]. Among them, smectic A (SmA) are of the particular interest, being periodic materials with structural units with size ranging from the nanometer to micron scale. In SmA LC, defect patterns can be easily created over areas as large as a few mm^2 by a rapid self-assembly process which makes them good candidates for the mass-production of periodic templates to be used in various applications[65].

In this thesis we will consider SmA LCs composed of rod-like molecules that tend to align parallel to each other along a common director **n** (a unit vector describing the average local molecular orientation) and arrange in parallel equidistant layers perpendicular to **n**[40,44]. The orientation of **n** is determined by anisotropic interactions with boundaries (anchoring) and/or external stimuli (electric and magnetic fields). SmA LCs have long been known to create periodic defect arrays when confined under incompatible boundary conditions in thin films and droplets. In this case, the **n** field must be distorted and the layers have to bend to satisfy the boundary conditions (Fig. I.1). The requirement that the layer spacing is unchanged[44] can be satisfied by creating defect domains known as focal conic domains (FCDs). Pattern formation is due to FCD nucleation and self-assembly into close-packed arrays[42,44].

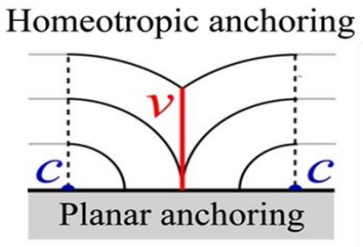

Figure I.1: Schematic illustration of smectic layers bending to satisfy incompatible boundary conditions imposing parallel (planar) and normal (homeotropic) alignment of the director **n**. *c* and *v* are topological defects, i.e. singularities where the layer curvature is undefined.

Axially symmetric toroidal FCDs and 2D hexagonal lattices (Fig. I.2) have been observed when SmA films were subjected to normal (homeotropic) and parallel (degenerated planar) anchoring with no preferential in-plane direction being induced. The

pattern formation was achieved by depositing LC films in air on isotropic liquids[66,67], solid surfaces[68,69], or by sandwiching between solid plates[70].

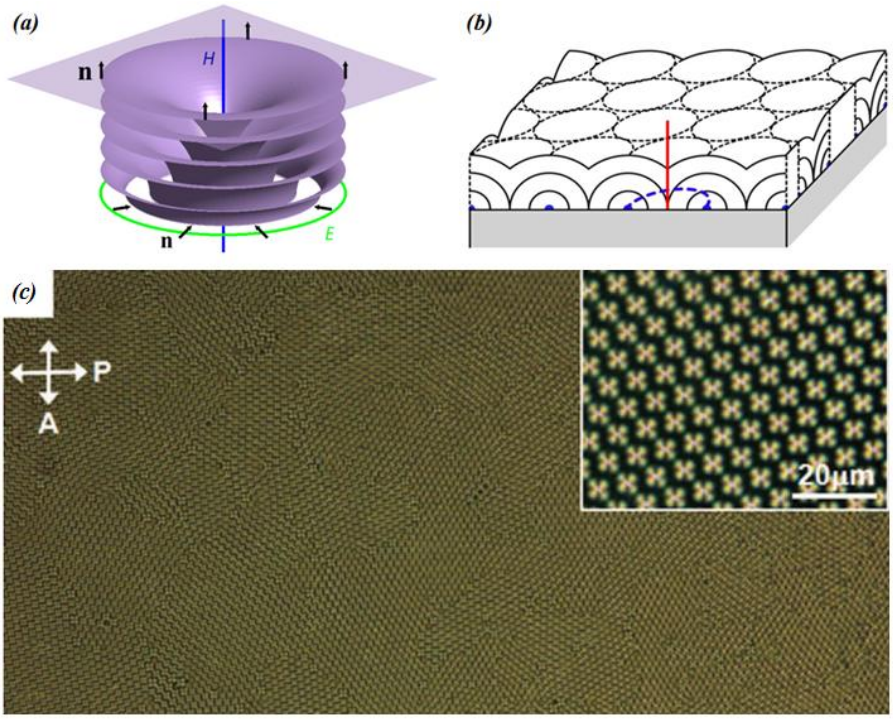

Figure I.2: (a) Schematic illustration of a toroidal FCD[71] with line defects *H* and *E*. The arrows indicate the director **n** orientation. (b) Close-packed hexagonal lattice of FCDs. Red and blue lines correspond respectively to line defects *H* and *E* in (a). (c) Optical micrograph of FCD lattice at the interface between air and a solid surface treated to induce planar anchoring. The inset shows a magnification[72].

Large-area self-assembled FCD patterns have been successfully employed for fabricating templates for soft lithography[72], microlens arrays of dimple and conical shapes[73] and for superhydrophobic patterned surface preparation[65] (Fig. I.3).

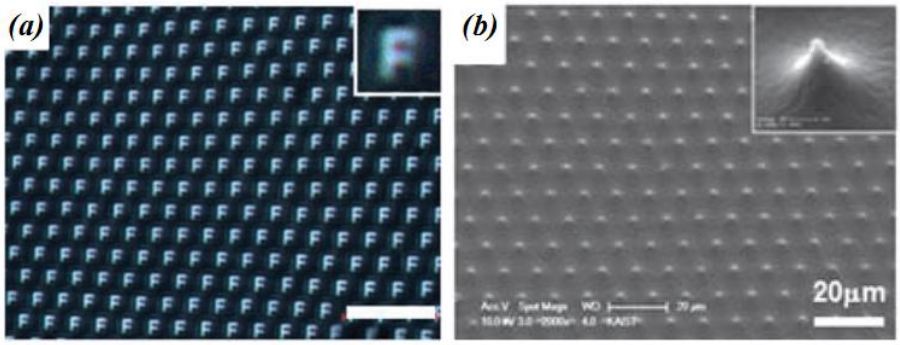

Figure I.3: **(**a) Optical microscopy image of letter "F" projected through an array of toroidal FCD microlenses[73]. (b) Scanning electron microscope image showing a polymer replica of the FCD array, used as superhydrophobic surface[65].

Linear domains (LD) can be created when the anchoring is planar unidirectional, i.e. there director tends to orient along a preferential direction at the aligning surface (Fig. I.4). LD contain curved smectic layers wrapped around straight disclination lines (Fig I.4 (a)). They have been observed for the first time by E. Lacaze and co-workers at CNRS-INSP for thin films of the SmA LC compound 8CB at the interface between air (imposing homeotropic anchoring) and crystalline molybdenum disulfide (MoS_2, imposing planar anchoring)[39].

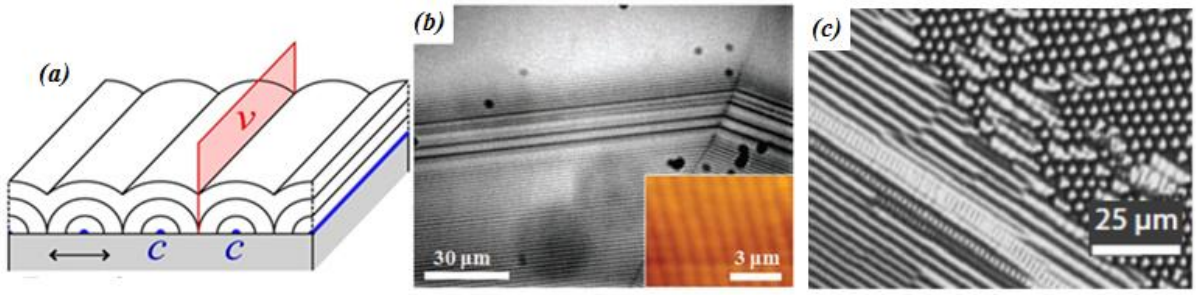

Figure I.4: **(**a) **S**chematic illustration of a LD array formed perpendicular to the planar anchoring direction (indicated with arrow) in a thin film. *c* and *v* are topological defects, disclination lines and curvature walls respectively. (b) POM image of LD arrays in a 8CB droplet deposited MoS_2[39]. The inset shows an AFM image of LC surface topography. (c) The transition between LD array and FCD lattice in droplet of 8CB deposited on mica[74].

Similar 1D patterns were later observed in 8CB film deposited on crystalline mica (Fig I.4 (c))[74,75] and on rubbed polymer surface of PVA (polyvinyl alcohol)[76,77]. A general feature of LD arrays is that their period increases when the film thickness increases, until LDs are replace by a FCD lattice.

From the study of LC defect pattern a promising idea has recently emerged: Combining the anisotropic properties of LCs with those of nanoscale objects such as colloids and nanoparticles (NPs), including quantum dots, nanotubes, graphene ribbons and flakes, may allow the development of new nanostructured functional materials. It is known that properties of NP differ significantly from those of bulk materials and are dependent on the NP size and shape[78-82]. These properties can be tuned also by putting NPs in mutual interaction in a matrix, template or host with defined structural properties. Because of their order and responsivity, LCs are suitable candidates for guiding the assembly of colloids and NPs into well-defined spatial patterns.

The idea stems from early experiments on colloid-LC mixtures performed at the beginning of the 2000s (Fig. I.5). The director field around a micrometer-size particle in the Nem of N* is distorted and requires topological defects to satisfy boundary conditions. When two or more particles are considered, the director distortion provides a long range force that lead to the stable aggregation of the colloidal particles into ordered structures[83-86]. Remarkably uniform arrays of droplets were obtained by demixing and phase separation of a LC-silicon oil droplet [87,88]. Hexagonal lattices of solid colloidal particles were formed at the Nem/air interface (Fig I.5 (a)) [89]. Chain-like particle aggregates were obtained into microcapillaries (Fig I.5 (b)) [90] and sandwich cells [91,92]. Colloidal chains can further self-assemble into the two-dimensional dipolar nematic colloidal crystals (Fig I.5 (c)) [92,93].

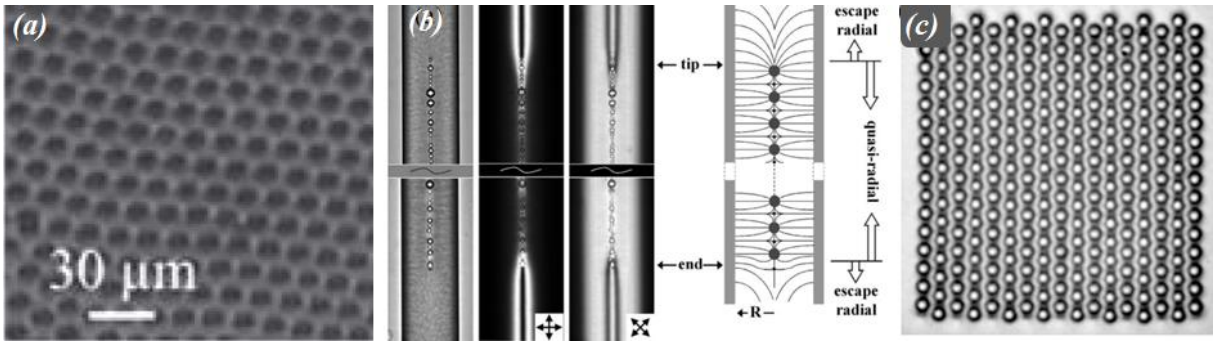

Figure I.5: Optical micrographs of (a) hexagonal colloid crystals of a curved nematic/air interface[89], (b) chain-like colloid aggregates formed into microcapillary in white light and between cross polarizers. The directions of polarizers are indicated [90]. (c) example of a 2D dipolar nematic colloidal crystal, assembled by the laser tweezer manipulation[92].

When the particle size is comparable to the size of LC molecules, the LC-particle and LC-mediated interactions between particles are expected to be different from those of colloidal particles[94,95]. NPs dispersed in a LC can modify the macroscopic properties of the LC such as optical birefringence, dielectric or magnetic anisotropy, and thermal response[95-97]. NPs tend to migrate towards highly distorted regions, reducing the overall energy of the system[98]. Typically, high elastic energy of distortion is focused in topological defects, thus the largest energetical gain is associated with a partial replacing of topological defect core with NPs, resulting in creation of stable trapping sites (Fig. I.6).

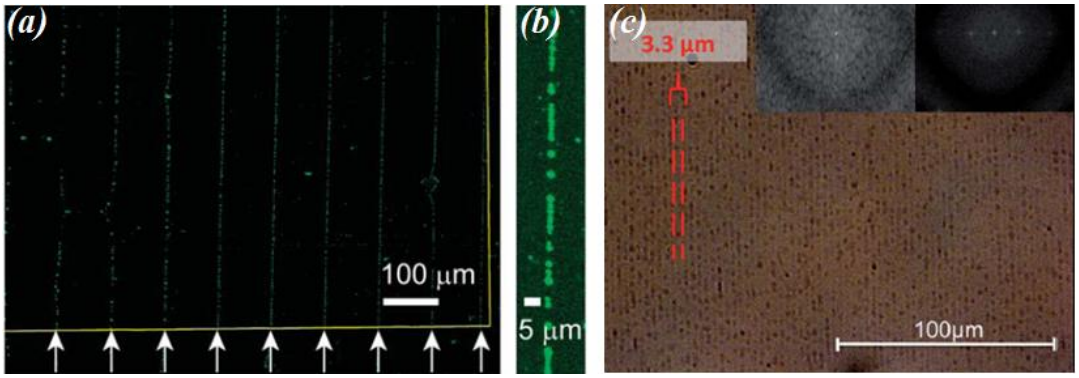

Figure I.6: **(**a) Fluorescence microscopy image of periodically aligned defects in a nematic film with trapped polymer micrometer-sized particles labeled with dichroic dye [99]. (b) Magnification of (a). (c) POM image of an array of dislocations in a SmA LC trapping spherical Au NPs of a diameter 4.7 nm[100].

For the same reason, defect are stabilized and more easily nucleated in the presence of NPs. Indeed, combining LC and NPs has led to the breakthroughs in the stabilization and practical application of frustrated chiral LC phases, namely blue phases (BP) and twisted grain boundary phases (TGB), that were considered “exotic” curiosities a decade ago. In the absence of NPs, these phases exist in a narrow range of temperature, often less than 1 °C, and contain a dense network of topological defects even in the absence of external fields. Defects can effectively trap small NPs of diameter less than 9 nm, such as small polymer coils and spherical NPs[95,101-103]. In turn, trapped NPs stabilize the defect structure over a large temperature range, sometimes exceeding tens of degrees[104-110].

Thermotropic SmA are a very promising class of materials for organizing NPs into regular structures. Both 1D and 2D defect arrays are capable to trap and assemble dispersed colloids, semiconductor quantum dots (QDs) and NPs, imposing periodical

spatial distribution that reflects those of the defect array. Hexagonal lattices of small colloidal spheres were formed within toroidal FCDs (Fig. I.7 (a))[111], where particles were trapped inside the vertical defect line at the FCD centers (Fig. I.2 (a)) [65]. LD arrays capture and organize spherical gold NPs or fluorescent QDs into an array of straight linear chains, with lengths exceeding 50 μm and a diameter comparable to the diameter of a single NPs (Fig. 0.7 (b))[76]. Within the chains, particles are in close interaction and, in the case of Au NPs, optically coupled, showing polarization dependent plasmon resonance. A recent work on SmA LC open films containing semiconductor anisotropic NPs[112] revealed aligning of NPs with their long axis parallel to the defect lines.

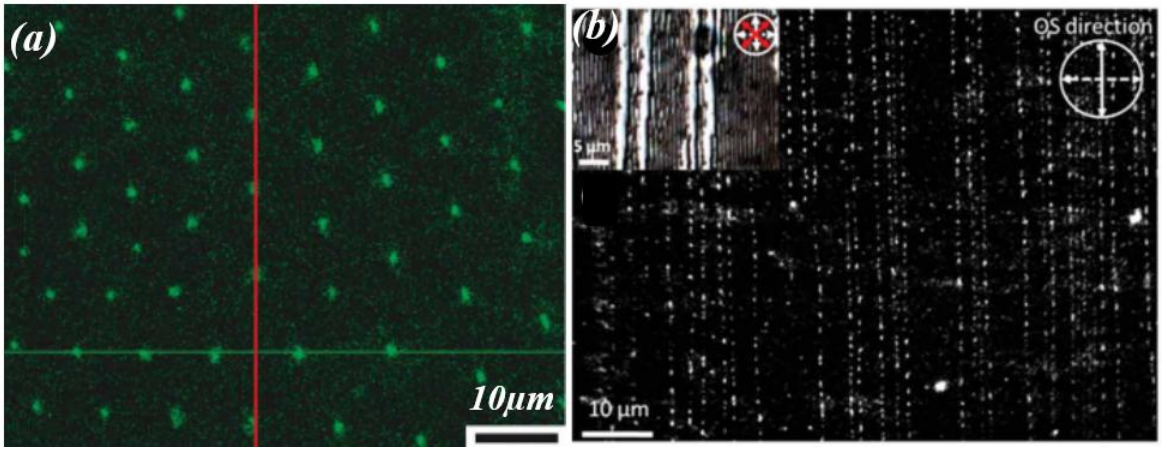

Figure I.7: Fluorescence images of (a) micron-sized colloidal particles assembled into a 2D lattice of toroidal FCDs[111] and (b) QDs of a diameter 5 nm trapped in LDs. The inset show a POM image of the array and arrow indicate the direction of crossed polarizers[76].

In this context, the idea of the thesis on the first step was to understand how to prepare SmA LC defect patterns with predefined morphology and to control and modify the period and dimensionality of the patterns using external stimuli. On the second step, to use SmA defect patterns for ordering and aligning NPs with different material (semiconductor, metal), size, shape (spheres, rods) and optical properties (fluorescence, plasmon resonance) via NP/defect interactions. LC patterns are used as templates to 'transferring' the order of the LC host to the NP guest over areas as large as a few mm^2. Our specific aims were:

1. Controlling pattern dimensionality (1D/2D), symmetry and period as a function of boundary geometry (open films with deformable air interface or closed cells with

rigid boundaries), film thickness and applied electromagnetic fields, with the possibility of reversibly switching between different pattern morphologies.

2. Understanding the relation between array formation and material parameters such as LC order, elastic constants, phase sequence, surface tension and anchoring by considering various SmA compounds and surfaces.
3. Using SmA periodic defect domains for organizing NPs in LC host matrices and creating novel functional materials.

The thesis is developed in 5 chapters:

Chapter 1 is a brief introduction to LC theory. The main thermotropic LC phases and order parameters are introduced with definition of order parameters, elastic energies and coupling with external fields. Topological defects of the orientation order (disclinations) and positional order (dislocations) are also presented, with an emphasis on the typical defect domains of the SmA phase: oily streaks and focal conic domains.

Chapter 2 introduces the materials and methods used in the thesis (LC, NP, QD, dyes, polymers and surfactants) with their main features and parameters. This chapter describes the procedures for sample preparation, surface treatments, fabrication and patterning of transparent electrodes, cell assembly, and LC/NPs mixtures. The chapter also provides a description of the experimental techniques used for the thesis work (POM, fluorescence confocal polarizing microscopy, FCPM, interferometry for thickness measurements and dark-field microscopy).

Chapter 3 presents the defect patterns formed in LC cells with “hybrid” planar-homeotropic anchoring conditions. The pattern morphology depended on the film thickness and could be reversibly changed by applying an external electric field[113]. Models of the pattern internal structure are also proposed.

Chapter 4 addresses the generality of 1D and 2D patterns nucleation and transition between them. A survey of different SmA LC, surfaces and boundary conditions is presented. Moreover,1D pattern nucleation is demonstrated for cells with homogenous planar anchoring conditions subject to applied electric fields. 1D/2D pattern transition is linked to a critical condition appearing at the Nem-SmA transition when the director is distorted and confined to a small thickness.

Chapter 5 presents the results of our work on composite LC-nanoparticle materials. The spatial distribution and alignment of fluorescent NPs of different types (semiconductor spherical and rod-like core/shell CdSe/ZnS QDs, CdSe/CdS dots-in-rods, and dichroic laser dye molecules) is examined by means of fluorescence and polarizing microscopy. Effective trapping, orientation and localization of NPs in defect arrays is discussed in connection with applied electric fields. The effect of particle size and increasing concentration on the SmA textures is also investigated. Critical concentrations of NPs inducing aggregate formation will be compared for two LC matrices and various NP sizes of (3.8 - 50) nm.

The Conclusion section summarizes the main results and proposes further developments. In short, the main findings of this thesis are the following:

1. 1D and 2D defect pattern formation is a common feature of thermotropic LCs having SmA phase in their phase sequences when subjected to incompatible unidirectional planar and homeotropic anchoring conditions.
2. We can create both 2D lattices and 1D arrays either by varying the LC film thickness in the absence of external electric field, or by applying the field at a given thickness. The thickness of the layer where the LC director rotates from normal to parallel to the substrates orientation determines the pattern symmetry and periodicity. 1D arrays appear when such thickness is small, both for hybrid and homogeneous planar anchoring conditions. Transitions between different pattern periods and morphologies are hindered by large energy barrier associated with defect rearrangement: patterns are stabilized against changes in external parameters by ‘topological’ barriers.
3. Anisometric NPs, such as dot-in-rods and dichroic dye molecules, align along the director in the absence of defects but align parallel to line defects within the defect core. An electric field applied normal to the defect line challenges the anisotropic particle-defect interaction and may lead to perpendicular orientation, depending on the particle type and size.
4. In hybrid cells, adding spherical Au NPs to SmA LCs leads to (a) destabilization of LDs, (b) stabilization of another type of defects – striated stripes and (c) it prevents aggregation even for a large concentration of Au NPs.

1. Structure, energy and defects of the smectic phase

This Chapter provides the essential theoretical knowledge for describing the structure and response of smectic defect patterns. Although the focus of this thesis is on the smectic-A (SmA) phase, many of the relevant physical phenomena, such as surface anchoring and orientation under applied fields, can be more easily understood stating from the nematic (Nem) phase at higher temperature. This is due to the fact that the Nem phase show a type of anisotropic molecular arrangement that persists in the SmA phase. Moreover, defect patterns nucleate at the Nem - SmA transition as temperature is lowered and many experimental observations, discussed in details at the end of Chapter 4, suggest that pattern formation is intimately connected to the particular character of such transition.

1.1. The ground state of nematic and smectic liquid crystals

The majority of liquid transforms into crystalline solids when temperature is decreased, like water transforms into ice. But some liquids show intermediate states called "mesophases" when temperature is decreased, with properties between those of liquids and crystals. Liquid crystal (LC) materials show mesophases exhibiting both the fluidity of simple liquids and a reduced symmetry and order that are typical of solids. There are many LC phases, depending on the type of order, i.e. symmetry of the material, some of which are shown in Fig. 1.1 (a)[44].

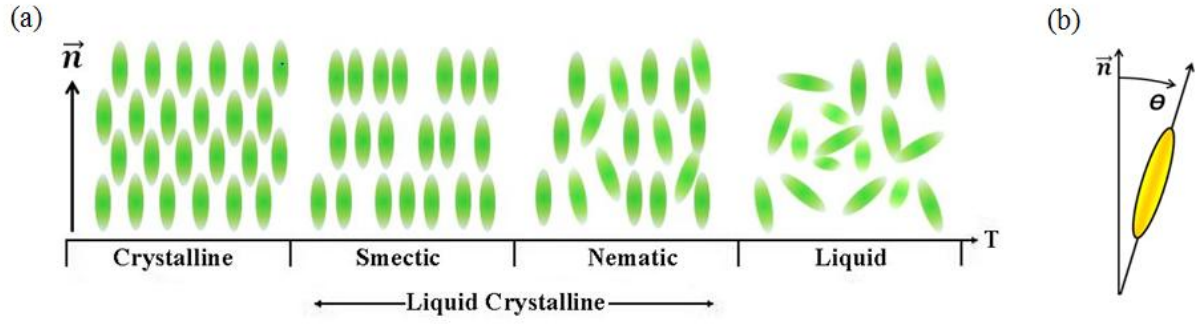

Figure 1.1: (a) Molecular ordering in the mesophases of a thermotropic LC composed of rod-like molecules. (b) Orientation of a rod-like molecule relative to the director **n,** which describes an average local orientation of the LC molecules.

Thermotropic LC are pure materials showing phase transitions as a function of temperature and are typically made of rod-like molecules. The nematic (Nem) phase is the less ordered (most symmetric) of the LC phases, possessing the orientational order described in Fig. 1(a). Molecules tend to align to each other around a common direction **n** called the "director" but their centers of mass a randomly distributed in space, as in a simple (isotropic) fluid.

When molecules are chiral, a chiral nematic phase called cholesteric (N^*) may appear where there is a spontaneous twist of the director orientation: **n** continuously rotates around an axis perpendicular to **n** and the amount of rotation is proportional to the distance travelled along such perpendicular axis, see Fig. 1.2 (a). When the travelled distance is equal to the "pitch" p the director is rotated by 180° and the molecular orientation is equivalent. In this sense, cholesteric is a 'periodic' materials where the (anisotropic) molecular order and properties are periodically repeated along the direction normal to **n.**

In the smectic phase, molecules show a positional (translational) order, in addition to being oriented along with **n**. The molecular density (i.e. number of molecules per unit volume) shows a spontaneous periodic modulation with period a along a direction z. Therefore, a smectic is another example of periodic material. In some case it is useful think of a smectic as to a layered material, i.e. a stack of lamellae with thickness a, although one should bear in mind that lamellae are not always physical entities that can be distinguished from one another (e.g. as they would be for a stack of lipid bilayers or the pages of a book). In the smectic A (SmA) phase, z is parallel to **n** whereas in the smectic C (SmC) phase **n** forms is tilted by an angle β from z towards a direction **c** parallel to the layers. Chiral molecules may form the smectic C^* (SmC^*) phase, where β is constant for all layers, but the **c** direction rotates by a finite angle from one layer to the next, forming a periodical helix with pitch $p>a$, see Fig 1.2. (b). Although the phase sequence depends on the LC molecular structure, pressure conditions and presence of external electromagnetic fields, most achiral LC molecules show the typical phase sequence: crystal → SmA → Nem → Isotropic (Iso) as the temperature is increased.

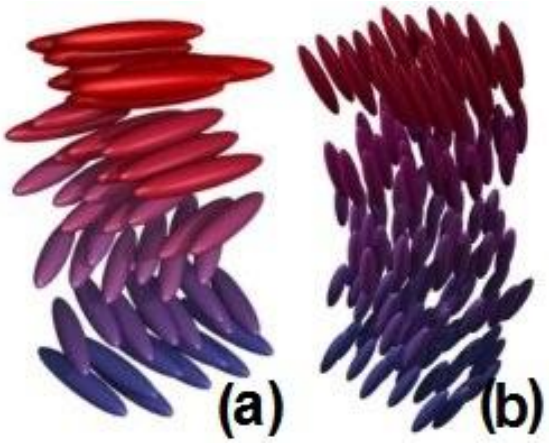

Figure 1.2: LC molecules orientation in chiral (a) N* phase and (b) Sm C* phase[114].

If we consider this phase diagram, one can say that the Nem phase "breaks" the full (spherical) rotational symmetry of high-temperature simple fluids. Indeed, the Nem phase is symmetric under a subset of rotations and reflection operations: any rotation around **n** and the change from **n** to –**n**. Simple fluids and the Nem phase are completely invariant by translations in any direction. The smectic phase further breaks such translational symmetry along the direction *z*. In a sense, the SmA can be considered as a 'parent' phase of the Nem phase: all symmetry elements of the Nem phase are included in the SmA phase and 'passed on' to the Nem phase at the SmA-Nem transition.

1.2. The nematic phase: order parameter, 'ground' state and elasticity

Specifying the symmetry elements of a LC phase is not sufficient to completely describe its thermodynamic state and phase transitions. In the context of symmetry breaking, an order parameter must be introduced for each type of broken symmetry (e.g. Nem or smectic) such that it vanishes at the the phase transition to a higher symmetry phase. In a nematic, the order parameter is a traceless symmetric tensor[44,115]:

$$Q_{ij} = S\cdot(n_i n_j - \delta_{ij}/3) \tag{1.1}$$

where $n_{i,j}$ are the director components and the scalar order parameter S is given by:

$$S = < P_2(\cos\theta) > = \frac{1}{2} < 3\cos^2\theta - 1 > \tag{1.2}$$

where θ is the angle between the **n** and the long axis of each molecule (Fig. 1 (b)). The brackets denote a statistical average. S = 1 for a perfectly aligned LC (e.g. in the crystalline phase) and S = 0 in the isotropic phase. The values of S typically ranges from 0.3 to 0.9, depending on the temperature and LC considered. Since the order vanishes at the transitions to the Iso phase, the natural approach to study the transition is to write down the free energy as a power series expansion of the order parameter. This approach is known as the Landau - Ginzburg phenomenological mean-field theory, developed in the 1930s for the general study of phase transitions (e.g. in superfluid helium and superconductors) and later adapted to LC phase transitions, notably by De Gennes. Near the Nem-Iso phase, the free energy is expanded as combination of the tensor elements Q_{ij} that satisfy the symmetry requirement of the Nem phase.

In an isolated nematic, Q_{ij} is uniform across the material (i.e. both S and **n** are uniform) and **n** can point in any direction. However this ideal situation or 'ground' state can be perturbed by the interaction with the boundaries and external fields, and both **n** and S may show spatial variations. Also in this case, the free energy expansion can be developed by introducing terms containing Q_{ij} and the spatial derivatives $\partial_i Q_{jk}$ that satisfy the symmetry requirements.

Deep in the Nem phase, i.e. far enough from the Iso and SmA phase, the scalar order $S(T)$ depends on the temperature T but is almost uniform for spatial variations that occur over a length scale much larger than molecular dimensions. In these conditions, the free energy expansion contains only the components n_i and derivatives $\partial_i n_j$ of the director. Frank and Oseen showed that the dominant terms in the expansion correspond to three principal modes of deformation called splay, twist and bend, described in Fig. 1.2[116,117]. The increase of free energy per unit volume is given by:

$$\Delta f = \frac{1}{2}K_{11}(div\boldsymbol{n})^2 + \frac{1}{2}K_{22}(\boldsymbol{n}\cdot\nabla\times\boldsymbol{n})^2 + \frac{1}{2}K_{33}(\boldsymbol{n}\times\nabla\times\boldsymbol{n})^2 \qquad (1.3)$$

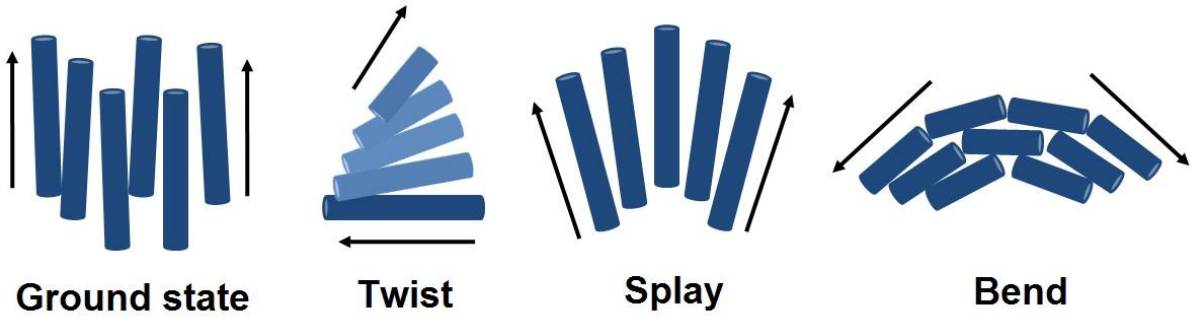

Figure 1.3: Equilibrium state of nematic liquid crystals and three main types of deformations: twist, splay and bend.

Table 1.1 list of the elastic constants for the two LC compounds that were most used in this thesis (see also Chapter 2.1)[118]. The constants depend on $S(T)$, and we report the values close to the transition to the SmA phase.

Table 1.1:

Elastic constants of 8CB and 8OCB near the Nem - SmA transition temperature

LC	Elastic constant	K_{ii} (pN)
8CB	K_{11} at T = 33.4°C	6.95
	K_{33} at T = 33.4°C	9.30
8OCB	K_{11} at T = 67.8°C	8.25
	K_{33} at T = 67.8°C	13.30

The expression of the free energy density is more complicated near the Nem-Iso and Nem-SmA transitions. Near the Iso phase deformations of S and **n** are coupled, and the full tensor Q_{ij} and its derivative must be considered. Near the SmA phase, thermal fluctuations create small smectic-like domains that affect both S and the elastic constants.

1.3. The smectic-A phase

1.3.1. Ground state and order parameter

Materials such as SmA LCs that break a translational invariant and spontaneously create a density modulation can described with a complex order parameter (field). In the ground state (Fig. 1.4), points with equal density span a set of parallel planes spaced by a

constant distance a0. One can express the fact that the phase φ changes by ±2π between neighbouring planes with the formulas:

$$d\varphi = \nabla\varphi \cdot d\mathbf{x} = q_0 \mathbf{m} \cdot d\mathbf{x} = \pm 2\pi \quad (\text{i.e.} \nabla\varphi = q_0 \mathbf{m}) \tag{1.4}$$

where $q_0 = 2\pi/a_0$ and **m** is the gradient direction. In SmA LC the material also shows Nem symmetry, i.e. spontaneous breaking of rotational symmetry and **n**||**m**.

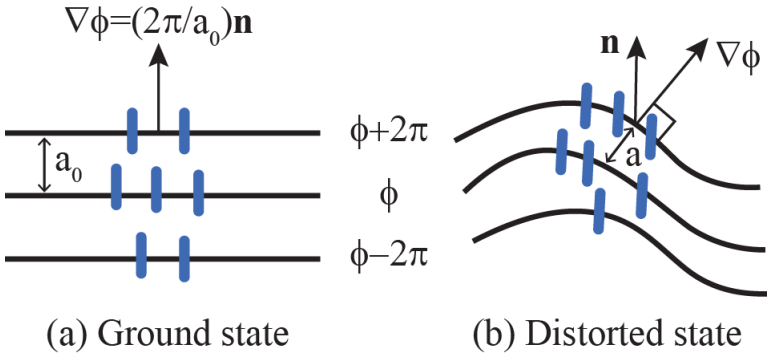

Figure 1.4: Molecules (blue rods) and layers (thick lines) in the smectic-A phase. ϕ is the phase and **n** is the director.

1.3.2. Distortions and elasticity of the smectic A phase

Planes with equal phase may become curved non-equidistant surfaces with **m** ≠ **n** and $|\nabla\varphi| = q = 2\pi/a \neq q_0$. Close to the SmA-Nem phase transition, one can follow the Landau – Ginzburg - De Gennes approach for describing order variation as a function of ψ and its spatial derivatives $\partial_i\psi$. Because in the ground state $\partial_i\psi = iq_0\psi n_i$ (Eq. 1.4), the expansion must contains terms $|\partial_i\psi - iq_0\psi n_i|^2$. The nematic symmetry is such that distortion in the **n** direction have a different elastic constant than in perpendicular direction. Therefore De Gennes proposed the following free energy expansion:

$$f = f_N + a|\psi|^2 + \frac{b}{2}|\psi|^4 + \frac{C_\parallel^2}{2}\left|\nabla_\parallel\psi - iq_0\mathbf{n}\right|^2 + \frac{C_\perp^2}{2}\left|\nabla_\perp\psi\right| \tag{1.5}$$

where f_N is the density of elastic energy of the nematic phase. $\nabla\parallel\psi$ and $\nabla\perp\psi$ are the gradient along **n** and in the perpendicular direction, respectively. The coefficients a changes sign at the Nem-SmA transition temperature T_c and can be written as

$a = \dot{a}(T - T_c)$ near T_c whereas b and $C_{||,\perp}$ are almost constant. In the ground state, the density modulation has amplitude given by $|\psi_0(T)|^2 = -a/b$. When the layers are flat and parallel, $\nabla\psi = q\mathbf{n}$ and the gradient terms reduce to $\left(C_\parallel q_0 |\psi_0|/2\right)^2 (1 - q_0/q)^2 = (B/2)(1 - q_0/q)^2$, where $B = \left(C_\parallel q_0 |\psi|\right)^2$ is the layer compressibility modulus of the SmA phase.

1.3.3. Analogy with superconductors

In 1972 De Gennes pointed out that the free energy expansion of Eq. (1.5) is similar to the Landau-Ginzburg expression describing transition between the normal and superconducting state of a metal[119]:

$$f = \frac{1}{2\mu_0}(\nabla \times \mathbf{A})^2 + a|\psi|^2 + \frac{b}{2}|\psi|^4 + \frac{\hbar^2}{2m}\left|\nabla_\parallel \psi - iq_0\mathbf{A}\right|^2 \tag{1.6}$$

where the vector potential **A** is analogue to the director **n** and the magnetic field $\mathbf{B} = \nabla \times \mathbf{A}$ to the rotor field that appear in the bend and twist terms of the nematic energy (Eq. 1.3). De Gennes related Nem and SmA phases respectively with the normal (N) and superconducting (S) states of a metal. From the analogy with superconductors stemmed various predictions:

(a) A smectic LC tend to expel the bend and twist (i.e. $\nabla \times \mathbf{n}$ is expelled) deformations in the same way as a metal expels the magnetic field **B** at the transition from the N to the S state. Deep in the SmA phase, the director is perpendicular to the layer (as in the ground state) and splay deformation involving $\nabla \cdot \mathbf{n}$ are 'allowed', in the sense that they can be created at the cost of a relatively low increase of free energy per unit volume. On the other hand, bend and twist deformations involving $\nabla \times \mathbf{n}$ are 'forbidden', in the sense that they require a high energy density. When bend must be considered, the free energy expansion in the deep SmA phase is sometime written as:

$$f = \frac{B}{2}(1 - q_0/q)^2 + \frac{K_{11}}{2}(\nabla \cdot \mathbf{n})^2 \tag{1.7}$$

where q, $\mathbf{n}$ and $\nabla\psi$ are linked by the relation: $\nabla\psi = q\mathbf{n}$. For 8CB, the modulus is $B \approx 10^7$ J/m^3 close to the SmA-Nem transition[120]. The first term can also be written as $B\varepsilon^2/2$, where $\varepsilon = (a_0 - a)/a_0$ is the layer strain.

(b) Due to the high value of B, the strain energy increases so rapidly that the strain deformation may 'melt' the SmA phase into the Nem phase. In superconductor, when |**B**| exceeds a certain temperature-dependent threshold, the S state is frustrated and the field may either enter the metal either in the form of topological defects – line singularities called magnetic "vortices" – or create non-singular regions with normal behaviour, i.e. with $\mathbf{B} \neq 0$. The first or second scenario occurs depending on the type of material that is classified as type-II in the first case or type-I in the second case. A SmA LC is expected to behave in a similar way, although it is often unclear to which type a LC material belongs. This analogy with superconductors led to the famous discovery of the Twist Grain Boundary (TGB) phase whereby twist distortions in a chiral LC are expelled from the bulk and confined to grain boundaries in the form of periodic arrays of twist dislocations [121].

(c) The twist (K_{22}) and bend (K_{33}) elastic constants diverge at the transition from the Nem to SmA phase. This has been proven experimentally for various SmA LC, including 8CB [122].

(d) If a bend distortion is applied over a length scale h (e.g. the thickness of a LC film) the elastic energy is of the order of $K_3(\nabla\times\mathbf{n})^2 \approx K_3/h_c^2$. The analogy with superconductor suggests that this energy equals the condensation energy $E_c = -a|\psi_0|^2$ at the Sm-Nem transition in a type-I material. The condensation energy scales as as $E_c \propto \theta^{2\gamma}$ as a function of the reduced temperature $\theta = (T - T_c)/T_c$ where the critical exponent is $\gamma = 1$ in the mean-field approximation and close to $\gamma = 1.3$ if fluctuations are considered [119]. As a result, the transition temperature of a bent nematic is *depressed* compare to the ground state: at a given temperature $T < T_c$ the Sm phase condenses only in bent regions whose thickness exceeds the critical value $h_c = h_0\theta^{-\gamma}$, whereas bent regions with $h < h_c$ persist in the Nem phase ($|\psi| = 0$). In other words, for a given thickness h, the bend distortion becomes critical at temperature $\theta = (h_0/h)^{1/\gamma}$. The relevance of this point will be discussed at the end of Chap. 4 concerning SmA LC films with thickness around 1 μm.

1.3.4. Confocality

The notion of confocality play a central role in the study of SmA LCs as it extends to curved surfaces and smectic 'lamellae' to intuitive idea that equidistant surfaces are 'parallel'. Consider the deep SmA phase where the strain is zero (i.e. $\nabla q = \nabla(2\pi/a) = 0$) and $\mathbf{n} \| \nabla\varphi$ (i.e. $\nabla\varphi = q\mathbf{n}$). These conditions immediately imply that $\nabla\times\mathbf{n} = \nabla\times\nabla\varphi = 0$, i.e. bend and twist are completely absent. Vice-versa, if $\nabla\times\mathbf{n} = 0$ and $\nabla\varphi = q\mathbf{n}$, then $\nabla q = 0$ and the smectic 'lamellae' are equidistant,.

Consider the normal **m** at a point **p** on a curved lamella (Fig. 1.5). A second surface can be considered 'parallel' to the first if all its points can be obtained by translating the point **p** by a constant distance a_0 along **m**. We can describe any (smooth differentiable) surface by choosing two tangent directions **x** and **y**, normal to each other and to **m**, such that the coordinate along **m**, say *z*, is a quadratic form of the coordinates *x* and *y* around **p**. The quadratic form is diagonalized along two principal axes **x** and **y** for which we can define two radii of curvature r_1 and r_2 that join the surface with the centers of curvature O_1 and O_2. The centers can be on opposite sides of the surface and the radii are considered positive or negative if they are parallel or antiparallel to **m**, respectively (Fig. 1.5 (a)).

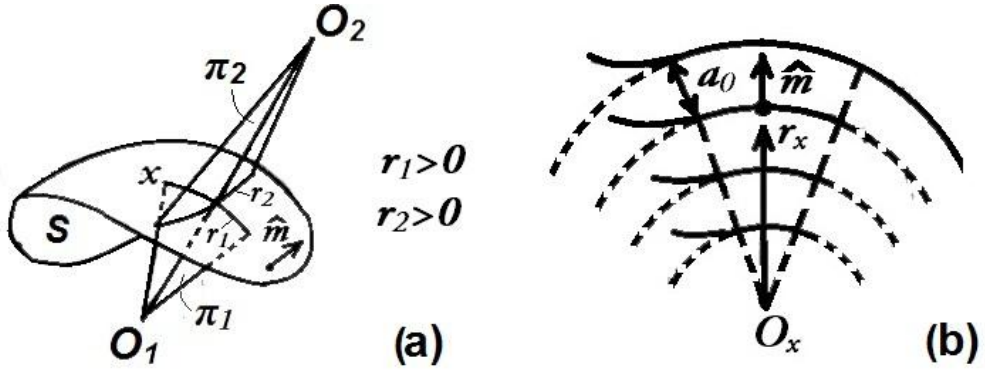

Figure 1.5: (a) Normal **m** and principal coordinates *x* and *y* of a surface *S* at a point **p**. O_1 and O_2 are the centers of curvature located on the focal surfaces, r_1 and r_2 are the principal radii of curvature. (b) Cut through a principal plane *xz* of a confocal set of surfaces.

As **p** moves along the surface, the centers O_1 and O_2 span two "focal" surfaces, possibly degenerate as lines (e.g. two lines for a torus, one line for a cylinder) or point

(for a sphere). It can be demonstrated that two 'parallel' surfaces are also necessarily "confocal", i.e. they share the same focal surfaces[123,124]. If we consider a point **p** on any surface of a confocal set and identify the set of points located on the other surfaces, these points share the same normal **m** and are equally spaced by a distance a_0. The principal plane *xz* (or *yz*) is common to the entire set and the radii of curvature on this plane, taken at the equally spaced points, are $r_x + pa_0$ (resp. r_y+qa_0) where r_x (resp. r_y) is the radius of curvature in **p** and pa_0 (resp. qa_0) is the distance from **p** (Fig. 1.5 (b)). In other words, a confocal set can be approximated as a set of concentric cylindrical surfaces.

1.4. Topological defects

The main goal of this thesis was to characterize the periodic patterns that form in SmA film at the transition from the Nem to SmA phase. The feature that distinguishes these pattern from other periodic LC patterns such as Helfrich undulations and Williams domains[44] is that they are the result of defect nucleation and self-assembly. Therefore, in this section we will describe the different types of defects that are commonly encountered in the Nem and SmA phases of thermotropic LCs and the energy of distortions they cause in LCs.

One can observe a topological defects formation even in homogeneously aligned smectic LCs due to a non-uniform thickness of the film or external inclusions. The distortion caused by inhomogeneities are transferred into smectic matrix, like presented in Fig. 1.6, on the characteristic penetration length, which can be determined according to Blinov[125] as follows:

$$L_p = \frac{1}{q^2\lambda_s} = \frac{\Lambda^2}{4\pi^2\lambda_s} \tag{1.8}$$

where characteristic length of smectic LCs $\lambda_s = \sqrt{\frac{K_{11}}{B}}$ (typically $\lambda \approx 1$ nm). It means that deformations of LC smectic layers caused by inhomogeneities are of the same order as inhomogeneities.

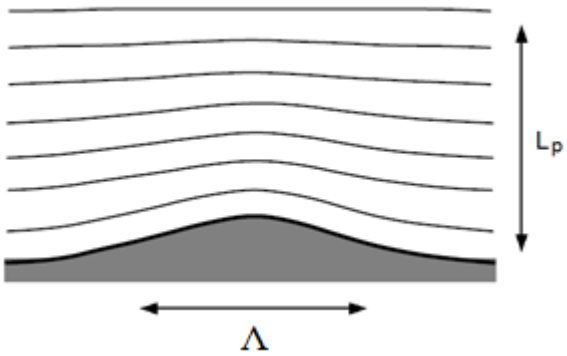

Figure 1.6: Deformation of smectic layers caused by an inhomogeneity on the boundary[124].

1.4.1. Defects of the nematic phase

Topological defects of the Nem phase are points, lines or wall singularities where the director **n** cannot be uniquely specified and molecular ordering is altered or removed. Here we consider disclination lines that were commonly encountered in our experiments.

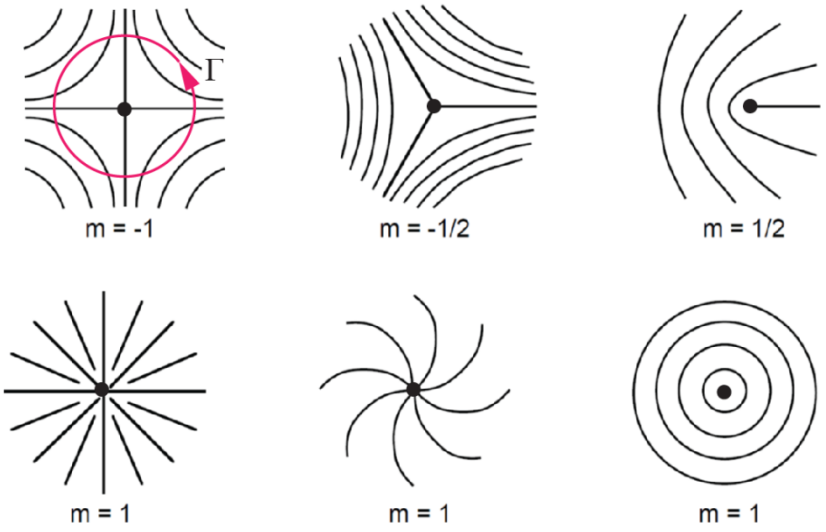

Figure 1.7: Typical disclination lines in the Nem phase[126].

Near the defect line, **n** is perpendicular to the line and the director field can be characterize by the winding number *m* (also called topological charge) defined as follows.

Consider any loop Γ containing the disclination and linear axis having the disclination as the origin. The orientation of **n** on Γ is given by: $\phi = m\theta + const$, where θ is the polar angle that specify a point on the loop. Therefore, **n** rotates by an angle $2\pi m$ over a complete loop. An example of disclinations are given in Fig. 1.7. The study of topology of the Nem phase reveals that disclinations with integer winding number m are unstable. For instance, one may expect that the director field in a round capillary with normal anchoring conditions on the internal surface to have topological charge $m = 1$. Instead, two lines with $m = 1/2$ are observed or a defect with reduced dimensionality (point "hedgehog" defects).

1.4.2. Elementary defects of the smectic phase

Because the SmA phase includes the symmetry elements of the Nem phase, i.e. a positional order and director **n** can be defined, disclination can be considered as defects of the SmA phase. However, the SmA phase also shows other types of defects that are proper to the positional order, namely dislocation lines. Figure 1.8 shows typical defects of the SmA phase[115].

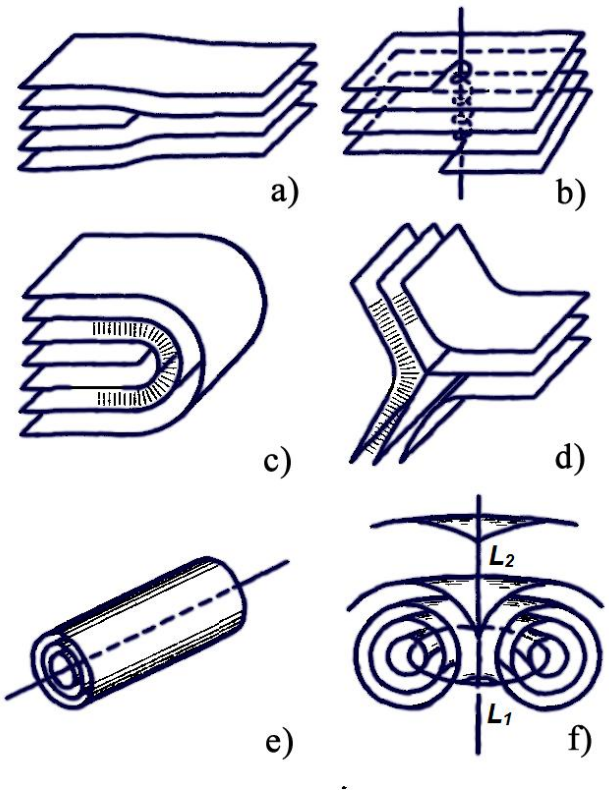

Figure 1.8: Topology of the defects in smectic A liquid crystals[115]: (a) edge dislocations, (b) screw dislocations, (c) wedge disclinations with topological charge $m = +1/2$, (d) wedge disclinations with topological charge $m = -1/2$, (e) roll, f) toroidal FCD.

(a) Edge dislocations (Fig. 1.8 (a)) are defect lines intrinsic to solid crystals. Typically, edge dislocations appear due to the external force tending to change the interlayer distance. As an example, usually they appear in wedge-type cells, where they compensate the difference in the interlayer spacing. Experimentally, edge dislocations are hardly detected, due to the very small size of the defect core (typically 2-3 nm) they do not show any contrast in polarizing microscopy. However, closer to the SmA – SmC transition in the vicinity of the defect SmC phase is more favorable, so the LC director **n** becomes tilted and can be visualized by a polarizing microscope[127], see Fig. 1.9 (a). Edge dislocations can also be revealed by X-ray diffraction, as the presence of large quantity of edge dislocations in the LC volume results in broadening of Bragg diffraction peaks[128]. Because of the wedge geometry of a cell edge dislocations are periodical. In the case of small angle of divergence α, the periodicity can be expressed as $\Lambda = b/tan\alpha \approx b/\alpha$ [124], where b – is a Burger's vector. Generally Burger's vector is a number of added layers $b = na_0$, where n is integer and a_0 is an averaged layer thickness. As it defines by a contour around the defect lying in a plane which intersects the defect, the generalization can be written as follows $\oint \frac{n}{a} \cdot dl = \sum_i n_i$, where the summation extends around all the embraced contour[44]. The schematical sketches of the edge dislocation with small Burgers vector are presented in the Fig. 1.8 (a) and Fig. 1.9 (b). In fact, when the angle α is large, or homeotropically oriented SmA film is locally pressed, dislocations with a large Burgers vector (up to hundred layers thickness) become visible and can be revealed by polarization microscopy. It was discovered for a first time by Williams and Kléman in their early work[129]. They showed that such dislocations are formed by two elementary disclinations L_1 and L_2 of opposite half-integer strength, separated by the distance b/2, schematically presented in Fig. 1.9 (c).

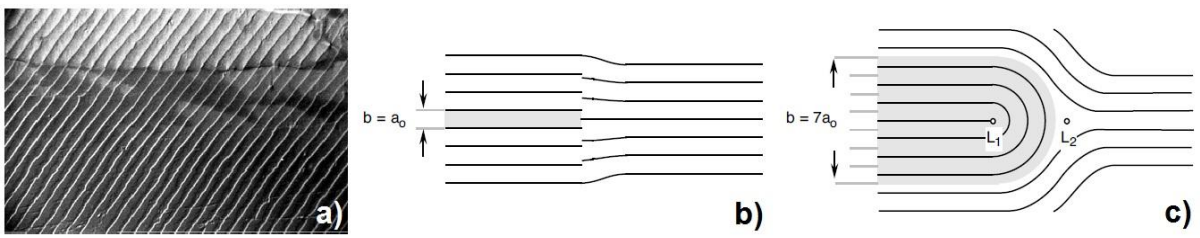

Figure 1.9: (a) Optical micrograph of edge dislocations close to the SmA – SmC phase transition; (b – c) core model for edge dislocations of different Burger's vectors $b = a_0$ and $b = 7a_0$ respectively [124].

The energy of the edge dislocations with small burgers vector (b = a_0) per unit length can be estimated as[124]:

$$E_{edge} = \sqrt{2/\pi}\, B^{\frac{1}{4}} K_1^{\frac{1}{4}} \gamma_c^{\frac{1}{4}} b \tag{1.9}$$

where K_1 is elastic constant, B – compressibility modulus. This formula means that energy of an edge dislocation and its Burger's vector are proportional. In the case of large Burger's vector Williams and Kléman proposed next equation for the core energy estimation[129]:

$$E_{edge\ core} \approx \frac{K_1 \pi}{2} \ln\left(\frac{b}{r_c}\right) + E_c \tag{1.10}$$

where r_c - is a disclinations core radii and E_c – their energy. In practice edge dislocations with large Burgers vectors are more frequent in SmA liquid crystals.

(b) Screw dislocations (Fig 1.8 (b)). This type of defects are usually observed in the chiral TGB_A phase (twist grain boundary SmA phase) or in SmC*. A periodic array of equidistant screw dislocations forms the grain boundary between smectic blocks that are free of twist, bend and defects (Fig. 1.10). Electron microscopy investigations made by Ihn et al. [130] revealed that screw dislocations align parallel on average along the local director **n,** like presented in Fig.1.8 (b). Axes of dislocations rotate in a helical fashion from one boundary to the next. Such rotation of defects pattern leads to the following rotation of the director of SmA along the axis perpendicular to the grain boundaries, see Fig. 1.10 (a). Distance between the neighboring dislocation lines l_d can be determined as following:

$$l_d = \frac{Pl}{2\pi l_b} \tag{1.11}$$

where P is a helical pitch, l is a smectic layer thickness, l_b is a distance between the grain boundaries.

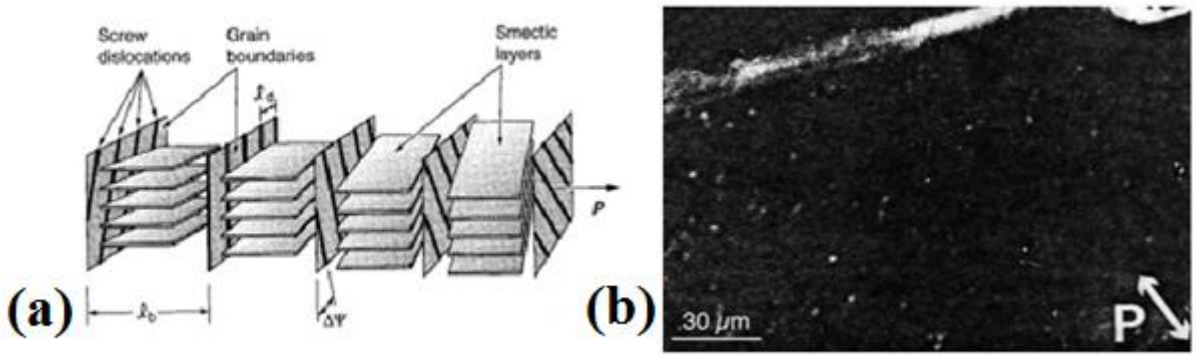

Figure 1.10: (a) Schematic representation of the TGB_A phase structure[131]. (b) Optical micrograph of SmC* film in homeotropic orientation. The screw dislocations are visible as bright spots on the black background[124].

The energy of screw dislocation per unit length can be expressed as following[124]:

$$E_{screw} = \frac{Bb^4}{128\pi^3 r_c^2} + \frac{K_3 b^4}{64\pi^3 r_c^4} + E_c \qquad (1.12)$$

where r_c – core radius, E_c – core energy, b is a Burgers vector. One interesting feature follows from this equation: since there is no dilation and layer curvature, screw dislocations do not have strain energy. For screw dislocations inherent only core energy, described by Williams and Kléman for the dislocations with a large Burgers vector[44].

The core structure of the screw dislocations is still not well understood. As an analogy with edge dislocations, a core can be nematic or isotropic. The screw dislocations are invisible for polarizing microscopy for both SmA and SmC phases. They can be observed only like a bright or dark spots (depending on the polarization of light) on a uniform background in SmC* phase, see Fig. 1.10 (b). Experimental observations of the screw dislocations were also performed using electron microscopy[124].

(c) Wedge disclinations (Fig. 1.8 (c-d)) are analogous to disclinations in the Nem phase (Fig. 1.11 (a)). However, the symmetry of the SmA phase stabilizes defects with an integer winding number. For instance, it is possible to create a director field with charge m = 1 (Fig. 1.8 (e) and Fig. 1.11 (b)) in a round capillary with normal boundary conditions. At the transition to the Nem phase, the line splits into lines with m = 1/2 and/or point defects, like presented in Fig. 1.11 (a).

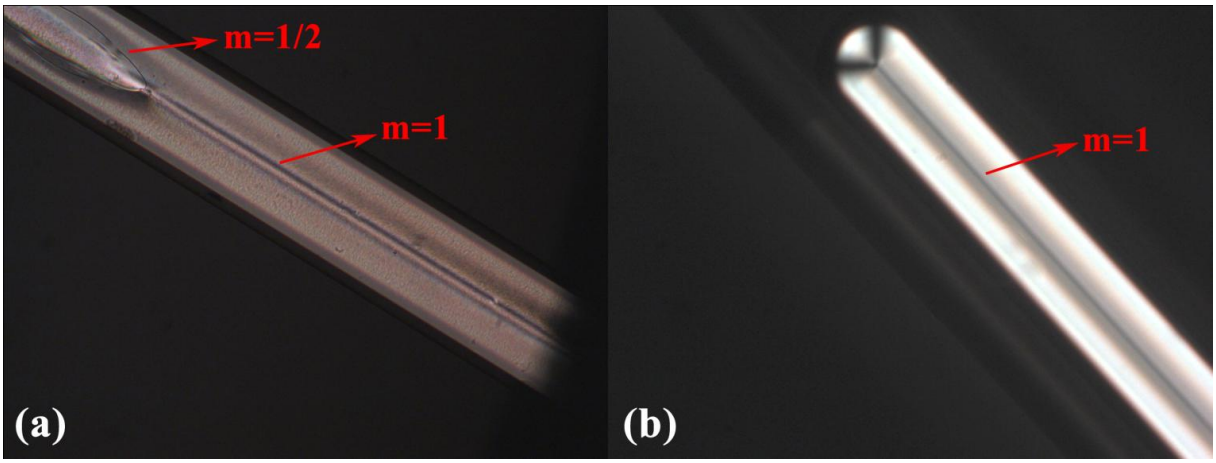

Figure 1.11: Polarizing microscopy images taken under the crossed polarizers illustrating (a) splitting of a defect line with integer winding number formed in capillary onto two defect lines with half-integer winding numbers in the Nem phase; (b) a defect line with integer winding number in the SmA phase.

For the satisfaction of long-range ordering in SmA liquid crystals, disclination lines occurs only in pairs with opposite sign, thus forming either dislocations or focal conic domains. For instance, edge dislocation consists of two linear disclinations is presented in Fig. 1.9 (c). L_1 and L_2 indicates respectively line defects with $m_1 = +1/2$ and $m_2 = -1/2$ winding numbers. Often disclinations in smectic liquid crystals have curved shape. The energy of disclination line can be estimated as following[44]:

$$E_{discl} = \frac{\pi}{2} K_1 ln \frac{ba_0}{2r_c} + E_c \qquad (1.13)$$

where E_c is an energy of the defect core.

1.4.3. Confocal domains: focal conics and oily streaks

In the SmA phase, the director field can be easily distorted and the lamella curved, but changing the distance a_0 between lamellas requires a high energy. These requirements lead to the formation of characteristic defect domains that combine multiple elementary defects of the type presented in the previous section.

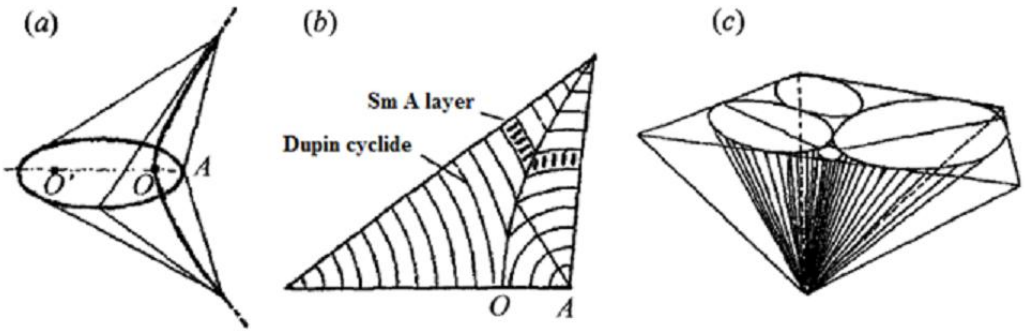

Figure 1.12: (a) Geometry of confocal pair in SmA LC. (b) Cross section of top conic demonstrating the geometry of smectic layers and orientation of molecules within the layer. (c) An example of filling SmA liquid crystal film by conics with different sizes [132].

(a) Focal Conic Domains (FCD) are sets of equally spaced curved lamellae called Dupin cyclides (Fig. 1.12 (a). The surfaces are confocal and share their centers of curvature that are located on two conjugated foal conics, a hyperbola *H* and an ellipse *E*, with the focus of one curve being the summit of the other. The shared normal of these surfaces defined the directions of **n.** They are all possible directions specified by taking any points on *H* and any point on *E*. Around *E* and *H*, the director **n** is similar to that surrounding a disclination line (although **n** is not always perpendicular to the focal conic line). When *E* is a circle (zero eccentricity), *H* is a straight line (infinite eccentricity) passing through the circle center and each cyclid is a torus (Fig. I.2 (c) and 1.8 (f)). When both eccentricities are equal one, the two conics are parabolae. The distortion of the layers is very week, except the region where the parabolae cross[133] (Fig. 1.13 (c)). Square FCDs[38] (Fig. 1.13 (d)) are formed by two hyperbolic branches of *H* making an angle of 45° with the plane of *E* with eccentricity close to the value $1/\sqrt{2}$. An optical micrograph of square FCD lattice was presented in Fig. I.4 (c).

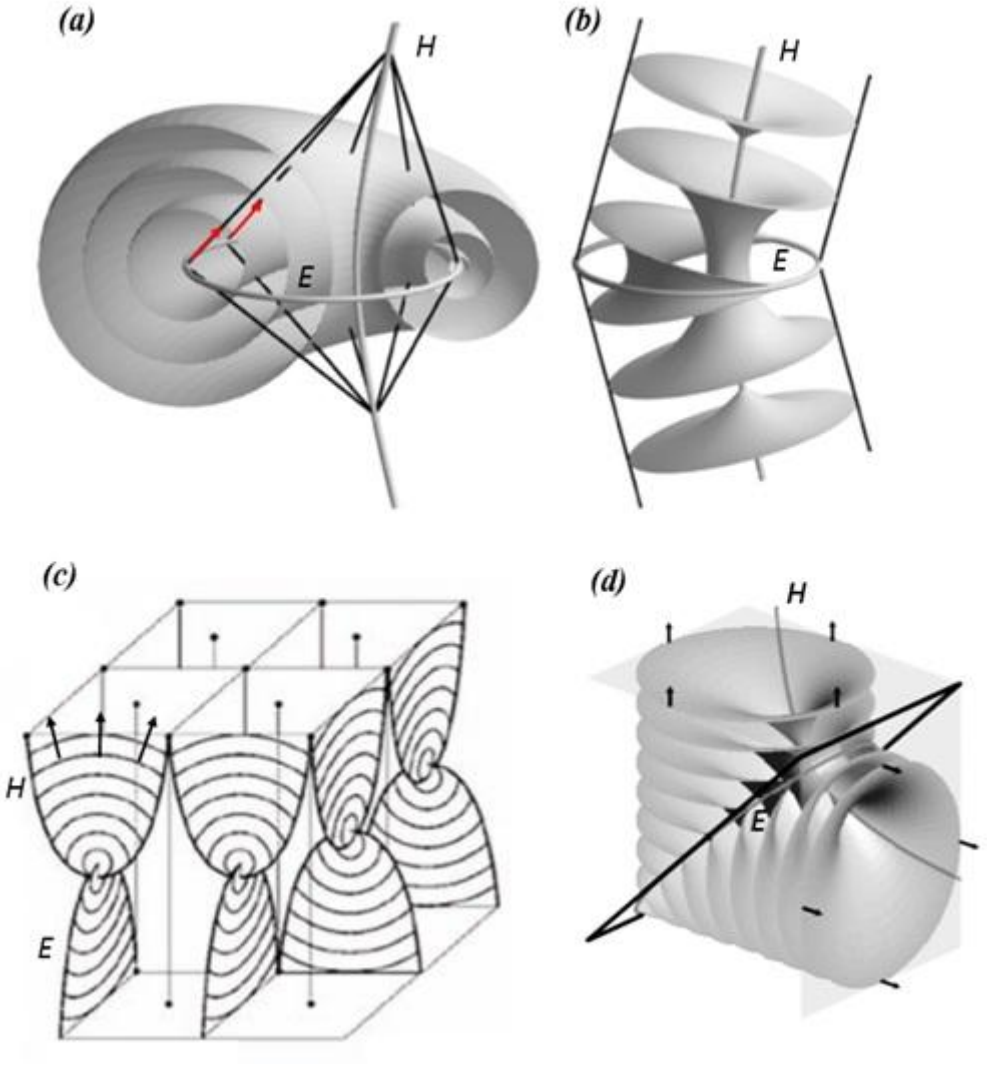

Figure 1.13: (a) A complete elliptical FCD (set of Dupin cyclides)[134]. (b) Region of the FCD with negative (Gaussian) curvature[134]. (c) Layer arrangement and lattice of parabolic domains[65] and (d) Square FCD[38]. H and E are line singularities: hyperbola and ellipse respectively. The director orientation is indicated with arrows.

In thermotropic LC, only the region with negative Gaussian curvature of the FCD (with two principal radii of curvature having opposite signs everywhere) is usually observed (Fig. 1.13 (b)). FCD associate following the laws first enunciated by Friedel[123]. The first law states that, if two focal domains are in contact, they are tangential to each other along the common generator of their boundaries. The second Friedel's law of association (so called "law of corresponding cones") requires coinciding of the cones with generators which have a common apex that belong to two conics. Both requirements can be completely satisfied in grain boundary geometry (Fig. 1.15) and ellipses of neighboring

FCDs are in contact along the major axes, or along the minor axes. Cones with different sizes can fill all the volume of SmA LCs, Fig. 1.12 (c)[132].

(b) Oily streaks. Frequently in thick homeotropic smectic LC films as well as in cholesteric liquid crystals one can observe thick bright lines, which thickness can reach even the thickness of the sample, like presented in Fig. 1.14 (a). Comparing with cholesteric liquid crystals, where defects with integer topological charge do not have a core, in smectic A liquid crystals oily streaks have a singular core[40]. The inner structure of these lines is complex and usually consists of an array of focal conic domains separated by flat layers parallel to the boundaries. According to G. Friedel[135] oily streaks can be presented like a pair of edge dislocations with an opposite sign and large Burgers vector, see Fig 1.14 (b). However, sometimes appear dislocations of small Burgers vector, which annihilate with time to the dislocations with large $\boldsymbol{b}$, that are energetically preferable. The core topology of edge dislocations in this case prevents the interaction of opposite sign dislocations[124]. Moreover, due to the elastic properties of SmA LCs oily streaks usually split into a series of focal conic domains[136]. The intervals between the FCDs can be filled either with the layers of edge dislocations or with FCDs of smaller size, like depicted in Fig. 1.14 (c). Continuous changing of the focal plane in polarization microscope reveals the formation of FCDs and edge dislocations along the film depth in oily streak. FCDs are characterized by a Burgers vector b that is a sum of two dislocations of opposite sign b_1 and $-b_2$ thus $b = b_1 - b_2$. Stability of oily streaks as well as focal conic domains depends on the tilt of smectic layers at the aligning surfaces, larger tilt results in better stability.

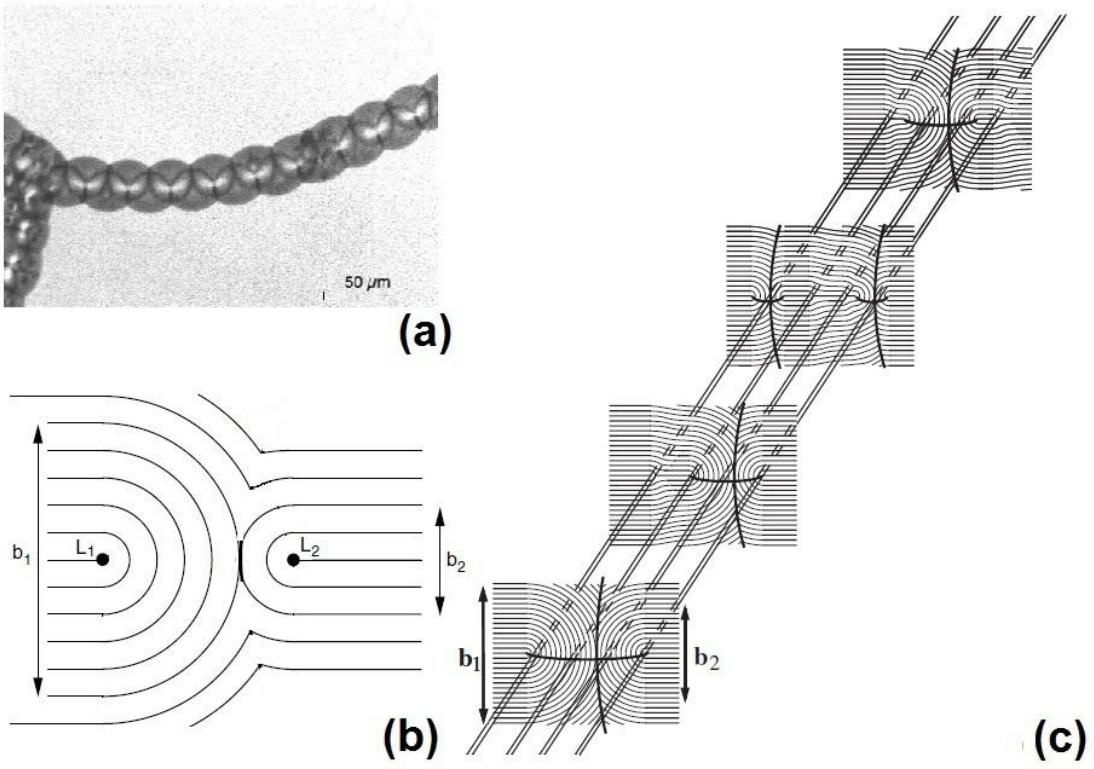

Figure 1.14: (a) Magnified image of oily streak observed in unpolarized light in a homeotropic 8CB sample[124]. (b) Oily streak formed by two edge dislocations L_1 and L_2 of Burgers vectors b_1 and b_2. (c) Structure of an oily streak shown in (a), composed of a FCD chain accompanied by edge dislocations[136].

1.4.4. Grain boundaries

In the volume disoriented monodomains or single crystals of SmA are connected by regions with strong variations of the order parameter, called grain boundaries, which can be formed from the bent smectic layers only, or involve line defects and focal conics[137]. Those monodomains meet with a misfit angle $2\theta\infty$ of the layers across a wall, assumed to be symmetric (Fig. 1.15)[124].

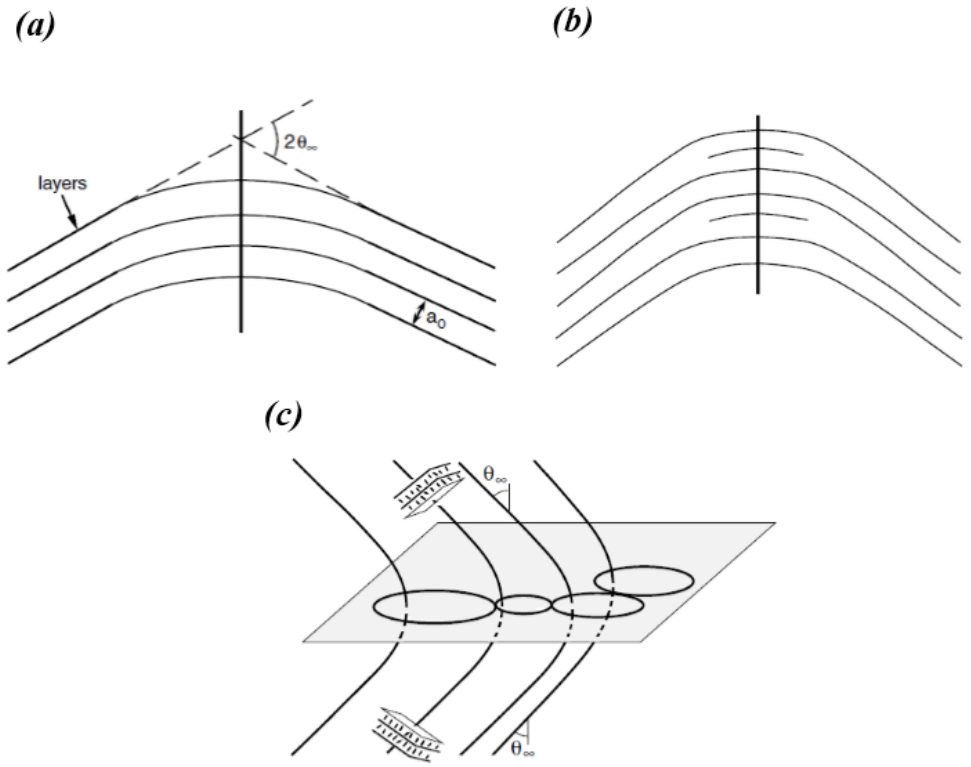

Figure 1.15: Schematic illustrations of different types of grain boundaries[124]: (a) curvature walls made of bent smectic layers (b) combined walls containing an array of edge dislocations and (c) Grandjean walls involving FCDs.

(a) In low-angle grain boundaries, with very small $\theta\infty$, called curvature walls, SmA layers are continuously bent, without breaking (Fig. 1.15 (a)). The elastic cost per unit surface is a function of an angle of the layer rotation[44]:

$$E_c \approx 2/3\sqrt{K_{11}B}\theta_\infty{}^3 \tag{1.14}$$

(b) When $\theta\infty$ exceeds a few degrees, grain boundary can be split into periodic edge dislocations (Friedel 1964) which relax the layer dilation at the center of the wall, forming a mixed or combined wall (Fig. 1.15 (b)). The energy of such a wall can be described as following[124]:

$$E_{comb} \approx \frac{K_{11}}{a_0}\theta_\infty{}^2 \tag{1.15}$$

where a_0 is the layer thickness.

(c) When $\theta\infty$ is larger than about 25°, Grandjean walls (focal domain walls) can be formed. In this geometry, the ellipses of FCDs are in the plane of the grain boundary and the hyperbolas have asymptotic directions perpendicular to the layers on both sides of the boundary (Fig. 1.15 (c)).

1.5. Surface anchoring

As it was mentioned in introduction, different LC textures and periodic defect patterns can be created by varying boundary conditions and imposing particular surface anchoring. Surface anchoring is the phenomenon of spontaneous alignment of the liquid crystal director **n** along specific direction at a surface. Anchoring is caused by anisotropic interactions of the LC molecules with the surfaces and involves both surface geometry (e.g. presence of oriented grooves or holes) and composition (e.g. surface charge and polarity)[138]. The surface molecular orientation of the LC propagates over macroscopic distances, so that by specific mechanical or chemical surface treatments a particular alignment can be induced in the bulk of the LC. Three main types of LC director alignment relative to a solid surface or free interface (i.e. with air) have been considered in this thesis: planar (parallel to the surface), homeotropic (perpendicular) and tilted. The LC director is specified by the polar (zenithal or out-of-plane) angle Θ and an azimuthal (or in-plane) angle φ (Fig. 1.16). The preferred director orientation at the surfaces is sometimes called “easy axis”.

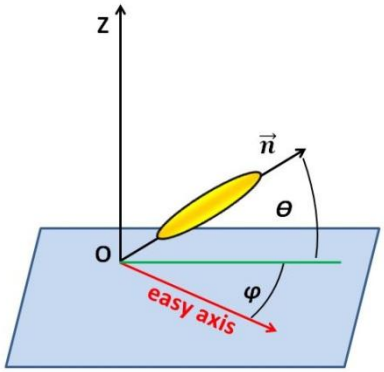

Figure 1.16: Schematic illustration of the director **n** orientation near the surface. Θ and φ are the polar and azimuthal angles respectively.

In the case of planar anchoring (Fig. 1.17 (a)) of LC molecules with a surface, **n** lies in the plane of the surface, so that the polar angle $\Theta = 0°$. If φ is fixed, the anchoring

is said to be unidirectional planar anchoring. When φ takes distinct discrete values the anchoring is multidirectional or multistable. φ may also take any random value, then the anchoring is planar degenerate. The alignment is called homeotropic when $\Theta = 90°$ (Fig. 1.17 (b)). Tilted director alignment is determined by fixed polar angle $\Theta \neq 0°$ and can be unidirectional or degenerate, depending on the value of φ (Fig. 1.17 (c)). As a general rule, the LC alignment is normal to the substrate if the surface energy of the LC is higher than the surface energy of the substrate, and parallel in the opposite case[139].

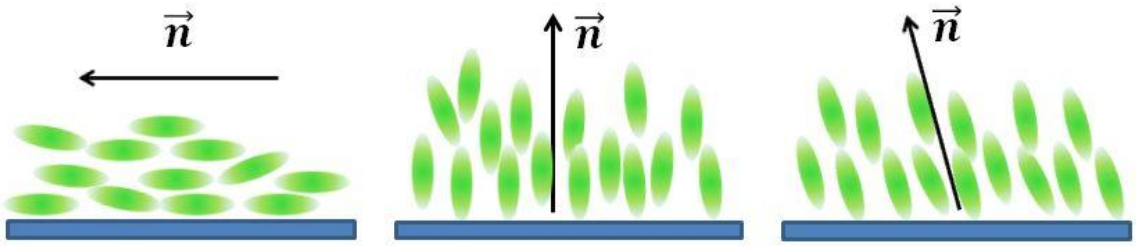

Figure 1.17: Schematic illustration of a) planar, b) homeotropic and c) tilted LC orientation at a surface. Arrows indicate the director **n**.

Interaction of initially isotropic easy axis on orienting substrate with ordered LC phase may result in appearance of the anisotropy on the orienting surface. This phenomenon is known as print or surface memory effect[38,140]. For instance, after the following Iso-Nem/Sm phase transition LC director can partially restore the "printed state".

In the presence of bulk distortions, a torque may act on the director at the surface, resulting in a deviation from the easy axis. In the Nem phase, the increase of surface free energy associated with small deviations (anchoring energy) is approximately given by the Rapini-Papoular formula[141]:

$$F_S = \frac{1}{2} W_p \sin^2(\theta - \theta_0) + \frac{1}{2} W_a \sin^2\theta_0 \sin^2(\varphi - \varphi_0) \qquad (1.16)$$

where Θ is a polar angle, φ is an azimuthal angle, W_p and W_a are respectively the polar and azimuthal anchoring strengths. In the SmA phase, orientational and positional order may be coupled at the interface and Durand *et al.* [142] have proposed that large deviations from the planar or homeotropic anchoring are equivalent to introducing dislocations in the SmA

phase and rquire a much higher energy than the anchoring energy associated to director deviation from the anchoring direction. Moreover, a mechanism of "positional" anchoring has been considered for the SmA phase were by the position of the lamella may be pinned on the surface.

1.6. Coupling with external fields

Due to high anisotropy of their electrical and magnetic properties, LC materials are very sensitive to external fields. In the presence of external electric and magnetic fields, LC molecules tend to align along the field or perpendicular to it, depending on the sign of anisotropic polarizability. We consider the case of an electric field of amplitude *E*, which is relatively easy to obtain in the laboratory using LC films and more relevant to practical application (e.g. LC displays). Also we consider weak field and assume that they are coupled to the director orientation without affecting the nematic or smectic order parameter. For *E* > 50 V/μm, the field may alter the nematic order and affect the Nem-SmA transition[143]. Under these assumptions, an electrostatic free energy density f_e is added to the nematic distortion energy f_N of Eq. 1.3. For a fixed voltage *V* applied to the LC film and anchoring conditions that do not induce any twist deformation (e.g. homogeneous planar or hybrid, Fig. 1.18), one has: $f_e = \varepsilon_a E^2 \sin^2\theta/2$, where θ is the director tilt from the boundaries and $\varepsilon_a = \varepsilon_{\parallel} - \varepsilon_{\perp}$ is the dielectric anisotropy. In the one-constant approximation $(K_{11} = K_{33})$ the free energy density is $f = (K\dot{\theta}^2 - \varepsilon_a E^2 \sin^2\theta)/2$ and Euler-Lagrange minimization leads, after a first integration, to the equilibrium equation $\xi^2\dot{\theta}^2 + \sin^2\theta = k^2$, where $\xi = (1/E)\sqrt{K/\varepsilon_a}$ is the electric coherence length and *k* is an integration constant. The solution can be cast in integral form:

$$z/\xi = \int_0^{\theta_z} d\theta / \sqrt{k^2 - \sin^2\theta} \qquad (1.17)$$

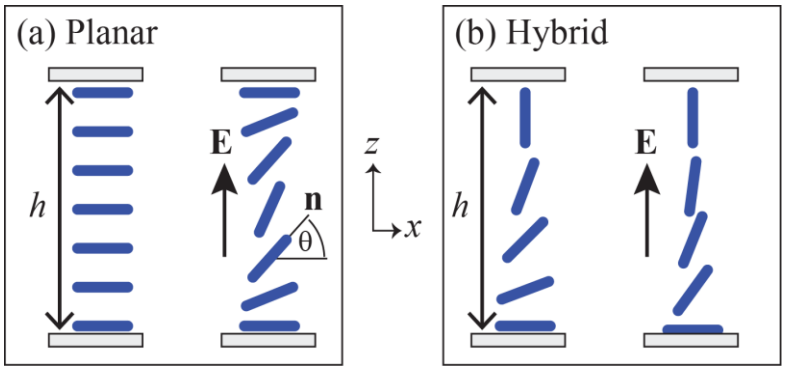

Figure 1.18: Applying an external electric field $E=V/h$ to (a) a LC film with homogeneous planar and (b) hybrid planar-homeotropic anchoring conditions

In the case of homogeneous planar conditions, $k=\sin\theta_m$ where θ_m is the tilt angle at the midpoint between the interfaces ($z=h/2$) (Fig. 1.18 (a)). The equilibrium equation admits two solutions: the trivial solution with $\theta_z=\theta(z)=0$, corresponding to the uniform planar director configuration, and a solution describing a distorted configuration:

$$z/\xi = u = \int_0^{\phi} d\lambda / \sqrt{1-k^2\sin^2\lambda} \tag{1.18}$$

where we have used introduced the variable $\sin\theta = k\sin\lambda$ in (Eq. 1.17) and the magnetic coherence length $\xi = \sqrt{K/\varepsilon_a}/E$. The distorted solution becomes energetically favorable when the voltage exceeds the Freedericks' threshold: $V_s = \pi\sqrt{K/\varepsilon_a}$. Notice, that $\xi = V_s/\pi E = hV_s/\pi V = hE_s/\pi E$. For common nematic liquid crystals such as cyanobipheils (nCB), V_s is of the order of one volt or less. The integration constant k can be determined as a function of the applied field using the relation:

$$h/2\xi = (\pi/2)(V/V_s) = \int_0^{\pi/2} d\lambda / \sqrt{1-k^2\sin^2\lambda} = F(k) \tag{1.19}$$

where F is the complete elliptical integral of the first kind. The director profile can be determined considering that $u\in[0,F(k)]$ in the range $z/h\in[0,1/2]$. The integral u in Eq. 1.18 is related to the first Jacobi function $\mathrm{sn}(u)=\sin\phi=\sin\theta/k$. Figure 1.19 (a) shows the

dependence of k on V/V_s for homogeneous planar anchoring conditions and Figure 1.19 (b) the director profile as a function of the V/V_s ratio. Both were obtained using Matlab with built-in code to calculate elliptic integrals and Jacobi functions.

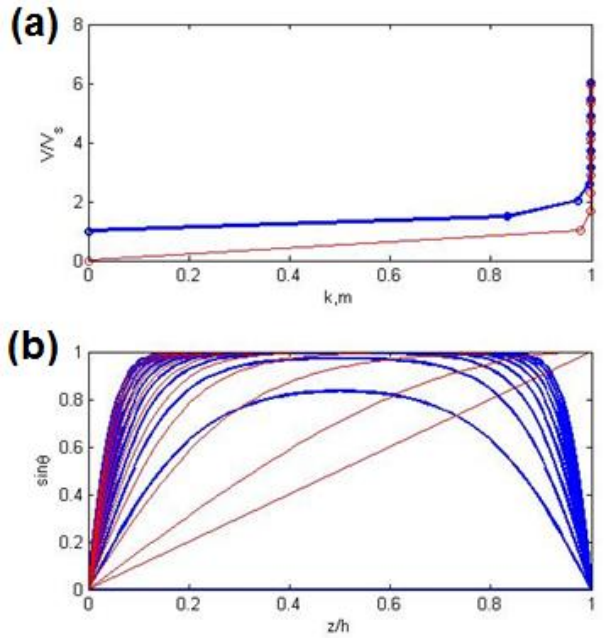

Figure 1.19: (a) Integration constants k and m as a function of the reduced voltage V/V_s for a LC with $\varepsilon_a > 0$. Thick blue lines correspond to the homogeneous planar anchoring conditions and thin red lines to the hybrid case (b) Profile of tile angle θ for different values of V_s/V. z is the distance from the surface inducing planar anchoring, h is the LC film thickness.

In the case of hybrid anchoring conditions (Fig.1.18 (b)), the integration constant is $k^2 = 1 + \xi^2 \dot{\theta}_h^2$ where $\dot{\theta}_h$ is the minimum of the tilt derivative, located at the surface inducing homeotropic anchoring ($z = h$). In this case, there is no trivial solution that satisfies the incompatible anchoring conditions. The director is always distorted and applying a field has the effect of thickening the region of the LC films where the director orientation is almost normal to the surface, i.e. close to the surface imposing homeotropic anchoring (Fig. 1.18 (b)). The integral (1.17) can be rewritten as:

$$z/\xi = mu = m\int_0^{\theta_z} d\theta / \sqrt{1 - m^2 \sin^2\theta} \qquad (1.20)$$

where $m = 1/k$ and the analogue of condition (1.19) is:

$$h/\xi = \pi V/V_s = mu = mF(m)\,. \tag{1.21}$$

Using Jacobi function we determined m and the director profile ($\sin\theta = \mathrm{sn}(u)$) as a function of V/V_s, shown in Fig.1.19. The director distortion near the surface inducing planar anchoring is similar for homogeneous planar and hybrid anchoring conditions when $V_s / V >> 1$. In this limit, $k,m \approx 1$ in this limit and both integrals (1.18) and (1.20) tend to: $z/\xi = \int_0^{\theta_z} d\theta/\cos\theta$.

As mentioned above, the bend constant K_{33} diverges at transition and therefore the one-constant approximation is no longer valid. In this case, a first integration of Euler-Lagrange equations gives $(K_{11}\cos^2\theta + K_{33}\sin^2\theta)\dot{\theta}^2 + \varepsilon_a E^2 \sin^2\theta = k^2$, which can be rewritten as [144]:

$$z/\xi = \int_0^{\theta_z} d\theta \sqrt{K_{11}\cos^2\theta + K_{33}\sin^2\theta}\,/\sqrt{k^2 - \sin^2\theta}\,. \tag{1.22}$$

For the same reasons outlines above (k, $m \rightarrow 1$), for high fields the director profile is again expected to be the same near the surface imposing planar anchoring for both homogeneous planar and hybrid anchoring conditions. The threshold voltage for the transition from uniform planar to distorted configuration for homogeneous planar anchoring conditions is $V_s = \pi\sqrt{K_{11}/\varepsilon_a}$, that does not diverge at the transition. On the other hand, near the transition $K_{33} >> K_{11}$ and the equilibrium equation becomes $\dot{\theta} = \mathrm{const}$. In the case of homogenous planar anchoring, this entails that the director is uniform, i.e. planar (const.= 0) whereas for hybrid anchoring conditions the director tilt increases linearly from zero to π/2 across the film thickness, in the same way as in the absence of a field. Therefore, the LC film become more 'rigid' at the transition from the Nem to SmA phase as it becomes increasingly difficult for the electric field to distort the director field induced by the boundary anchoring conditions.

1.7. The effect of inclusions on the LC order

Depending on the size R of dispersed inclusions in LC, which can be dye molecules, nanoparticles (NPs), colloids, inclusions of some other materials or phases, a

very different behavior is expected in LC matrix[95]. The particles can be homogeneously dispersed, form aggregates; can assemble in various ordered structures (see introduction, Fig. I.5 - I.7), eventually strongly modifying electro-optical properties of LC host[95-97,145-147]. When embedded into the LC matrix particles cause distortions, they result in an elastic energy cost of about KR, where $K \approx k_B T/a$ is the magnitude of the elastic modulus and a is the size of LC molecule[95]. When R is only slightly larger than a, entropic effects dominate and particles are likely to modify properties of LC matrix, such as the order parameter, but not the texture. In the case when $R \gg a$, LC matrix has to fulfill the anchoring conditions on the surface of the particles. Therefore the LC matrix may be strongly distorted by the particles presence. The energy cost of the anchoring effects is of the order of WR^2, where W is the surface anchoring coefficient. A maximum particle size, when the anchoring on the particle surface can be violated due to a high elastic cost, is defined by the surface extrapolation length $b = K/W$, which varies from 10 nm to 10 μm for thermotropic LCs, considered in this thesis.

For very small NPs, the topological defects may disappear, being replaced with a disordered area around NPs, or no disordered area, depending on the ligand around the nano particle[80,95]. This is true for a liquid crystal that do not contain distortion without nanoparticles, e.g. nematic LCs aligned by the interfaces. For LC films that are already distorted, the interaction between particles and LC may be slightly different, in particular in presence of topological defects[76,95].

In this thesis we examine a spatial distribution and alignment of nano-size objects of different nature and shape, such as dichroic laser dye molecules, semiconductor spherical quantum dots, dot-in-rods (DR) and spherical gold NPs, embedded into tunable SmA periodic patterns with expected topological defects and small defect cores, of an order of a few nanometers[148]. The effect of a particle size and increasing concentration (when the present in system topological defects are saturated with NPs and are not capable to embed all the dispersed particles) have been studied.

2. Materials and methods

2.1. Smectic materials

The majority of results presented in this thesis have been obtained using a specific LC compound (8CB, presented below) that has well-known chemical and physical properties and is commercially available, resistant to heat and light exposure and relatively easy to align using standard anchoring techniques. Other compounds have been considered for specific purposes, particularly to explore the effect of LC material properties, such as phase sequence and elastic constants, on the growth of periodic defect arrays.

8CB (4′-octyl-4-biphenylcarbonitrile, from Sigma-Aldrich) belongs to the cyanobiphenyl (*n*CB) family of LC, one of the most well-known and widely explored LC. It has rod-like molecules with a rigid biphenyl core to which are attached an aliphatic tail and a polar cyano head group (Fig. 2.1). Its molecular weight is Mw = 291.43 g·mol^{-1}.

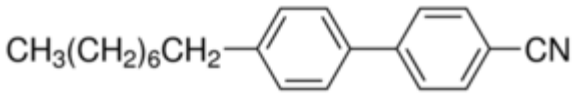

Figure 2.1: Molecular structure of 8CB.

8CB forms a bulk SmA phase at room temperature and undergoes a continuous SmA to Nem transition at temperature T_{NS} = 32.5 °C and a weakly first-order Nem to Iso transition. Below 21 °C, 8CB becomes a crystal (Cry) via a first order transition. Its complete phase sequence as function of temperature is[149]: Cry ↔ 21 °C ↔ SmA ↔ 32.5 °C ↔ Nem ↔ 40 °C ↔ Iso.

Due to its high stability against heat and light exposure, surface anchoring properties and availability of previous literature, 8CB was the choice material for our study. Key material properties of 8CB are listed below:

Table 2.1:

Material properties of 8CB

Smectic period, *a* (nm)	3.2 + 0.1	[44], [150]
Optical birefringence, δn T = 25°C, λ = 632.8 nm T = 32°C, λ = 589.3 nm	 0.165 0.166	 [151] [53]
Dielectric anisotropy, ε_a T = 33.4°C	9.25	[118]
Compressibility modulus, *B* (Pa) T = 25°C	$2 \cdot 10^6$	[152]
Curvature (splay) elastic constant, *K* (pN) T = 33.4°C	9.3	[118]

10CB (4′-decyl-4-biphenylcarbonitrile) has the same structure as 8CB except the alkyl tail, which has 10 carbon atoms instead of 8. The molecule length and diameter are 2.45 nm long and 0.5 nm[153]. Its molecular weight is Mw = 307.43 g·mol^{-1}. Pure 10CB has a direct 1st order Iso to SmA phase transition without Nem phase and a strongly first-order SmA to Cry phase transition. The 10CB phase sequence is[153]: Cry ↔ 44 °C ↔ SmA ↔ 51.6 °C ↔ Iso.

8OCB (4′-octyloxy-4-biphenylcarbonitrile, from Sigma-Aldrich) has the same structure as 8CB except the alkyl chain, which is linked to the phenyl ring via an oxygen atom (Fig. 2.2). Its molecular weight is Mw = 307.43 g·mol^{-1} and the phase sequence is[153]: Cry ↔ 54.5 °C ↔ SmA ↔ 67 °C ↔ Nem ↔ 75 °C ↔ Iso.

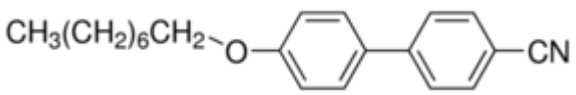

Figure 2.2: Molecular structure of 8OCB.

SCE-12 (from Merck, England) is a ferroelectric mixture with negative dielectric constant, showing the phase sequence[154]: Cry ↔ - 20°C ↔ SmC* ↔ 64 °C ↔ SmA ↔ 78.8 °C ↔ N* ↔ 118.0 °C ↔ Iso. SCE-12 molecules contain phenyl and biphenyl cores linked together by carbonyl bonds[155].

Chisso 1024. The ferroelectric LC CS-1024 (CHISSO Corporation) has the phase sequence [156]: Cr ↔ - 12°C ↔ SmC* ↔ 62 °C ↔ SmA ↔ 82 °C ↔ N* ↔ 90 °C ↔ Iso.

9004. The other ferroelectric LC compound 9004 has the phase sequence: Cry ↔ 35°C ↔ SmB ↔ 50 °C ↔ SmC* ↔ 62 °C ↔ SmA ↔ 73 °C ↔ Nem ↔ 87 °C ↔ Iso.

2.2. Functional molecules and nanoparticles

The idea of creating functional materials by mixing a self-ordered LC host with guest particles having specific properties can be developed in various directions, focusing on different properties (e.g. thermal conduction, charge transport, mechanical response) and materials (e.g. carbon nanotubes, polymer coils, magnetic particles, etc.). In this thesis we considered small molecules and nanoparticles whose optical properties, particularly light adsorption and emission, may be rendered anisotropic by a coupling with the ordered LC matrix. The choice is also dictated by physical and geometrical properties required for the qualitative analysis of the particles distribution and orientation into the LC host by means of fluorescent polarizing optical microscopy (FCPM), i.e. high efficiency of the materials in generating fluorescence and remarkable photostability, which enables long-term imaging experiments. FCPM technique, described in details later in this chapter (Chapter 2.5.3), allows 3D imaging of LC containing fluorophores and gives an information about the director distribution using the property of LCs to orient the fluorescent dye molecules and nanoparticles of anisotropic shape[157,158]. We therefore considered: small (low molecular weight) fluorescent molecules used as dichroic laser dyes, semiconductor nanocrystals and plasmonic metal nanoparticles. The small size of molecules and nanoparticles is important as it should not lead to significant distortions of the LC host. Moreover, when the particle size is comparable to the size of a defect core, a few nanometers in SmA LC[148], particles are expected to be localized close to or within the defects, as it is energetically favorable for particles to be trapped by defect cores in order to minimize the elastic energy of distortions they cause in LC host[76,95,145,159,160]. As a

consequence, we may expect the possibility of orienting and anisotropic assembly of particles due to the ordering of the defects[112,161]

The dichroic laser dyes are usually strongly fluorescent in presence of hydrophobic environment[162], mixable with LCs[163] and have sufficiently large (tens of nanometers) Stokes shift (the difference between the fluorescence and absorption wavelength), to allow the use of very small dye concentrations. Typically the presence of 0.005 - 0.010 wt% of dye is enough to get high contrast FCPM images and at the same time it does not affect the LC host[158].

2.2.1. Small fluorescent molecules

Coumarin 6 (from Radiant Dyes Chemie) is a very common and widely used laser dye with low molecular weight (Mw = 350.43 $g \cdot mol^{-1}$) and large quantum yield of 0.8 (i.e. the number of emitted photons per adsorbed photons)[164]. Coumarin 6 has an anisotropic molecular structure (Fig. 2.3 (a)). Due to its anisotropic shape, Coumarin 6 exhibits dichroism, i.e. it absorbs light more efficiently along one molecular axis than the other. The major component of the transition moment is along the long molecular axis and light polarized perpendicular to the long molecular axis is absorbed less than parallel polarization (the molecule is a positive dye)[165]. Coumarin 6 has a relatively high dichroic ratio[165] and a large Stokes shift (Fig. 2.3 (b)). It ethanol, it has an absorption band from 400 to 500 nm, peaking at 460 nm and an emission band from 450–700 nm, peaking at 502 nm.

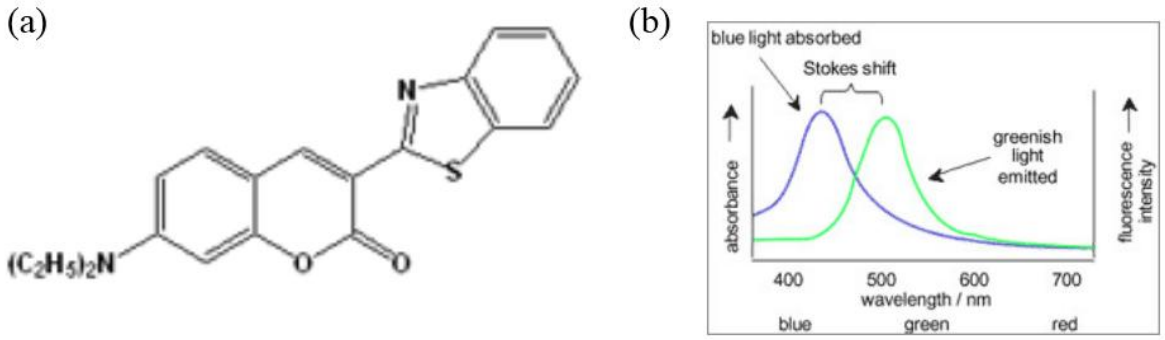

Figure 2.3: (a) Molecular structure, (b) absorption and emission spectra of dichroic fluorescent dye coumarin 6.

Nile red (NR, from Sigma Aldrich) is another small fluorescent molecule (Mw = 318.37 $g \cdot mol^{-1}$) with anisotropic shape and positive dichroism (Fig. 2.4 (a)). It has a long axis of about 1.1 nm[166], dichroic ratio 2[162] and shows solvent-dependent fluorescence with a high quantum yield of 0.7 [167]. When mixed with cyanobiphenyls (5CB), the absorption and emission maxima are respectively λ_a = (545 ± 5) nm and λ_e = (599 ± 5) nm (Fig. 2.4 (b))[162].

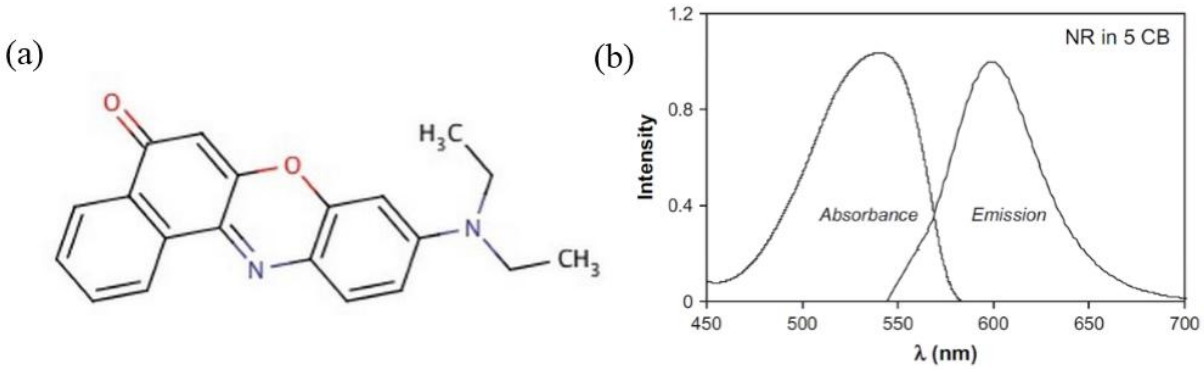

Figure 2.4: (a) Molecular structure, (b) absorption and emission spectra of nile red in nematic 5CB.

2.2.2. Semiconductor nanocrystals

Quantum dots (QDs) are fluorescent semiconductor nanocrystals, typically exhibiting strong absorption in UV and blue spectral regions and narrow emission spectra whose position is determined by geometrical parameters, such as particle size and shape. QDs are very efficient materials for generating tunable fluorescence. They have remarkable photostability, broad excitation and narrow, emission properties that enable long-term imaging experiments. Chemically grown CdSe QDs are probably the most extensively investigated object among semiconductor nanoparticles since the introduction of the concept of the "size quantization effect"[168].

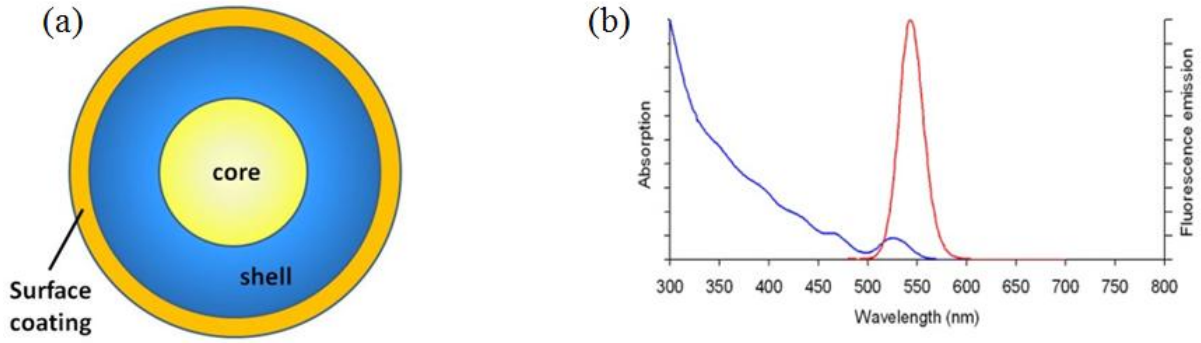

Figure 2.5: (a) Schematic illustration of the core/shell QD structure. (b) Typical broad absorption (blue line) and narrow symmetric fluorescence (red line) spectra of QDs.

The size-tunable fluorescence of QDs is attributed to the radiative recombination of electron-hole pairs, which involves the highest occupied and the lowest unoccupied quantum-confined orbitals[169]. The relation between the size R and the bandgap energy of electron-hole pair in semiconductor QDs ($E_{g,QD}$) is given by equation [170,171]:

$$E_{g,Qd} = E_{g,b} + \left(\frac{\hbar^2}{8R^2}\right)\left(\frac{1}{m_e} + \frac{1}{m_h}\right) - \left(\frac{1.8e^2}{4\pi\varepsilon_0\varepsilon R}\right) \quad (2.1)$$

where the first energy term $E_{g,b}$ is the bandgap energy of the bulk solid, the middle term is the quantum energy of localization and the last term represents the Coulomb attraction of the electron-hole pair. The m_e and m_h are the effective mass of the electron and the hole in the solid respectively, e is the elementary charge of the electron, $\hbar$ is Planck's constant, and ε is the dielectric constant of the solid. The quantum confinement term in Eq. (2.1) dominates as the particle radius R decreases, and the lowest excited state shifts to higher energy than $E_{g,b}$. In other words, the smallest QDs emit the light with the largest energy (smallest wavelength).

Both the fluorescence quantum yield and the emission spectrum width depend on the radiative recombination path. The large surface-to-volume ratio provides numbers of defects and imperfections on the surface of QDs which act as trap sites for charge carrier (electrons and holes). Having their own electronic energy states, often within the QD bandgap, surface trap sites lead to increase of a possible transitions number and non-radiative relaxation in particular, thus reducing radiative recombination efficiency and broadening the fluorescence spectrum. Moreover, although details are still unclear,

surface trap sites are believed to play a major role in fluorescence blinking, enhancing the non-radiative decay rates [172]. The suppression of negative effects caused by surface trap sites was recently achieved in single CdSe QDs by adding surface bound ligands [173,174] and by growing thick semiconductor shells around the QD cores, forming heterojunctions in so-called "core–shell" semiconductor QDs [175] (Fig. 2.5 (a)).

In this thesis, we work with two types of QDs:

a) Qdot® 545 ITK™ organic quantum dots from Invitrogen, USA, with an emission maximum $\lambda_e = (545 \pm 5)$ nm (Fig. 2.5 (b)). The 3.5 nm core, made of CdSe, is surrounded and stabilized by a semiconductor ZnS shell, improving both the optical and physical properties of the material. QDs have a lipophilic surface coating. They are provided as a suspension in decane.

b) QDs from PlasmaChem, Germany, with an emission maximum $\lambda_e = (530 \pm 5)$ nm consist of a quasi-spherical 2.5 nm CdSe core protected and stabilized by a 0.6 nm ZnS shell and coated with hydrophobic organic molecules. They are provided as a powder.

Dot in rods (DRs) are semiconductor nanoparticle with a rod-like appearance. The shape of the CdSe nanocrystals can be manipulated from a nearly spherical morphology to a rodlike one by controlling the growth kinetics of the nanocryslal[176] leading to an electronic structure transformation from a zero-dimensional (QDs) to 1-dimensional (nanorod) quantum system[177]. Nanorods provide several features beneficial for lasing applications, such as: dichroism and polarization dependent absorption and fluorescent emission; enhanced absorption cross sections and hence reduced lasing threshold and improved photostability; increased optical gain lifetime and extended optical gain spectral range[178]. A new class of nanorods shoving a large optical anisotropy and photostability was recently developed by growing a rod-like CdS shell around a spherical CdSe core. The new heterostructure was named dot-in-rod (DR)[179]. The relatively thick DR shell (about 2 nm comparing with the typical value of about 0.5 nm) together with a tuning of the shell length results in obtaining room temperature non-blinking single photon generation[180].

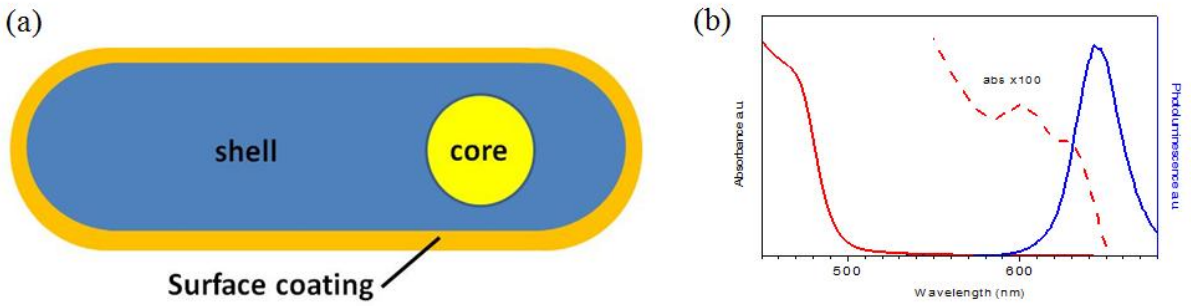

Figure 2.6: (a) Schematic illustration of the DR structure. (b) Absorption (red line) and fluorescence (blue line) spectra of DRs

In this thesis we considered core/shell CdSe/CdS DRs synthesized by a wet-chemical seeded-growth approach allowing a precise control of the heterostructure geometrical parameters and are described in details in ref.[179]. The DRs were provided by dr. Luigi Carbone from the CNR - Istituto di Nanotecnologia di Lecce. The CdSe spherical core has 2.9 nm diameter and was embedded in an anisotropic rod-like CdS shell (Fig. 2.6 (a)). The rod-like shell had an average length (55 ± 5) nm and total thickness ≈ 7 nm. The adsorption band extended in UV region with $\lambda < 500$ nm and the maximum fluorescence emission was $\lambda_e = (643 \pm 5)$ nm (Fig. 2.6 (b)).

2.2.3. Plasmonic metallic nanoparticles

Gold nanoparticles (Au NPs) due their unique optical properties are widely used in technology, biological and medical applications, organic photovoltaics, as electronic conductors, catalysis, in sensory probes, drug delivery and many other applications[95,97,145,181-185]. Au NPs properties are attributed to the combination of their size, much smaller than the light wavelength λ, and interaction of light with metal conduction electrons[186]. (Fig. 2.7). The interaction with light leads to accumulation of charges on the surfaces of NPs, producing Localized Surface Plasmon Resonance (LSPR) oscillations at a frequency that strongly depends on particle size, geometry and composition, as well as properties of the surrounding medium and inter-particle interactions.

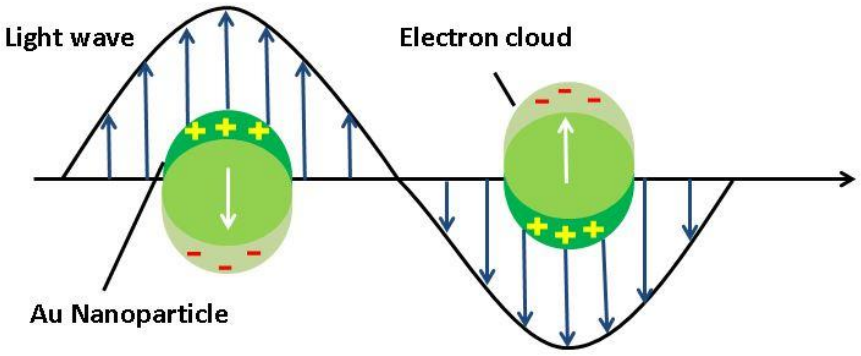

Figure 2.7: Schematic diagram illustrating a localized surface plasmon.

For the small isolated NPs with a radius $R < 0.1\ \lambda$ the extinction (absorption plus elastic light-scattering) cross-section C_{ext} can be found from Mie's solution of Maxwell's equation[181]:

$$C_{ext} = \frac{24\pi^2 R^3 \varepsilon_m^{3/2} N}{\lambda \ln(10)} \frac{\varepsilon_i}{(\varepsilon_m + \chi\varepsilon_m)^2 + \varepsilon_i^2} = C_{abs} + C_{sca} \qquad (2.2)$$

where C_{abc} and C_{sca} are the absorption and scattering cross-sections respectively, $\varepsilon = \varepsilon_r + i\varepsilon_i$ is the complex dielectric constant of the bulk metal, ε_m is the dielectric constant of the surrounding medium, N is the electron density and χ is the nanoparticle form factor which can varies from 2 for spherical nanoparticles up to 20 for nanorods with a large aspect ratio[81]. The characteristic plasma wavelength, λ_p, or plasma frequency, ω_p, of nanoparticle is a function of only the electron density, N, and the effective mass of electrons, m_e, in the bulk material:

$$\lambda_p = \frac{2\pi c}{\omega_p} = \sqrt{\frac{4\pi^2 e^2 m_e \varepsilon_0}{N e^2}} \qquad (2.3)$$

where c is the speed of light in vacuum and e is the elementary charge of the electron.

For spherical NPs the surface plasmon resonance is observed when $\varepsilon_r = -2\varepsilon_m$ (the Fröhlich condition), meaning enhancing of polarizability and internal polarization inside NPs as well as highly localized electromagnetic fields.

Depending on the NP radius the absorption or elastic light-scattering process may be more favorable in interaction with light waves. The absorption cross-section $C_{abc} \propto R^3$

and the scattering $C_{sca} \propto R^6$, so that absorption dominates for small particles, whereas particles of larger size scatter more light.

In quasi-static approximation a size dependence of plasmon resonance is introduced in Eq. 2.2 by assuming a size-dependent material dielectric function $\varepsilon = f(\omega,R)$ [81]. Experimental results presented on Fig. 2.8 show "blue-shifts" corresponding to the decrease of isolated particle size. Size dependence of the band width Γ or in other words full width at a half maximum (FWHM) is known to linearly depend on inverse particle radius[82]:

$$\Gamma = \Gamma^{bulk} + A/R \tag{2.4}$$

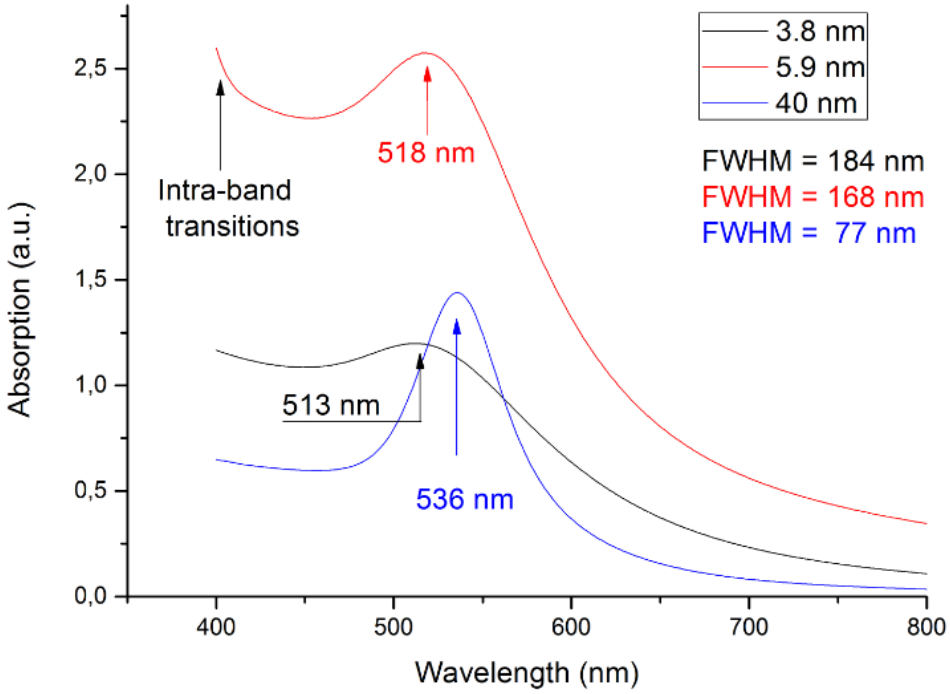

Figure 2.8: Absorption spectra of isolated Au NPs of diameter 3.8 nm (black line), 5.9 nm (red line) in toluene and 40 nm (blue line) in chloroform with the maxima at 513 nm, 518 nm and 536 nm and band width (FWHM) of 184 nm, 168 nm and 77 nm respectively, illustrating size-dependence of LSPR properties.

In this work we used quasi-spherical Au NPs of different sizes functionalized with ligands to avoid aggregation in toluene or chloroform solutions, listed below in Table 2.2. NPs exhibit homeotropic surface anchoring with LC molecules.

Table 2.2:

Properties of Au NPs solutions

Diameter (nm)	Mass of 1 NP (g)	Volume of 1 NP (m^3)	Solvent	LSPR peak (nm)	LSPR width (nm)
50	1.30E-15	6.54E-23	chloroform	540	75
40	6.66E-16	3.35E-23	chloroform	536	77
30	2.81E-16	1.41E-23	chloroform	526	87
10	1.04E-17	5.23E-25	chloroform	520	118
5.9	2.07E-18	1.04E-25	toluene	518	168
3.8	6.66E-18	2,87E-26	toluene	513	184

2.2.4 Mixing particles with liquid crystals

The mixtures of nanoparticles (DRs, QDs, Au NPs) and dyes in LC were made by first taking suitable volumes of 8CB in its isotropic phase using a micropipette and dissolving it in a known amount of organic solvent (chloroform or toluene). Particles were then added from a solution in the same solvent. Solutions containing Au NPs and dyes were placed on a heating stage or in an oven for 2 – 3 hours at $(50 – 60)^0$ C to let the solvent evaporate, as they should not be affected by such a temperature and we could avoid printing of ordered LC phases on the particle surfaces by keeping solutions in Iso phase[38,39]. DRs and QDs solutions were dried in a low vacuum at ambient temperature for 24 – 48 hours, to avoid heat degradation of semiconductor crystals. After the solvent was evaporated, the final concentrations of particles were: 0.3 mM for dyes, 1 pM – 0.1 mM for nanoparticles.

2.3. Surface alignment of liquid crystal materials

Obtaining well-defined and strong anchoring of the LC was the key to create periodic arrays of SmA defects. Indeed, defects are created when the LC director and SmA lamellar arrangement are subjected to large deformations and contain a high density of free elastic energy, which can be induced and held in place only if the anchoring is strong enough. The anchoring should also be stable from the chemical-physical point of

view, i.e. it should not be degraded over time by the adsorption of contaminant or functional particles present in the LC, or by repeated cycles of heating and cooling above and below the SmA phase transition. In this thesis, we have considered various methods for treating the surface and obtain either planar (parallel to the surface) or homeotropic (normal) anchoring

Planar anchoring was obtained on polymer coatings of polyvinyl alcohol (PVA) and polyimides (PI), and crystalline substrates of muscovite mica and MoS_2. Unless a specific in-plane direction is created on the polymer surface, the anchoring is degenerate. By exposure to orientationally ordered LC phases initially isotropic or degenerate planar anchoring on the polymer substrate can be rendered strongly anisotropic[38,140]. This phenomenon is known as print or surface memory effect. Unidirectional planar anchoring, possibly with a small tilt angle, can be produced by rubbing the polymer layer with velvet cloth [138]. The mechanism of the alignment involves the LC molecules lying in the periodic microgrooves generated by rubbing with their long axes parallel to the groove direction and Van der Waal's interactions at the interface between LC and oriented polymers at alignment-layer surfaces. Rubbing may also produce high localized heating that leads to melting of one of the polymer materials.

Anchoring on crystalline surfaces such as cleaved mica or MoS_2 is also planar. The anchoring is unidirectional on mica and multidirectional on MoS_2. The anchoring directions are very well defined on such substrates and lead to very 'clean' LC texture without surface imperfections and unwanted defects over large area. However, anchoring on mica is easily contaminated and altered by ambient volatile molecule that induce transitions to other planar anchoring direction and even homeotropic anchoring. Moreover, mica is birefringent, with an easy axis oblique to optical axis, and MoS_2 is opaque to light. Therefore mica is unsuitable for optical polarization studies and MoS_2 cannot be used in experiments based on light transmission through the interfaces performed in this thesis. For this reasons we were mainly using transparent polymer films as the aligning surfaces.

Poly-imide (**PI**-2555, from Hitachi Chemical DuPont MicroSystems GmbH) was dissolved in NMP (1-methyl 2-pyrrolidinone) at 5 wt% concentration and deposited on glass following these steps: spin-coating for 2 seconds at 400 rpm (slow spin) to spread the drop over the entire surface; rotation for 60 seconds at 3600 rpm (fast spin); soft-

baking at 80°C for 30 min to evaporate the solvent and hard-baking at 250°C for about 1h to cross-link the PI polymer chains; and rubbing of the layer for 3 times always in the same direction.

Poly(vinyl alcohol) (PVA, M_w = 85.00-124.00 $g \cdot mol^{-1}$, from Sigma Aldrich) was dissolved in DI water at 0.5 wt% concentration using a magnetic stirrer while heating up to 100 - 170 °C for a few hours. The polymer was deposited on glass following these steps: spin-coating for 30 seconds at 3000 rpm with an acceleration time of 2 seconds; hard-baking of the layer at 100°C for 60 minutes; and rubbing for 3 times always in the same direction.

MoS_2 is a layered single crystalline substrate that can be easily cleaved to obtain a clean surface parallel to the basal planes. The orientational and positional order of the molecules in the surface monolayer is arising from specific substrate-molecule interactions. Aliphatic chains of LC molecules lie flat on the surface and perfectly register with the crystalline structure which results in two-dimensional order, with the molecules arranged in straight rows, and a registration between molecules of adjacent row[187] forming domains of different molecular orientations separated by a grain boundaries[39]. With nCB molecules, the order is higher for longer aliphatic chains and, i.e. larger values of n[188].

Large-area (up to 1 cm^2) atomically smooth surfaces with the same crystallographic plane can be obtained by cleaving another layered alumino-silicate crystal, **mica**[74]. The compounds of the nCB series generally are oriented with their molecular axes parallel to the substrate, making an angle of 60° with the optical axis of the mica slide[187].

Homeotropic alignment was obtained using a silane surfactant octadecyl-trichloro-silane (OTS, from Sigma Aldrich). The OTS molecules form a covalent bond with a hydroxyl group on glass and on the surface of Indium-Tin-Oxide (ITO), a common material for transparent electrodes (see below) [189]. The ionic head of OTS becomes anchored to the substrate while a non-polar tail is pointing from it (Fig. 2.9). The aliphatic tail attracts and orients the carbon chain of the LC molecule inducing orientation perpendicular to the substrate[138].

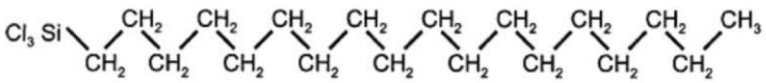

Figure 2.9: Chemical structure of OTS.

OTS was deposited on glass or ITO following these steps: 1 mg of OTS was dissolved in a 90/10 w/w solution of n-hexane/chloroform, corresponding to 2.5mM of OTS; surfaces were dipped in the solution for 20 min while sonicating to avoid aggregation; surfaces were rinsed with chloroform, baked for or 60 min at 110°C, then if needed sonicated in chloroform for 5 – 10 min to remove aggregates from the surface.

Cleaning procedures are important to determine the adhesion and stability of anchoring layers on support surfaces of glass and ITO. The procedure used throughout this thesis was the following:

1. Ultrasonicate the surfaces in DI water mixed with detergent for 5 minutes.

2. Rinse several times in DI water, then sonicate for 5 minutes in DI water.

3. Sonicate 5 minutes in acetone.

4. Sonicate 5 minutes in chloroform.

5. Dry and then do plasma cleaning for 7 - 10 minutes at maximum power.

6. Do the coating immediately after plasma cleaning.

If the surface had to be very clean, then the procedure began with a cleaning step in piranha solution (3:7 v/v solution of hydrogen peroxide in sulfuric acid). When the glass was very dirty, surfaces were wiped with soap and ethanol.

2.4. Sample and cell fabrication

2.4.1. Sessile droplets and spin-coated films

Droplets of LC with nL volume were deposited on the substrate in the nematic or isotropic phase using a thin copper or tin wire. The droplet was left spreading on the

surface in the nematic or isotropic phase until it reached the desired thickness at its edges. Spreading was arrested by cooling the in SmA phase due to the increase of viscosity. This method allows creating very thin droplets but has three main limitations. First, wetting and spreading may not occur for particular combinations of LC and substrate. In fact, isotropic 8CB does not spread on the surfaces and the droplet must be spread in the nematic phase, putting the anchoring in competition with flow alignment. Second, sample thickness cannot be fixed *a priori* as it depends on LC wetting and spreading, typically leading to complex non-spherical droplet shapes. Third, the shape of the air interface is unknown as the stress inside the LC droplet may deform the interface at various length scales [38].

To avoid non-uniformity of sample thickness, in some experiments the LC was spin coated on the surface from a solution with organic solvent (toluene or chloroform). On PI and PVA, a 30 - 40 microliter droplet of 0.2 M (8CB or 9004) solution in toluene was spin-coated for 30 seconds with a speed of 1800-2000 rpm and acceleration time 2 seconds. While spinning the organic solvent was completely evaporating and thin LC film of thickness about (200 – 600) nm was produced.

2.4.2. Closed cells

Closed cells with two rigid boundaries confining the LC, typically treated glass slides or thick mica plates, have many advantages compared to thin films. First, the cell can be closed and then filled with LC via spreading and capillary action or, when these are absent, by pumping the LC in with hydrostatic pressure. Therefore, there are no more restrictions in the choice of LCs and surface coatings to be use due to the wettability, and the cell can always be filled with LC in the isotropic phase. Second, the LC thickness can be controlled *a priori* by putting a proper spacer between the boundaries (Fig. 2.10). Third, the interface geometry is flat and rigid. Last. But most important, the boundaries can be coated with a thin layer of conductive ITO that enables applying an external electric field.

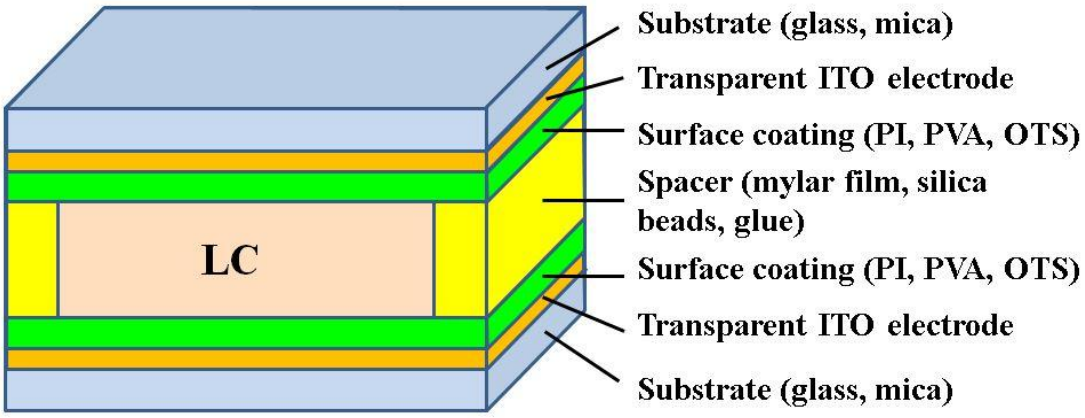

Figure 2.10: Schematic illustration of closed cell geometry.

Cell spacers and gluing. The cell was closed using a few droplets of UV adhesive after inserting mylar film of thickness (2.5 – 100.0) μm or silicon beads of diameter (1.4 – 2.1) μm. For very thin cells, no spacer was used but the UV glue droplets were squeezed to a thickness less than 1 μm. In some cases, two different spacers were used to create a wedge cell that allowed investigating the effect of thickness variations in a single sample. The angle between the cell boundaries was typically smaller than 1 mrad. Norland Optical Adhesive 61 UV glue (NOA 61 from Norland Products Incorporated, USA) is a liquid photopolymer that cures when exposed to ultraviolet light (UV)[190]. The curing time depends on the glue film thickness and the amount of available UV light energy. The energy required for obtaining full crosslinking and solvent resistance of the adhesive is 3 Joules/cm^2 in the range (350-380) nm of the glue maximum absorption. Using a 100 W mercury lamp the precure can be obtained in 10 seconds. It has to be followed by a longer time deposition to the UV light. With the same mercury lamp in 5 – 10 minutes the glue will be fully cured. NOA 61 reaches its optimum adhesion to glass in about 1 week at the ambient conditions or by aging at 50^0 C for 12 hours. After aging the glue has a high thermal stability, it withstands temperatures from -150^0 C to 125^{0}C.

ITO-coated glass was either purchased from commercial sources or deposited by sputtering in prof. Carlo Versace's laboratory at the University of Calabria. Sputtering was used to create conductive ITO electrodes on thin cover slips to be used with high numerical aperture microscope objectives having a short focal distance. We used cleaned borosilicate glass coverslips of thickness (0.13 – 0.17) mm (see cleaning procedure above)

from different sources. The layer of indium-tin-oxide (ITO) was deposited in a horizontal in-line sputtering system (Edwards Auto 306) by bombarding the target material with high-energy ions from a plasma (Fig. 2.11). The system was equipped with two magnetron guns and DC power supply (MDX 15.K, Advanced Energy: 500 V, 3 A 1.5 kW) which generates plasma in the deposition chamber. 7.5 cm in diameter and 6 mm thick target of In_2O_3/SnO_2 in a 90/10 wt% ratio have been used. The target to substrates distance was 8 cm. The deposition parameters we used were: pre-vacuum 9.0·10-5 mB, vacuum $4.8 \cdot 10^{-2}$ mB, power 40 W, time 2 minutes, resulting in 50 nm thick transparent uniform ITO layer.

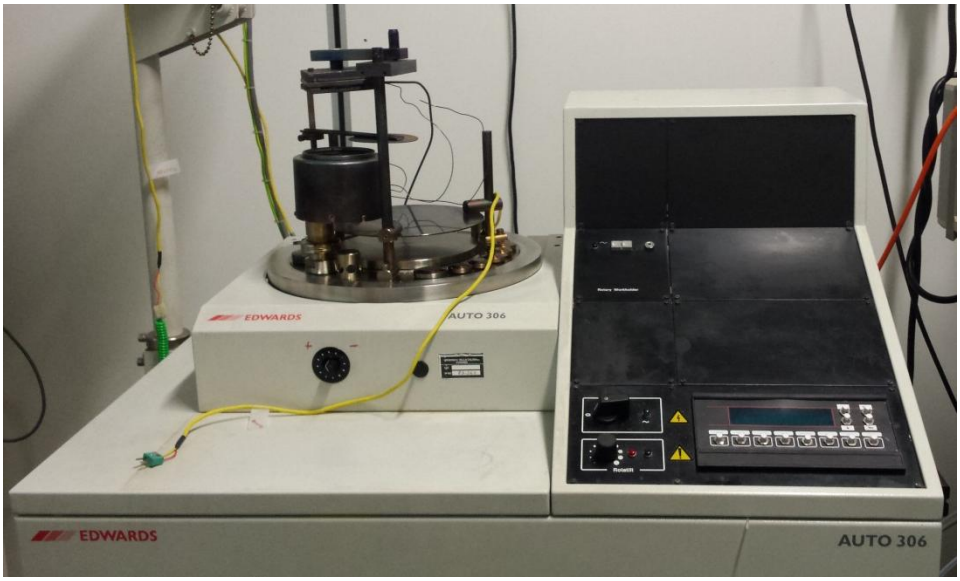

Figure 2.11: Sputtering system (Edwards Auto 306) used for ITO conductive layer deposition.

Commercial ITO coated glass of thicknesses (1.0 ± 0.1) mm and the ITO layer thickness of about (150 - 200) nm was always used as one or both substrates for cells assembling in the experiments where electric field application was required. Indeed, the presence of at least one rigid substrate is necessary for fabricating cells thicker than 1 μm. An excessive flexibility and fragility of the coverslips makes it impossible to do any manipulations with samples made of two coverslips without disturbance of LC alignment.

The ITO electrodes were patterned with strips as shown in Fig. 2.12 to create cells where voltage could be applied on selected pixels or strips. This was particularly useful to avoid short-circuiting produced by accidental local contact between the electrodes, e.g.

due to dust particles or scratches of the ITO layers in regions with thickness smaller than 1 μm.

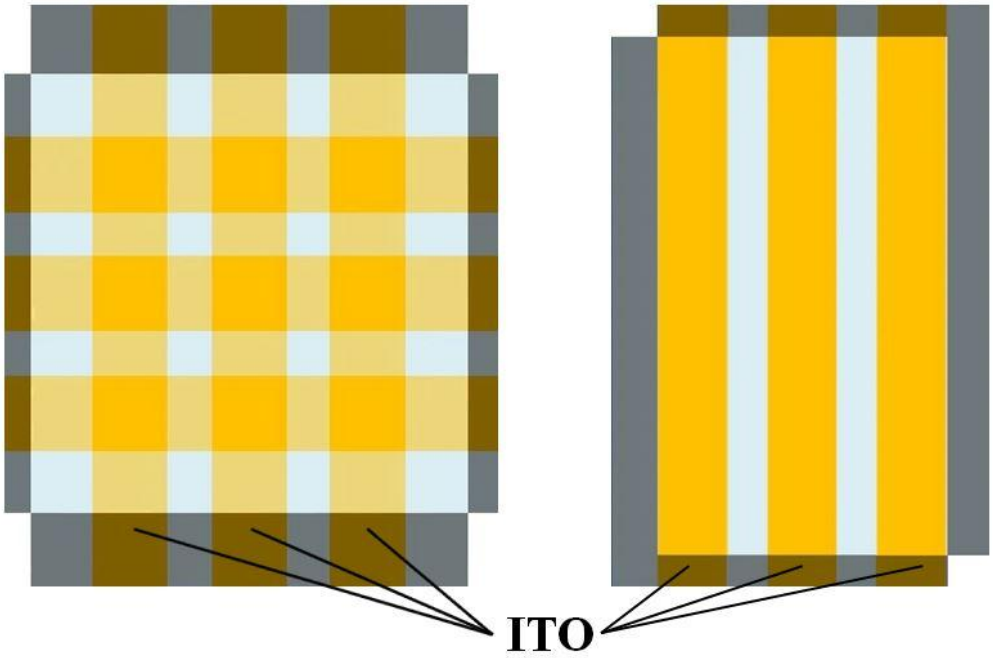

Figure 2.12: Schematic illustration of ITO electrode patterning with working (a) pixels and (b) stripes. Both surfaces were patterned with ITO strips, that are crossed in figure (a) and aligned in figure (b).

To produce the strips, the ITO coated glass was first masked with a pattern made of adhesive tape. The ITO layer was carefully covered to avoid air bubbles and dust beneath the tape. Then the glass slides were dipped into chemical reagents that attacked and removed ITO from the non-protected zones. The reacting solution was made with 10 parts DI, 10 parts hydrochloric acid (HCl) and 1 part sulphuric acid (H_2SO_4). Notice that the reagents must be mixed in this order to avoid explosion and the work must be done in a chemical fume hood. The mixture was stirred at the maximum rotation for 3.5 minutes at 20 °C. The masked ITO samples were dipped into the solution, which temperature was previously increased to 50 °C, while it was stirred for 7 minutes. Then samples were dipped into distilled water for 3 minutes, additionally cleaned with distilled water and dried. The procedure may be repeated if the conductive layer was not completely removed. For further glass treatment the tape musk was taken out and the glass cleaned

from remained adhesive with a paper towel rinsed in ethanol, then cut and cleaned following standard procedures.

2.5. Optical microscopy

2.5.1. Multiple-beam interferometry for thickness measurements

When the spacer thickness in closed cell was smaller than 15 μm, the cell thickness h was measured before filling the cell using an interferometry scheme that combined an optical microscope with a spectrophotometer (AvaSpec by Avantes). White light from the tungsten lamp of the microscope was collimated on the cell region of interest. Depending on experimental needs the thickness could be measured locally or as an average over a large sample area by choosing a proper objective magnification and opening/closing a diaphragm. Light wave underwent multiple reflections in the cell between partially reflecting cell boundaries. The transmitted spectrum showed maxima of intensity corresponding to constructive interference at wavelengths λ_q such that $2\pi h/\lambda_q = hk_q = \pi q + \varphi_1 + \varphi_2$, where q is the chromatic order, which represents an optical path difference between interacting beams in parts of λ, k is the wave vector, and φ is the phase shift upon reflection on the aligning layer coating the cell boundary. Therefore, the transmitted intensity is a periodic function of $k = 2\pi/\lambda$ and we determined h by measuring the period $k_q - k_{q-1} = \pi/h$. This technique allowed to measure the cell thickness with a resolution much better than 1 μm, but it was limited to thickness below 0.4 μm because of limited resolving power of the spectrophotometer (i.e. the distance $k_q - k_{q-1}$ between two neighboring peak could not be resolved in the transmitted spectrum).

The thickness of open LC films deposited on reflective PI/glass or PI/Si interface was measured in a similar way, assuming that the phase of light waves traversing the LC film was proportional to the h and a phase shift upon reflection at the interfaces was zero. The LC sample appeared as a sequence of alternating bright and dark fringes when illuminated in reflection mode with the microscope light filtered through a green bandpass filter with $\lambda = (543 \pm 3)$ nm (Fig. 2.13). Fringes were observed due to a gradual increase of h going from the droplet edge. Bright fringes corresponded to $nh=2q\delta h$ and dark fringes to $nh = (2q+1)\delta h$ with $q = 0,1,2...$ and the refractive index n averaged on the film thickness. By counting the interference fringes, we could measure thickness variations as

small as $\delta h = \lambda/4n$, which is the difference between a dark fringe and the next bright fringe.

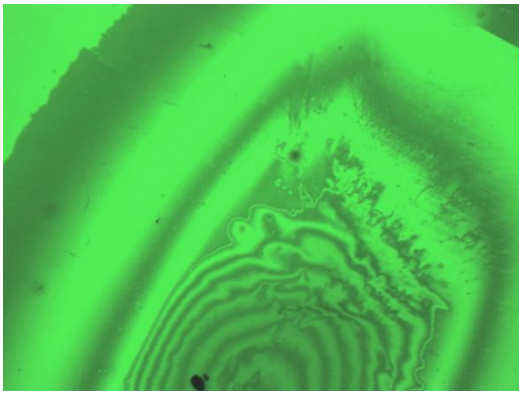

Figure 2.13: SCE12 droplet on PI/Si surface. Optical fringes indicate thickness increase by λ/4·n starting from the droplet edge (a first dark fringe in a top left part of the image).

2.5.2 Polarized optical microscopy (POM) and compensation

POM is widely used in LC study as a tool for determining the alignment of the director **n.** The LC sample is put between a polarizer *P* and an analyzer *A* that are either crossed at 90° or parallel to each other. The light intensity transmitted through *A* depends on both the polar orientation of **n** relative to the *A*-*P* plane and the in-plane azimuthal orientation. For fixed polar orientation of **n** and $A \perp P$, the transmitted light depends on the azimuthal angle ϕ between **n** and *P:*

$$I = I_0 \sin^2(2\varphi) \sin^2(\pi\delta nd/\lambda) \quad (2.5)$$

where *I* is the intensity of transmitted light, I_0 is the incident light intensity and δn is birefringence.

For A||P and fixed polar orientation of n, the light transmitted through A depends on the azimuthal angle ϕ between **n** and *P*:

$$I = I_0[1 - \sin^2(2\varphi) \sin^2(\pi\delta nd/\lambda)] \quad (2.6)$$

Therefore, the sample looks completely dark when ϕ = 0 or 90° and shows maximum brightness when ϕ = 45°. The polar orientation can be determined by measuring the phase retardation $\Gamma = h\delta n$, where $\delta n = n^* - n_o$ is the birefringence:

$$n^* = \int_0^h [(sin\theta(z)/n_e)^2 + (cos\theta(z)/n_o)^2]^{-1/2} dz \qquad (2.7)$$

$\theta(z)$ is the variable angle of tilt between the optical axis (i.e. **n**) and the microscope axis (normal to the LC film) z. n_o and n_e are respectively the ordinary and extraordinary refractive indices of LC. Notice that $\Gamma/h = 0$ and $\Gamma/h = n_e - n_o$ when the average polar angle across the film thickness is $\theta = 0$ and $\theta = 90°$, respectively. To measure Γ, a Berek titl compensator (from Leica, Germany) was placed with its optical axis at -45° with the polarizer. When the LC appears completely dark at the center of the microscope's field of view, the phase retardation read on the compensator is equal to Γ.

2.5.3 Fluorescence Confocal Polarized Microscopy

Fluorescence Confocal Polarizing Microscopy (FCPM) is a useful technique to visualize the alignment and distribution of the optically anisotropic materials and has been successfully used to study three-dimensional director structures of defects in nematics[158], cholesterics[157 191] and smectic A [38,157] LCs (Fig. 2.14).

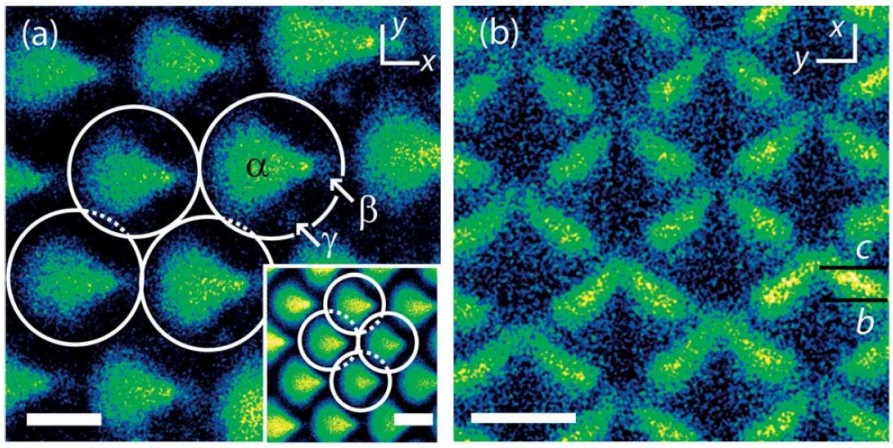

Figure 2.14: FCPM images of focal conic domain lattice in SmA 8CB film on mica obtained with the polarizer parallel to x (a) and perpendicular to x (b). Inset in (a): a thinner region of the 8CB droplet[38].

FCPM is based on the polarization-dependent light adsorption and polarized emission of anisotropic fluorophore that align with the director. Its principal scheme is shown in Fig. 2.15. A confocal microscope is equipped with a linear polarizer *P* introduced before the dichroic mirror, so that it polarizes both the excitation light and the fluorescent light emitted by the fluorophore. The linearly polarized incident light focused on the sample by the objective lens excites the fluorescence emission in a small voxel (volume pixel). The light coming from the voxel passes through the pinhole located in the focal plane of the collector lens and conjugated to the focal plane of the objective, i.e. the probed voxel and the pinhole are confocal and therefore the signal from the neighboring region is prevented from reaching the detector. The measured FCPM intensity is maximum when the transition dipole of the fluorophore is parallel to *P* and minimum when is perpendicular (see an example in Fig. 2.14). Namely, the intensity scales as $I \propto cos^2\alpha cos^2\alpha'$, where α and α' are the angles between the transition dipole and the light polarization at the moment of absorbing and emitting a photon. In the case of NR and Coumarin 6 used in this thesis, the transition dipole is oriented along the long axis of the molecule (Figs 2.3 and 2.4) both during adsorption and emission. The lifetime of the excited state (time delay between the acts of adsorption and fluorescence emission) is $\tau \approx$ 4 ns and it is smaller than the characteristic time of rotational relaxation $\tau_0 \approx 6$ ns of the dye in the liquid crystal matrix[162]. Therefore, the detected FCPM intensity is $I \propto cos^4\alpha$ [158].

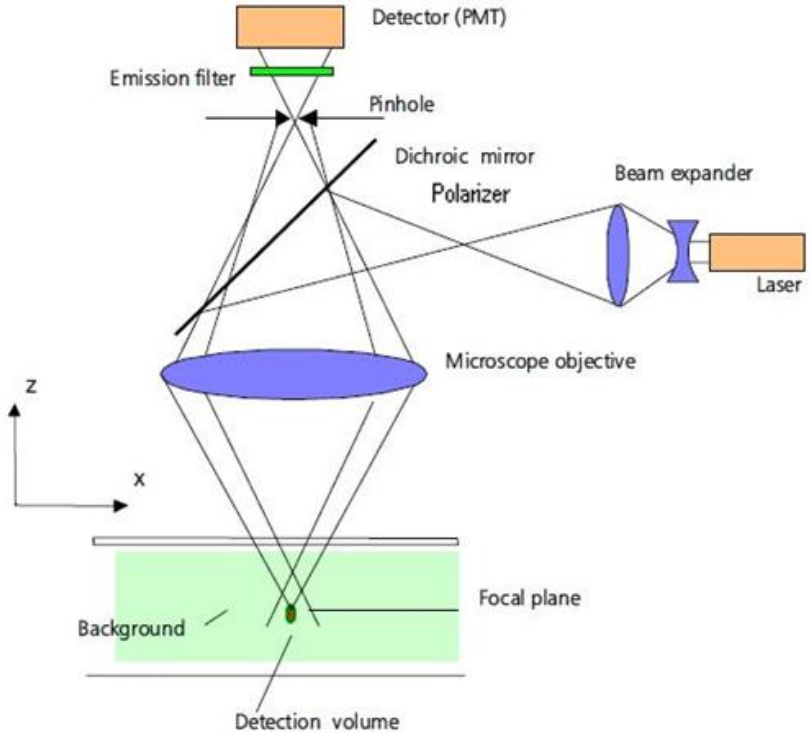

Figure 2.15: Schematic of the FCPM setup for observations in the reflection mode[192].

Coumarin 6 and NR are known to align with their long axis parallel to the director **n** in cyanobiphenyl materials such as 8CB (Fig. 2.1)[38,53]. Therefore, bright and dark areas in FCPM images correspond to regions where **n** is parallel and perpendicular to *P* respectively. By taking FCPM images on various image planes, a full tomographic, i.e. 3D reconstruction of the LC sample interior can be obtained.

Dots-in-rods (DR) also show polarization-dependent light absorption and emission[179,193]. The transition dipole is directed along the main rod axis[179,112]. Due to the large particle size compared to small dye molecules such as NR, the rotational relaxation time of a DR particle is expected to be much larger than the excitation lifetime $\tau \approx \hbar/E$ where E is the semiconductor bandgap energy. Therefore, DRs are expected to share the optical behavior of Coumarin 6 and NR. As we will see in Chapter 5, DRs also align with director of 8CB in the SmA phase. On the other hand, quantum dots (QDs) are expected to be insensitive to both polarization and director alignment. In any case, the surrounding LC matrix must be carefully considered when the measured fluorescence signal is analyzed

due to possible optical effects such as polarization rotation and lensing that may strongly distort the fluorescent intensity distribution.

In this thesis a Zeiss LSM 710 inverted confocal microscope (from Carl Zeiss MicroImaging GmbH, Germany) with a 63x Plan-Apochromat DIC oil immersion objective with numerical aperture NA = 1.4 and working distance WD = 0.19 mm was used in reflection mode. The fluorophores were excited using an argon blue-green laser with wavelength 488 nm. The emitted light was collected in a spectral range 500 – 750 nm. The inherent fluorescence from the 8CB did not affect our measurements. Its maximum value corresponds to 400 nm and goes down to zero before reaching 500 nm in the working temperature range (20 – 45) °C[149]. The microscope was equipped with a heating stage to allow phase transition of the LC samples. Tomographic reconstructions of the sample interior were obtained by combining images taken in *xy* (horizontal) plane, parallel to the LC film, with section taken (vertical) *xz* and *yz* planes. Also notice that the microscope axis, *z*, is chosen to be normal to the LC film. The resolution is that of the confocal microscope upon which the PCFM setup is build, namely about 300 nm in the *xy* plane and about 500 nm along *z*.

2.5.3 Dark-field microscopy (DFM)

In DF microscopy, the unscattered beam is excluded from the image. For this reason the optical microscope is additionally equipped with a specially sized disc, a patch or annular stop which are used to create a cone of oblique illumination by partially blocking an incident light (Fig. 2.16). The condenser lens focuses the light at the sample. If there are no reflective objects, all the light will be transmitted and omitted due to the presence of a direct illumination block. Only the scattered light will enter the objective, creating a high-contrast bright image at the dark background.

We used DF microscopy for investigations of 8CB samples doped with Au NPs of diameter d = (30 – 50) nm, as it is known that starting from nanoparticle size of about 30 nm scattering begins to be significant [181].

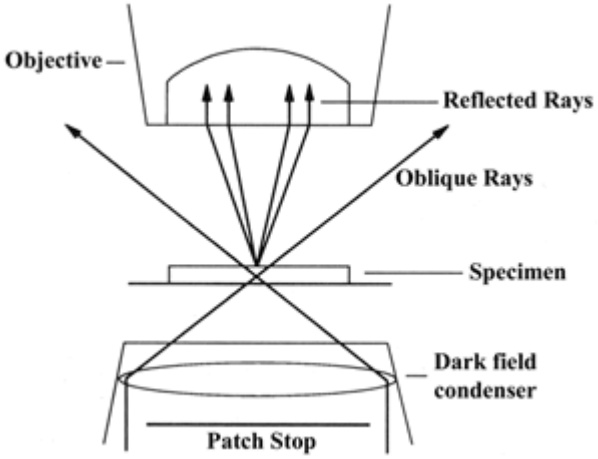

Figure 2.16: A principal scheme of dark field microscopy[194].

Direct comparison of linear defect array containing Au NPs pictured with a help of optical microscope in DF mode and bright field mode under the crossed polarizers suggests that scattering from Au NPs is veiled by much stronger signal coming from anisotropic LC matrix.

3. Closed cells with hybrid anchoring conditions

In the past few years, thermotropic smectic A (SmA) liquid crystals (LC) have emerged as a promising class of materials for creating large-area 1D[39,74,76,100] and 2D[38,66-70,195] periodic micropatterns to be used in application such as guided assembly of dispersed colloids and nanoparticles[68,76,95,100], soft lithography[72,196] and microlens arrays[73]. The main feature of the SmA patterns and arrays is the presence of topological defects that are nucleated in films subjected to incompatible (hybrid) homeotropic-planar anchoring conditions. The director field **n**, and the orientation and shape of the smectic lamellae results from the balance between bulk elastic (structural) forces due to layer deformation, surface anchoring and geometrical boundary conditions. To satisfy anchoring conditions, the lamellae are expected to bend in a curved shape, which is schematized in Figure I.1. The deformation field is associated with singularities – disclinations and dislocations lines, and wall defects (Chapter 1.4.) – and may be partially released by allowing local departures from the anchoring conditions[38] and/or confocality rule [197-199]. Defects interact with each other and with the interfaces via long-range elastic forces generated by the deformation, and self-assemble into multi-defect domains whose symmetry reflects that of the interfaces. Surfaces that do not impose any particular in-plane alignment, such as degenerate parallel (planar) and normal (homeotropic) anchoring, produce axially symmetric defect domains known as toroidal focal conic domains (FCDs) that self-organize into close-packed hexagonal lattices[66,67,69,72,73] (Fig. I.2). On the other hand, oriented 1D arrays of straight linear domains (LDs)[39,74-76,100] (Fig. I.4) and lattices of eccentric FCDs[38,70] (Fig. I.4 and 1.13 (d)) are created at the interface between air, inducing homeotropic anchoring, and substrates inducing unidirectional planar anchoring.

In this thesis, we have considered for the first time the effect of external electric fields on the formation, morphology and period of defect arrays formed in SmA films sandwiched between rigid electrode plates under hybrid anchoring conditions. The electric field was applied normal to the plates and the director **n** tended to align parallel or perpendicular to the field for positive and negative dielectric anisotropy of LC respectively. We were able to create highly oriented 1D arrays and 2D lattices and control the pattern type (1D/2D) and period by varying the film thickness and/or the applied electric field. Striped patterns were stable over the entire temperature range of the SmA

phase, as opposed to transitional effects reported in Cladis and Torza[200]. In contrast with field-driven electro-hydrodynamic patterns observed in the nematic (Nem) phase (Williams domains[44]), our patterns corresponded to static arrangements of the SmA lamellae. Pattern morphology could be controlled at the Nem → SmA but remained largely unaffected by field variations applied in the SmA phase. Therefore, the system was bistable in the SmA phase, i.e., different pattern morphologies could be obtained for a same voltage depending on the voltage applied during the N-SmA transition. Such behavior indicates that large energy barriers hinder the rearrangement of defect patterns in response to applied fields

3.1. Field-off patterns

Fig. 3.1 shows large-area periodic arrays of LDs obtained in the SmA phase of two thermotropic LCs, 8CB and SCE12. The phase sequences of these compounds are given in Chapter 2.1 and include a chiral phases for SCE12. 8CB and SCE12 differ in their chemical-physical properties, e.g. the dielectric anisotropy, ε_a, is positive for 8CB and negative for SCE12 (see Chapter 2.1). The samples were confined to a thickness $h \leq 2$ μm in a closed hybrid cell geometry using the procedure described in Chapter 2.4.2. As a planar aligning layer we used rubbed polymer polyimide (PI), whereas homeotropic anchoring was obtained using OTS. Under a Polarizing Optical Microscope (POM) with crossed polarizers the samples appeared as a sequence of alternating dark (non-birefringent) and bright straight lines, perpendicular to the planar anchoring direction x (Fig. 3.1). The transmitted light intensity showed a sinusoidal modulation along x due to a periodic variation of the refractive index. Such modulation diffracted the light of a green laser beam under normal incidence (Fig. 3.1, Inset).

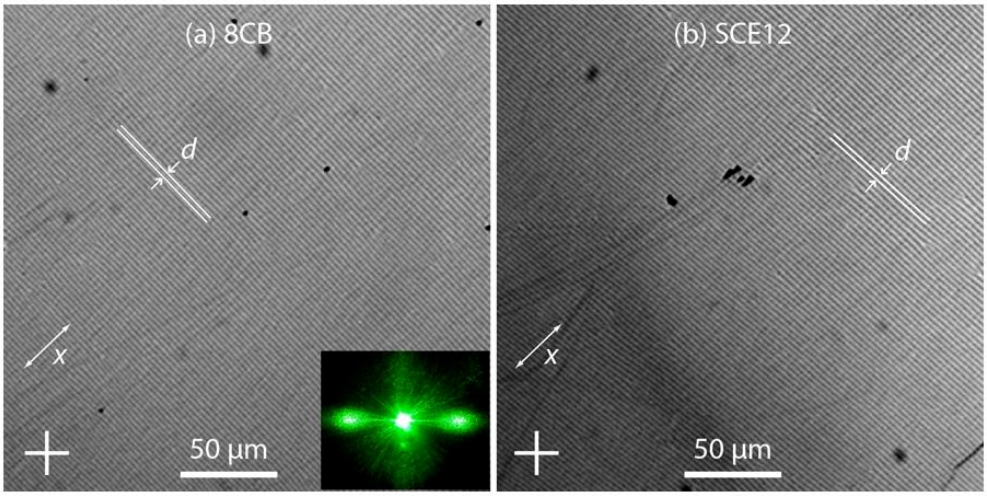

Figure 3.1: POM images of large-area, self-assembled arrays of LDs obtained in the absence of electric field. The planar anchoring direction was parallel to *x* and the polarizers were oriented as shown by the cross. (a) 8CB sample with thickness $h = 1.2$ µm and period $d = 2.6$ µm. Inset: Diffraction pattern for green laser light. (b) SCE12 sample with $h = 1.2$ µm and period $d = 2.7$ µm.

When the sample thickness *h* increased above 1.3 µm, LD arrays coexisted with isolated FCDs and patches of FCD lattice, which developed into a full close-packed 2D lattice as the thickness was increased above 2 µm (Fig. 3.2).

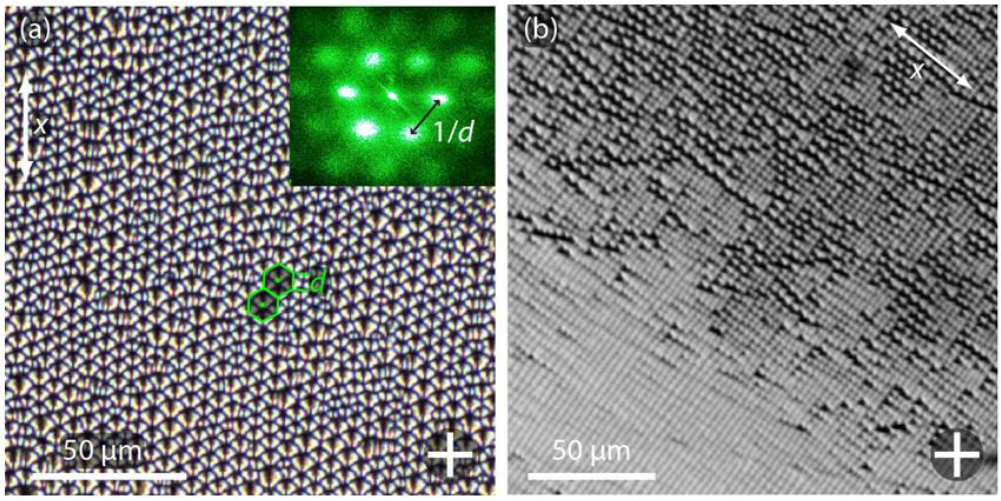

Figure 3.2: (a) POM image of a close-packed lattice of non-toroidal FCDs obtained in the absence of electric field. The planar anchoring was parallel to *x* and the polarizers were oriented as shown by the cross. The sample thickness was $h = 2.7$ µm and then period $d = 4.6$ µm. Inset: Diffraction pattern at normal incidence for green laser light, showing hexagonal symmetry. (b) Region of coexistence at the transition between FCDs and LDs ($h = 1.2 – 1.8$ µm).

Laser diffraction showed that the lattice was hexagonal (Fig. 3.2, Inset). For both LD arrays and FCD lattices, the period d increased almost linearly when h increased, $d = d_0 + V_0 h$, with different slopes V_0 and offset d_0 for LDs and FCDs (Fig. 3.3). Notice that the slope was $V_0 = 2$ for LDs formed in both 8CB and SCE12, indicating that a similar array structure was created for the two compounds, despite their different chemical structure. At the transition between the two pattern types, the lateral size of isolated FCD and the period of FCD patches were comparable to the period in LD regions.

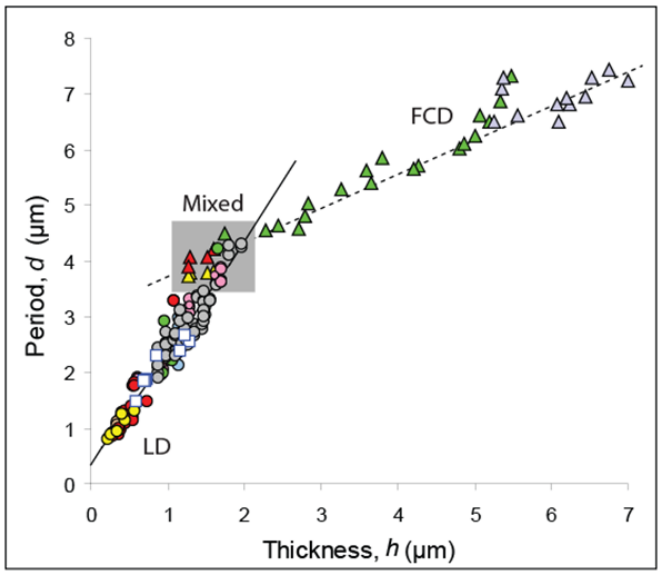

Figure 3.3: Lateral domain size (period) d as a function of the film thickness h. Circles and triangles indicate respectively LDs and FCDs for 8CB samples. White squares in the foreground correspond to LDs formed in SCE12. Solid and dotted lines are linear fits, $d = d_0 + V_0 h$, with $d_0 = 0.3$ µm and $V_0 = 2$ for LDs, and $d_0 = 3.1$ µm and $V_0 = 0.62$ for FCDs. Each color corresponds to a different sample.

In cells with uniform thickness h, the period d of LD arrays was constant. Uniform arrays covering areas as large as 0.1 mm^2 (more than 0.3 mm lateral size) could be routinely obtained. Also, LDs running across the entire uniform area without interruptions or changes in brightness were frequently observed (Fig. 3.1). For a given h, the lateral domain size d (i.e. the local array period) varied slightly among the different domains and from sample to sample. The dispersion was $\delta d / d < 0.2$ for LD arrays and increased for FCD lattices. Such dispersion is much larger than the experimental errors on d, and appears to be intrinsic to the mechanisms of defect nucleation, self-assembly and close-packing that lead to pattern formation.

Simple POM observations of 8CB samples provided a coarse-grained picture of the director field inside the striped LD arrays presented in Fig. 3.4 (a).

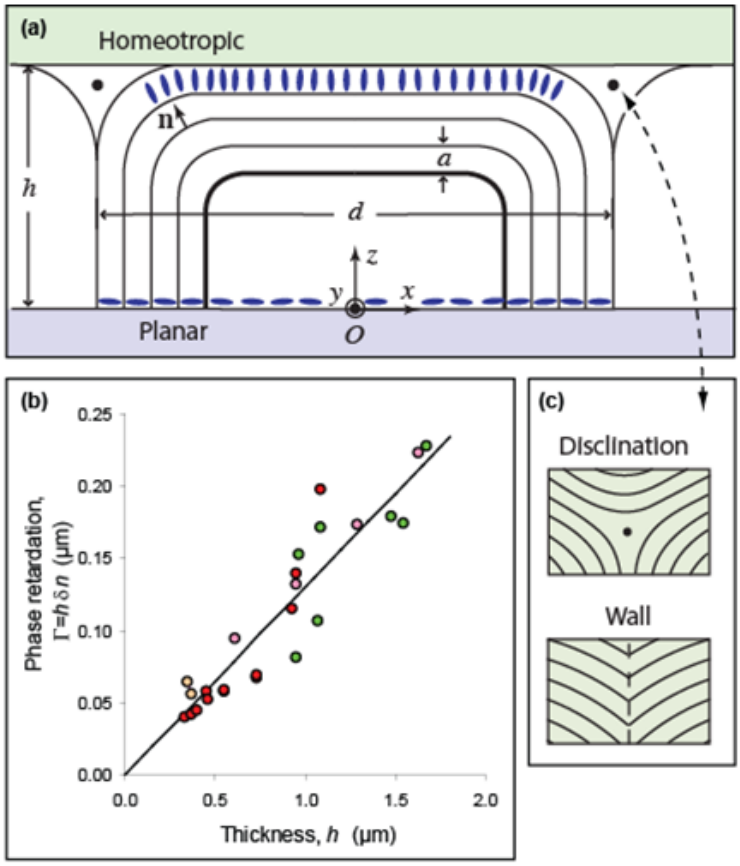

Figure 3.4: (a) Cross-sectional view of the internal LD structure in the absence of a field. Molecules are shown as blue rods, lamellae as lines. **n** is the director, perpendicular to the lamellae, and *a* is the lamella thickness. Lamellae are added confocally to the lamella shown as a thick line. (b) Phase retardation Γ of the brightest regions ($x = \pm d/2$) as a function of the sample thickness *h*. Different colors correspond to different samples. The solid line corresponds to $\Gamma = h\delta n$ with birefringence $\delta n = 0.13$. (c) Disclination lines and curvature walls are expected at the boundary between neighboring domains and at the domain center *O* (black dots).

The director **n** lied in a vertical plane parallel to *x*, was invariant along the perpendicular direction *y* and was periodically tilted from the surface normal *z* towards the direction *x*. Because of the tilt modulation, the laser diffraction was barely detectable when the light polarization was parallel to *y*, i.e. perpendicular to **n** and insensitive to the tilt modulation. Non birefringent dark lines of the LD array corresponded to homeotropic regions where **n** was almost normal to the surfaces (zero tilt) across the film thickness, whereas bright lines corresponded to maximum tilt. In the bright lines, the optical phase

retardation $\Gamma = h\delta n$ increased linearly with the sample thickness h, with local birefringence $\delta n = 0.13$ close to the maximum value $\delta n_0 = 0.165$ for 8CB at room temperature[151] (Fig. 3.4 (b)). This showed that **n** was planar (90° tilt) across most of the film thickness. Such coarse grained picture of the director field and lamellae arrangement in the LD arrays is similar to that obtained by POM for open 8CB films deposited on crystalline surfaces (Fig I.4 (a)) and further detailed by high-resolution X-ray diffraction measurements[39,74,75,201]. These studies have shown that LDs contain lamellae that satisfy both anchoring conditions by starting and ending with a vertical orientation (**n** planar) on the planar anchoring surface, and passing through a horizontal orientation (**n** homeotropic) in between (see thick lamella in Fig. 3.4 (a)). The lamellae are shaped as hemicylinders flattened along the confinement direction z. Building on these ideas, we propose a simple explanation for the slope $V_0 = 2$ of the d vs. h curve of LD arrays (Fig. 3.3). When h increases, LDs grow confocally by propagating the flattened hemicylinder shape: adding one lamella on top increases the domain height h by a and the lateral size d by $2a$ (Fig. 3.4 (a)). However, if the domain has height h above the rubbed polymer substrate at the domain center ($x = 0$, Fig. 3.4(a)), there should be $n = h/a$ lamellae inside it, spanning a distance $d = 2na = 2h$ along x. The presence of an offset such that $d = d_0 + 2h > 2h$ indicates that not all lamellae inside the LDs are built confocally, but there are non-confocal regions inside and surrounding the confocal domain. The latter regions are typically located in the proximity of topological defects. In our samples we expect a defect, most likely a disclination line, at the domain center where the confocal construction leaves the lamellae orientation undefined (point O with $x = 0$ and $z = 0$ in Fig. 3.4 (a)). At the domain boundary, the lamellae close to the homeotropic surface must be flat to conform to the boundary plate and suddenly bend by 90° to reach the polymer surface with a vertical orientation (point with $x = \pm d/2$ and $z = h$ in Fig. 3.4 (a)). Most likely, these lamellae locally violate the homeotropic anchoring and reach the domain boundary with a tilted orientation, thereby creating a curvature wall or a disclination line (Fig. 3.4 (c)).

It is more difficult to determine the lamellae arrangement inside the FCDs due to 3D nature of the FCD implying many parameters to describe eccentricity, orientation, completeness, etc. By analogy with similar patterns obtained in open films[38] and closed cells[70,202] we deduce that the FCDs (Fig. 3.2 (a)) were non-toroidal (eccentric), with the major axis of the ellipse oriented along the anchoring direction x and the conjugated

hyperbola lying in the vertical plane parallel to *x* (Fig. 1.13 (d)). Fluorescent confocal polarizing microscopy (FCPM) studying (Chapter 2.5.3) of 8CB hybrid cells with $h > 2.5$ μm doped with the dichroic laser dye Coumarin 6 (Chapter 2.2.1) have confirmed our assumption (Fig. 3.5). Horizontal FCPM sections, taken with the polarizer *P* parallel (Fig. 3.5 (a)) and perpendicular (Fig. 3.5 (b)) to the planar anchoring direction *x*, show a 2D quasi-hexagonal FCD lattice, similar to the one observed in open cells (Fig. 2.14)[38]. Figures 3.5 (a-c) show that one of the asymptotes of the hyperbola *H*, namely the one pointing towards the OTS surface, is almost vertical so that the conjugated ellipse *E* appears as a circle when viewed along the surface normal, *z*. The hyperbola *H,* lies in the vertical xz plane and passes at the focus *F* of *E* with an inclination of approximately 45° (Fig. 3.5 (c)). When $P \perp x$ (Fig. 3.5 (b, d)) the image plane intersects the ellipse *E* and the FCDs have characteristic double-lobed mustache-like shape. Vertical sections taken on *yz* planes perpendicular to the plane of the hyperbola, do not intersect *H* when the plane is on the opposite side of *F* with respect to the ellipse center *O* (Fig. 3.5 (d_1-d_2)) and intersect *H* at a point (crosses in Fig. 3.5 (d_3-d_5)), that approached the PI surface as the vertical plane moves towards the edge of the FCD, when the *yz* plane is on the same side of *O* as *F*. These results are very similar to those obtained in open 8CB films deposited on PI and mica substrates[38].

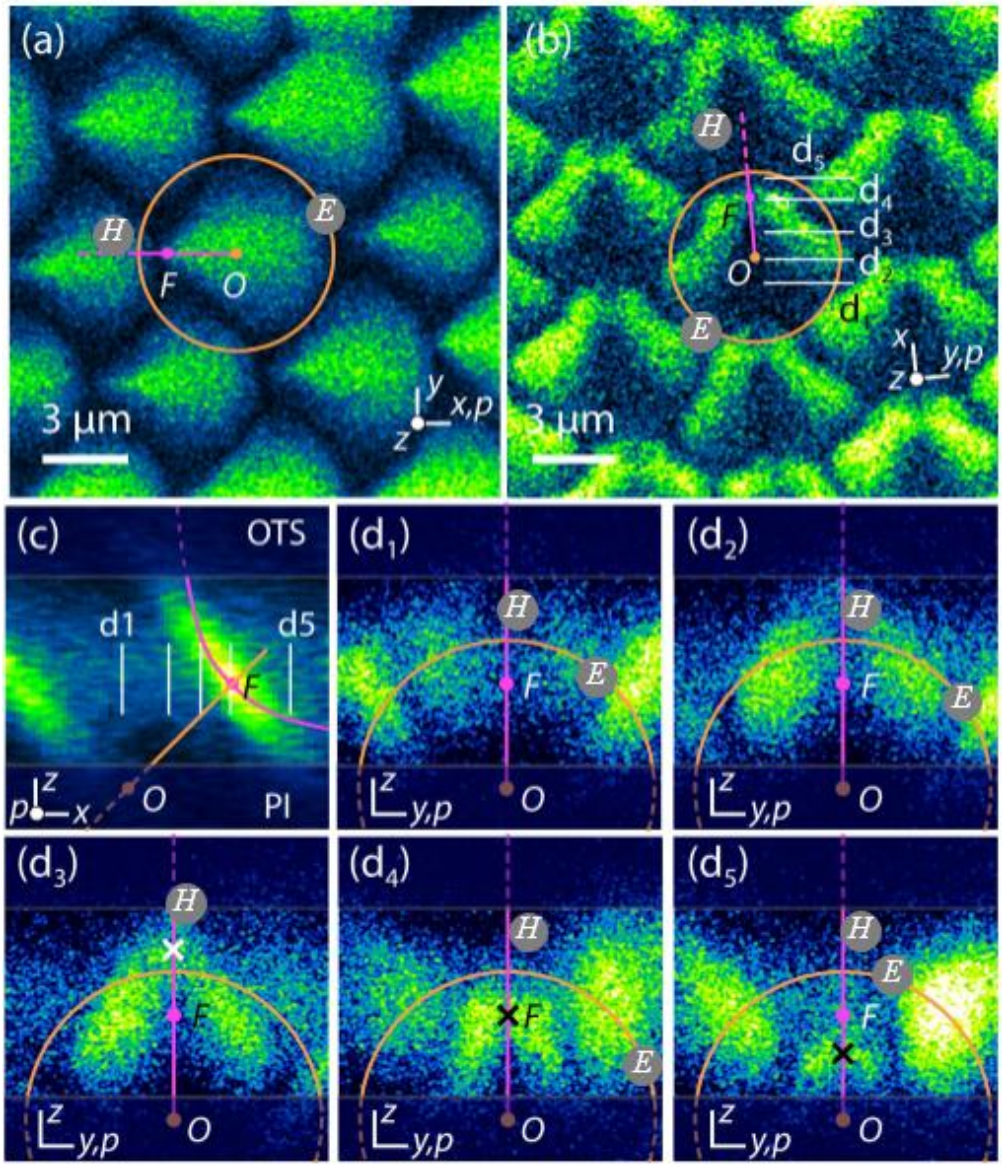

Figure 3.5: FCPM images of 2D arrays of FCDs obtained in the absence of a field. *P*, *x* and *z* are respectively the direction of linear polarization, planar anchoring direction and surface normal. The ellipse *E* with center *O* and focus *F* is tilted by 45° from the surfaces. The conjugated hyperbola *H* lies in the vertical plane *xz*. **(a-b)** Horizontal sections. **(c)** Vertical section in the plane of *H* showing the 45° inclination of *H* around *F*. **(d_1-d_5)** Vertical sections in planes orthogonal to the plane of *h*. The location of the planes in the array is shown in Fig. (b) and (c). Crosses indicate the intersection of *H* with the *yz* planes. The asymptotes of *H* point approximately along *x* and *z*, so that *E* appears as a circle when viewed along these axes (Fig. (a, b and d)).

3.2. Field-on patterns. 8CB

We prepared 8CB samples with thickness h = (6 – 13) µm that produced 2D lattices of FCDs in the absence of a field. When a DC voltage V was applied while keeping the sample in the SmA phase, the overall pattern morphology remained

unaffected. However, when samples were cooled down from the isotropic (Iso) phase while applying the same voltage *V*, 1D arrays of LDs could be created at the Nem – SmA transition if *V* was sufficiently high (Fig. 3.6).

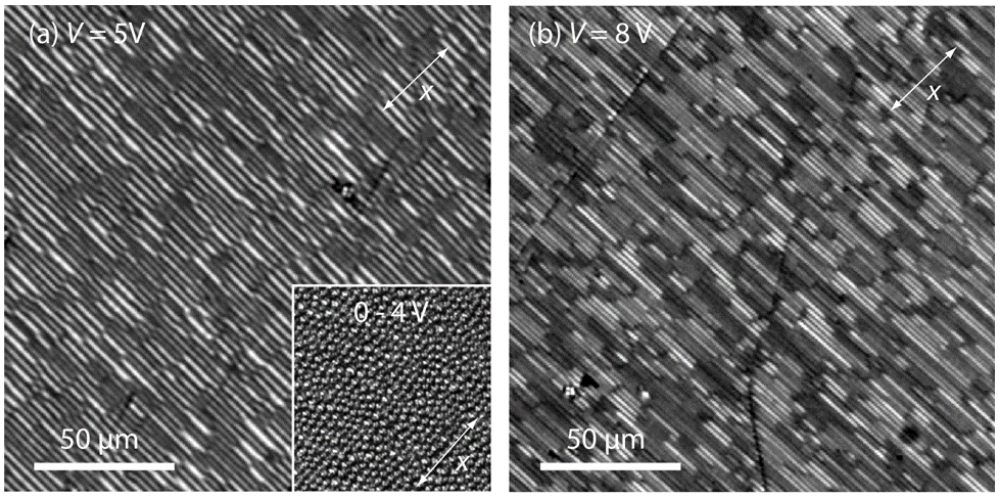

Figure 3.6: LDs created by applying an electric field in an 8CB sample while cooling from the Nem to the SmA phase. (a) Film thickness h = 7.1 µm, voltage V = 5 V. The inset shows the FCD lattice formed in the same region after cooling from Nem phase with a lower voltage. (b) h = 8.1 µm, voltage V = 8 V

.

The size d of the LDs increased approximately linearly with the film thickness h and decreased with V (Fig. 3.7 (a)). For $V > 10$ V, the period of the LDs was too small to be resolved by POM but the white light coming from the microscope lamp was diffracted along the x direction with a green-blue tint, indicative of a LD arrays with small period d. The slope of the d vs. h line decreased as V increased and was smaller than the value V_0 = 2 measured for LDs in the absence of a field. When V was decreased below about 5 V, FCDs appeared first in thick regions of the SmA sample, then in regions with decreasing thickness as V was further decreased. As for the E = 0 case (Fig. 3.3), LDs coexisted with FCDs in the transition region.

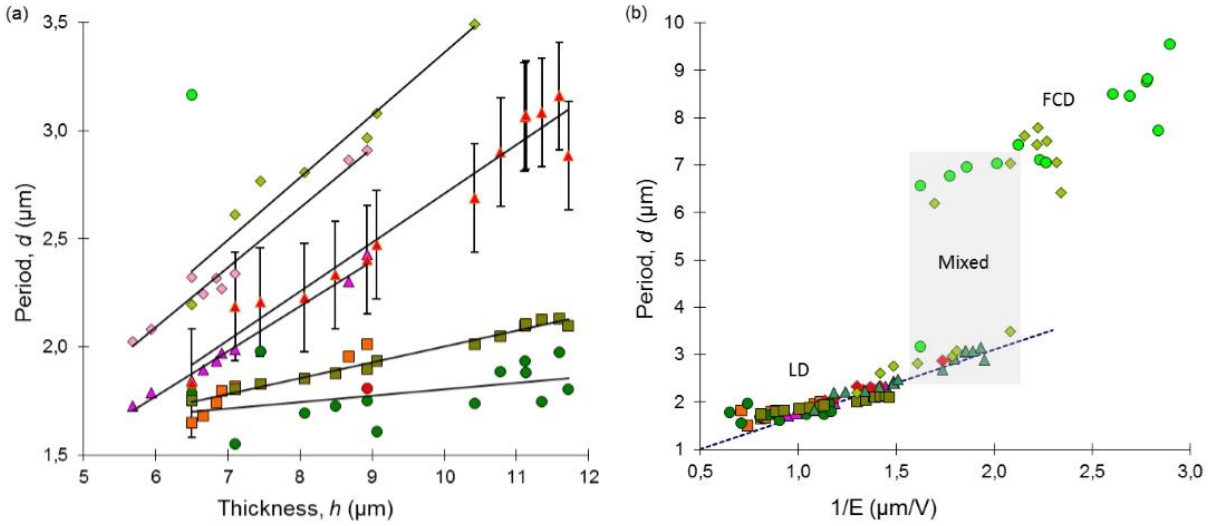

Figure 3.7: (a) Lateral size *d* of LDs as a function of the film thickness *h* for different values of DC voltage *V*. One symbol was used for each voltage. For a given voltage, different colors correspond to different samples. For each *V*, the point with maximum *d* is the latest stable point before the complete transition to a FCD lattice. The error bar shows the typical dispersion of the *d* measurements. (b) Size *d* as a function of the inverse of the electric field $E = V/h$. In the shaded region, LDs coexist with FCDs. The straight dotted line has equation $d = d_0 + V_0 / E$ with $d_0 = 0.3$ µm and $V_0 = 1.4$.

This seemingly complex response to changes of thickness and voltage was much simplified by considering *d* as function of the inverse of the electric field $1/E = h/V$ (Fig. 3.7 (b)). All *d(h,V)* curves reduced to a linear master curve, to $d = d_0 + V_0 /E$, with slope $V_0 = 1.4$ V and offset $d_0 = 0.3$ µm. Moreover, it became apparent that LDs and FCDs coexisted when $1/E$ was between 1.6 V µm^{-1}and 2.3 V µm^{-1}, and the transition from 2D to 1D was complete only for $1/E < 1/1.6$ V µm^{-1} corresponding to $E > 0.6$ V µm^{-1} (Fig. 3.7 (b)). A similar behavior was observed when the field was modulated (sinusoidal AC voltage) at frequencies ranging from 0.1 to 100 kHz. The period, *d*, increased linearly with the inverse of the electric field $1/E = h/V$, where $V = V_{RMS}$, with a smaller slope $V_0 = 0.62$ V and offset $d_0 = 0.2$ µm (Fig. 3.8). For a given voltage *V*, the period of the LD arrays was uniform over areas with uniform thickness *h* (i.e. uniform *E*) and we could routinely obtain areas as wide as 0.3 mm showing uniform period *d*. The period dispersion was $\delta d / d < 0.2$, comparable to that obtained for field-off patterns (Fig. 3.1). In contrast to the latter case, the LDs were frequently interrupted and showed variations of brightness along their length. The average length of uninterrupted domains was significantly smaller than the lateral extension of regions with uniform *d* (Fig. 3.6).

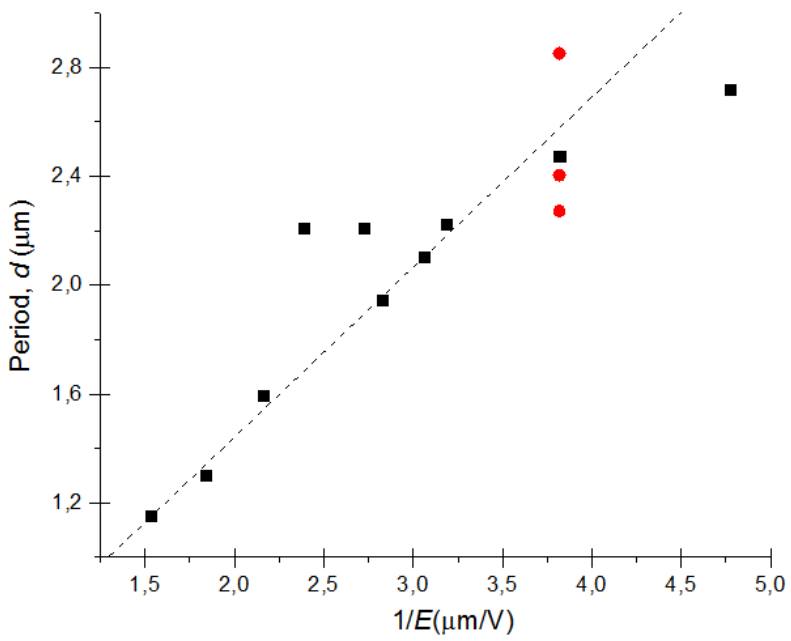

Figure 3.8: Lateral size, d, as a function of the inverse of the electric field $E = V_{RMS}/h$, corresponding to sinusoidal AC fields with variable RMS amplitude and fixed 1 kHz frequency (black rectangles) and variable frequency (0.1 - 100 kHz) with fixed amplitude (red circles). The dashed line is a linear fit of the data described by an equation $d = d_0 + V_0/E$ with $d_0 = 0.2$ µm and $V_0 = 0.62$ V.

To understand the similarities observed in the $E = 0$ case for a varying thickness and in the $E > 0$ case for a varying field strength, we consider the director field **n** in the Nem phase and how it changes in response to variation of E at the SmA-Nem transition (Fig. 3.9).

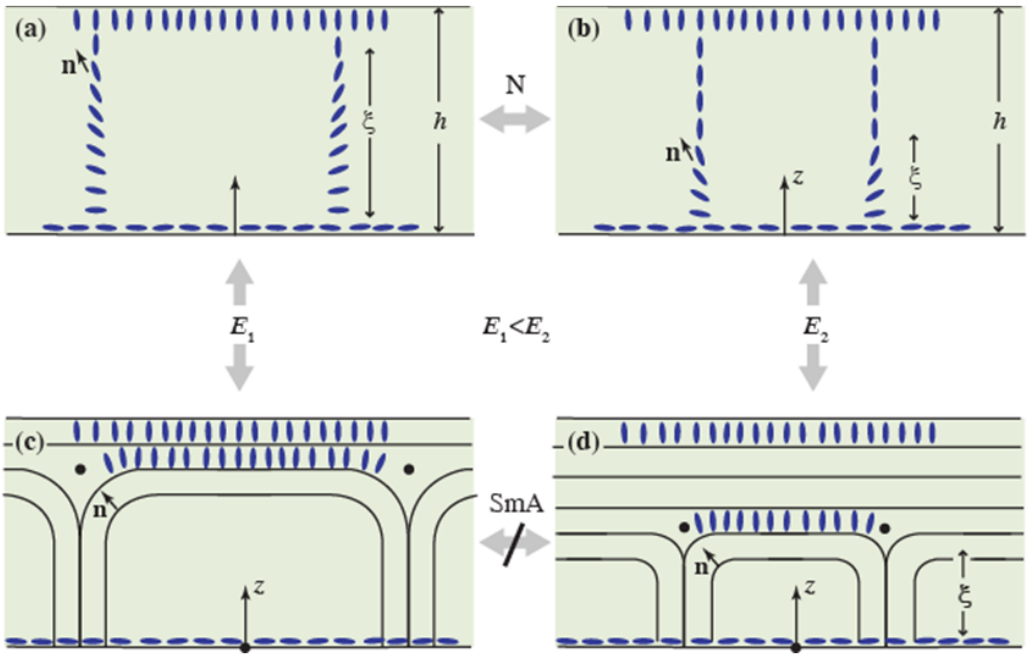

Figure 3.9: Internal structure of a linear domain in the presence of an electric field E. In the Nem phase, the director **n** tilts from the surface normal z in a layer of thickness given by the coherence length $\xi \propto V_0/E$. The height of the LD in the SmA is comparable to ξ. Varying E is not sufficient to change the size of the LDs due to the topological barrier preventing the creation, rearrangement and adsorption of the defects (black dots).

When E tends to zero, the tilt angle varies linearly and uniformly across the entire sample thickness h, rotating from zero to 90° along the surface normal z (Fig. 3.9 (a)). The application of a field introduces a dielectric term - $(\varepsilon_a/2)$ $(\mathbf{n}\cdot\mathbf{E})^2$ in the free energy, where ε_a is the dielectric anisotropy, that couples the director distortion with the external field. When E is increased in the Nem phase, an increasingly thick portion of the LC film close to the surface inducing homeotropic anchoring becomes uniform and homeotropic (i.e., **n**||**E**). The region where **n** significantly tilts from z and E becomes increasingly confined near the surface inducing planar anchoring (Fig. 3.9 (b)). The thickness of this region is given by the electric coherence length $\xi = (K / \varepsilon_0\varepsilon_a)^{1/2} /E$, where K is the elastic constant of the LC and ε_0 the permittivity of vacuum[44]. As the sample is cooled to the SmA phase, the homeotropic region turns into a set of mostly flat horizontal lamellae while curved lamellae are formed in the tilt region (Fig. 3.9 (c-d)). Thus the electric field E has an effect analogous to that of a compression that reduces − from h to ξ − the thickness available for creating curved lamellae.

Our hypothesis is supported by FCPM measurements (Chapter 2.5.3). For FCPM observations we prepared a similar 8CB hybrid cell of thickness h = 13 μm doped with the dichroic laser dye Nile Red (NR) (Chapter 2.2.1. The orthogonal *xz* cross-sections of the sample in the Iso, Nem and SmA phases are shown in Fig. 3.10 as function of an AC voltage (applied through the Nem to SmA transition). The incident light polarization P and thus the detected signal were parallel to the planar anchoring direction x, P || x. The frequency was fixed to 1 kHz.

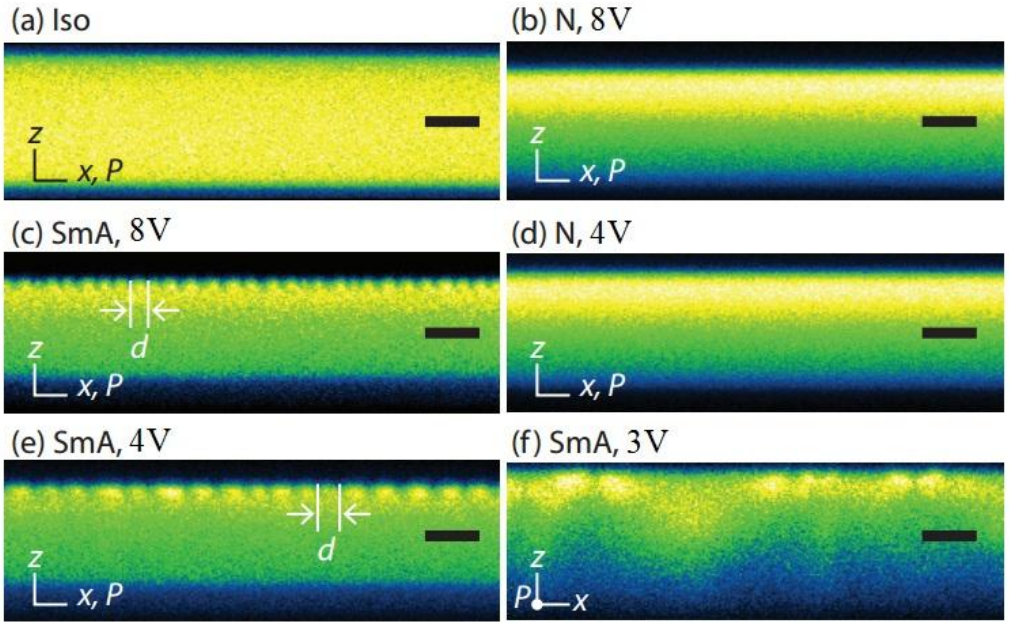

Figure 3.10: FCPM images of *xz* cross-section of 8CB containing fluorescent Nile Red. (a) Iso phase with voltage V_{RMS} = 8 V and 1 kHz sinusoidal AC field applied. (b-c) Nem and SmA phase under the same conditions (d) Heating again in the Nem phase with V_{RMS} = 4 V, (e) SmA phase with V_{RMS} = 4 V. (f) SmA phase with V_{RMS} = 3 V. x and P indicate the direction of planar anchoring and polarization. The sample thickness was h = 13 μm. Scale bar is 4 μm.

In the absence of the electric field the measured fluorescence intensity in the Iso phase was uniformly distributed across the LC film thickness (Fig. 3.10 (a)). This corresponds to the random molecules orientation typical for the Iso phase (Fig. 1.1). When a 1 kHz AC field with voltage V_{RMS} = 8 V was applied in the Nem phase (Fig. 3.10 (b)) the intensity increased as the director tilted from the substrate normal: going from 0° tilt and minimum fluorescence intensity at the homeotropic interface (bottom of the image) to 90° and maximum fluorescence intensity at the planar interface (top of the image). Thus,

it must be noted that fluorescence intensity is not only due to the **n** orientation, but the light adsorption in the LC bulk also may decrease the measured signal. The region where **n** was significantly tilted from the normal was confined close to the surface imposing planar anchoring and produced LD array with a period d = 1.3 μm in the SmA phase (Fig. 3.10 (c)). As an amplitude of the electric field was decreased to 4 V, LDs with a larger period d = 2.1 μm were formed during the Nem – SmA transition (Fig. 3.10 (d-e)). Fig. 3.10 (f) exhibits a more complex director distribution representing an orthogonal cut of FCD lattice which were formed in SmA phase during the transition with a small applied field.

In the N phase we expected a bright region to appear more and more confined close to the planar interface as we were increased the applied voltage above the threshold value of Frederic's transition. One can notice in Fig. 3.10 (b) and (d) quite similar fluorescence intensity distribution in the N phase through the sample thickness under applied 1 kHz AC field 8 V and 4 V respectively. The maximum vertical resolution of the fluorescent microscope, being 500 nm, was not sufficient to resolve and estimate a confinement thickness, ξ, which is expected to be of the same order. Nevertheless, one can see that LD arrays were formed in the tiny region close to the planar interface where we observed the director tilt in the N phase. Accordingly, we can induce a transition from 1D arrays to 2D lattices either by decreasing the thickness with E = 0, or by increasing E.

Following the model of Fig. 3.4 (a) and replacing h with ξ, we expect $d = d_0 + 2\,\xi$. For 8CB, K = 9 pN, ε_a = 9 and $\xi \approx 0.3$ V / E (V μm^{-1}) a few degrees above the Nem-SmA transition[118] (Table 2.1). Notice that $\xi = V_s / \pi E$ where $V_s = \pi\,(K / \varepsilon_0\varepsilon_a)^{1/2}$ is the Frederick's transition threshold voltage (Chapter 1.6). Therefore we expected $d = d_0 + V_0 / E$ where $V_0 / E = 2\,\xi$ with $V_0 = 0.6\,V$. In the case of AC fields, this was indeed the case. On the other hand, for DC fields we obtained $d = d_0 + 1.4 / E = d_0 + 4.7\,\xi$. In all cases, including field-off, DC field and AC field, the offset was d_0 = 0.2 - 0.3 μm.

In a hybrid (planar-homeotropic) nematic cell subject to DC voltage, flexoelectricity and surface interactions (e.g. accumulation of ionic impurities at the electrodes) may create a polarization field **P** that contributes to the free energy with terms of the **P·E** type[63,203]. These effects can be time-averaged to zero by applying AC fields with frequencies in the kHz range[204]. We obtained different pattern dependence on DC and AC fields (Fig. 3.7 (b) and 3.8), showing that polarization effects in the Nem phase

were significant in establishing the properties of the patterns in the SmA phase. The additional constraints of the SmA phase on the **n** also may play an important role. For instance, for $E > 0$ the topmost layer (reaching the maximum height z) of a flattened hemicylinder does not reach the homeotropic boundary and does not have to conform to the rigid plate geometry. Therefore hemicylinders can be more rounded at the top and defects at the domain boundaries may differ from the $E = 0$ case (Fig, 3.9 (c-d)). These differences are also reflected in the behaviour of the 1D-2D transition. For $E = 0$ (Fig. 3.2 (b) and 3.3), LDs and FCDs of comparable size $d = (3.6 – 4.4)$ μm coexisted in the transition region with $h = (1.3 – 1.9)$ μm. For $E > 0$ (Fig. 3.7 (b)), the domain size increased discontinuously at the transition, the FCD size being almost double the LD size. The size of the LDs and FCDs in the transition region were respectively smaller and larger than the size observed in the absence of a field.

3.3. Field-on patterns. SCE12

When LC has negative dielectric anisotropy, $\varepsilon_a < 0$, as it is the case for SCE12, application of an external electric field in the Nem phase leads to the director reorientation perpendicular to the field. Accordingly, in SCE12 hybrid cell the thickness of the region with **n** oriented parallel to the substrates increased as the field strength is increased. The region where **n** rotates from normal to parallel orientation in respect to the substrates is confined close to the homeotropic anchoring surface. The SmA textures created in 7 μm thick cell in the absence of the field and by sinusoidal 5 kHz AC field application during the Nem → SmA phase transition are shown in Fig. 3.11. Typically for hybrid cells, LDs were formed perpendicular to the rubbing direction (Fig. 3.11 (b)). However, LDs were less straight than in the case of 8CB, where the domains are formed close to the planar anchoring surface. Most likely, the director could deviate more from the planar anchoring orientation x through the thick region of the LC film where the director was turned planar. As the temperature was slightly decreased from 110 °C to 108 °C the LD array was replaced by another texture reminiscent of FCDs growing parallel to the rubbing direction in thick cells without a field (Fig. 3.11 (b-c) respectively). Decreasing the AC field strength while keeping the temperature constant or switching the field off resulted in formation of the SmA pattern shown in the Fig. 3.11 (c).

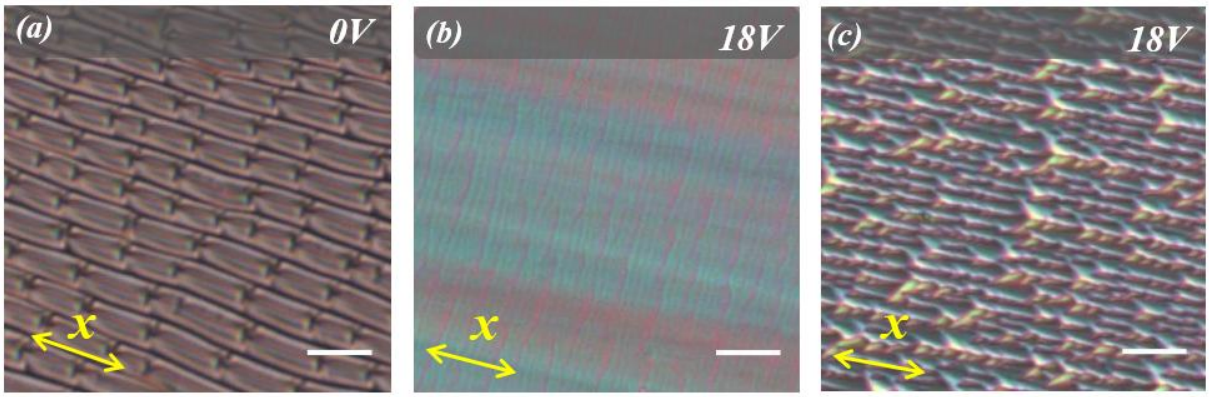

Figure 3.11: POM images showing SmA textures formed in the SCE12 hybrid cell with $\varepsilon_a < 0$ of thickness 7 μm at the Nem → SmA transition (a) in the absence of the field and under applied sinusoidal 5 kHz AC field of (b) 18 V at 110 °C and (c) 18 V at 108 °C. The planar anchoring orientation *x* is indicated by arrows. The scale bar is 20 μm. Images were taken with crossed polarizers.

3.4. Texture persistence and bistability

When the field strength was varied in the 8CB SmA phase after creating a 1D array or 2D, the pattern type did not change and the period remained almost constant for more than one day after varying the field (Fig. 3.12). For both LD arrays and FCD lattices we observed only a small decrease of domain birefringence due to widening of the homeotropic regions and/or decreasing birefringence of the bright regions. In particular, applying a field *E* higher 0.6 V/μm during the Nem-SmA transition created a LD array, but switching from zero to the same value of *E* in the SmA phase created a persistent FCD lattice. Therefore, the system was bistable and the creation of a 1D or 2D texture depended on how the field and temperature were varied.

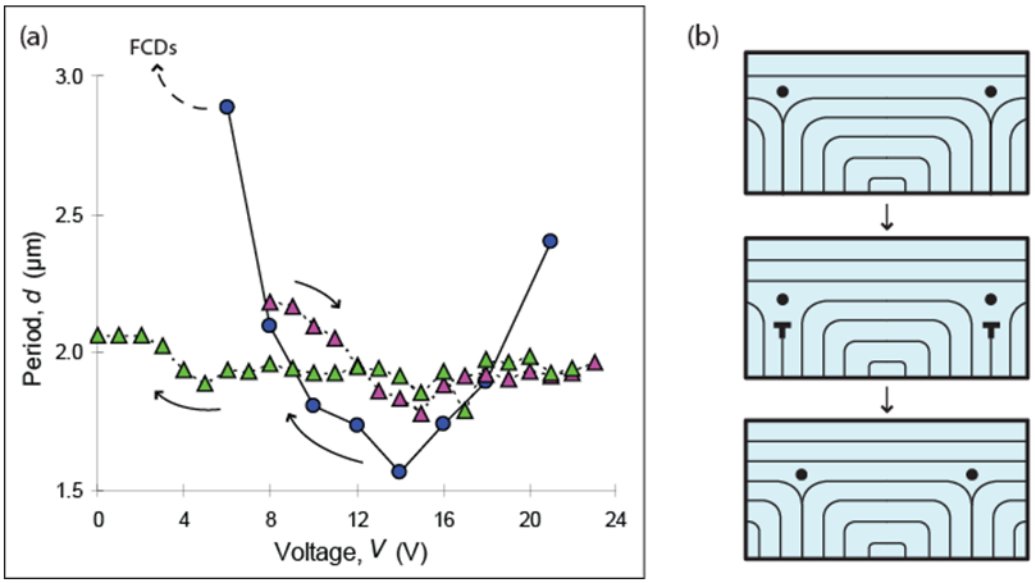

Figure 3.12: (a) Persistence of LD array period d as a function of the voltage V in the SmA phase. Dots correspond to arrays created by applying the voltage while cooling from the Nem to the SmA phase. d varied as a function of V and, for $V < 5$ V, 1D arrays were replaced by 2D lattices. Triangles correspond to an array created by applying a 8 V DC voltage in the Nem phase. After the transition, the voltage was first increased (purple triangles) then decreased (green triangles) while keeping the sample in the SmA phase, without reheating in the Nem phase. In this case, d did not change with V and the 1D-2D transition was not observed. The sample thickness was $h = 11.7$ µm. (b) Reducing the thickness of the region where lamellae are curved requires removing a curved lamella and creating dislocations (t symbols). Dots indicate disclinations lines and curvature walls.

When a FCD lattice was heated to the Nem phase without changing the field, a faint lattice texture was observed by POM in the Nem phase due to surface memory effect, i.e. the persistence in the Nem phase of the **n** field created on the substrates in the SmA phase[38,140]. The print could be erased in the isotropic phase by increasing the field voltage, and LD arrays could be created upon cooling into the SmA phase with $E > 0.6$ µm/V. However, when a LD array was heated to the Nem phase without changing the field, we could not detect the print of the LD texture. Therefore, surface memory effect could stabilize a persistent 2D pattern and hinder the field-induced transition to 1D array, but does not explain the persistence of 1D patterns and their period when the field is decreased or switched off.

The likely cause of the pattern bistability and persistence is that rearranging the lamellae in response to variations of the confinement thickness (h when $E = 0$ or ξ when $E > 0$) involves large energy barriers: the samples remained locked or 'frozen' in a non-

equilibrium state at the Nem-SmA transition, where the constraints of the SmA phase were activated. Indeed, the study of striped patterns and two-dimensional (translation-invariant) periodic materials, particularly liquid crystals[205,206] and cylindrical bloc copolymers[205,207,208], has shown that pattern kinetics is dominated by the large energy barriers required to change the number, type and relative distances of topological defects. Namely, the conservation of the total Burger's vector acts as a global constraint during pattern transformation. Defects also affect the macroscale rheology of SmA LC phases and generate bistability in SmA displays[209]. Fig. 3.12 (b) schematically shows the progressive confinement of a 1D array of LDs due to an increasing electric field. As ξ is reduced, a stack of horizontal layers grows from the surface inducing homeotropic anchoring and curved lamellae must be progressively removed from the flattened hemicylinder. Layer removal involves the creation of dislocations, an energy-costly process that requires violation of the constant-period constraint (confocal rule) around the dislocation core.

Conclusions

Applying electric fields is a simple and effective way to guide the nucleation of defects and their self-assembly in SmA film into periodic micropatterns. Compared to other methods such as microchannel confinement[68] or surface patterning[210], applying electric fields gives the advantage of reconfigurability and bistability that are sought for V_0 applications[73,209,211] and may be beneficial in many applications such as guided assembly of nanoparticles, interacting with defects[76] and fabrication of microlens arrays[73]. Moreover, 1D arrays with periods smaller than 1 μm can be easily created by applying electric fields to thick cells, instead of fabricating sub-micron cells without field. From the fundamental point of view, the smectic order in 1D array has the property of being translation-invariant (along *y*, Fig. 3.4 (a)) and can be studied using the methods developed for two-dimensional periodic systems such as block copolymers[205,207], natural patterns, wavelets and wrinkles[212,213] and smectic phases of superconducting materials[214]. Also, our work with closed cells and electric field evidences the generality – yet to be explained theoretically – of the confinement-induced 2D to 1D transition for a decreasing confinement thickness, previously reported for open films of 8CB on various substrates (molybdenite[39], mica[74] and poly-vinyl alcohol[76]). This phenomenon is largely independent on the confinement type (sample thickness *h* or coherence length ξ), interface chemistry

(8CB or SCE12 at various substrates), boundary rigidity (glass plates vs. air interface), surface anchoring strength, pre-tilt and order (smooth crystalline vs. rough amorphous polymer substrate), as long as the surfaces induce conflicting homeotropic and unidirectional planar anchoring.

4. Planar cells and generality of the 1D/2D transition

In the previous chapter we showed that large-area 1D arrays of LDs or 2D lattices of eccentric FCDs can be formed in SmA films subject to hybrid anchoring conditions. LD arrays were first observed in 8CB droplets deposited on cleaved substrates of crystalline MoS_2 (Fig. I.4 (b))[39] and mica (Fig. I.4 (c))[74]. More recently, LDs were obtained in thin 8CB films spin-coated on PVA (Fig. I.7 (b) Inset)[77] and the structure of the FCD lattices was studied for thick droplets deposited on rubbed PI and mica (Fig. 2.14)[38]. In Chapter 3 we showed that both LD arrays and FCD lattices can be created in closed cell with hybrid anchoring conditions as a function of the film thickness and applied electric field. It was pointed out that the arrays appear at the transition from the Nem to SmA phase, and are stabilized against variations of the applied field by strong topological constraints of the SmA phase.

These observations raise a number of questions: (a) How general are the phenomena of pattern formation and thickness dependence in SmA films? For instance, how similar are the period *vs.* thickness curves, and critical thickness for the 1D/2D transition for various LC compounds and anchoring interfaces? (b) Defects are formed at the transition to the SmA phase from Nem phase, where the director field **n** is distorted in a splay-bend configuration. Is the bend deformation, $\nabla \times \mathbf{n}$, completely expelled from the SmA and is the layer thickness uniform in the LC film? At what point do De Gennes theory and analogy with superconductors (Chapter 1.1.3) become relevant to describe the behavior of the SmA LCs? Namely, the analogy with superconductor suggests that a strong bend can penetrate the SmA phase either in the form of Nem domains for a type-I material, or an array of dislocations for a type-II material. Could the transition from 2D FCD lattices to 1D LD arrays be related to such transition from the Nem phase to the "frustrated" SmA phase with an excess of bend deformation?

4.1. Survey of pattern formation for various liquid crystals and hybrid anchoring conditions

As first towards understanding the nature of the 2D/1D transition we carried out a survey of various SmA LCs confined under hybrid anchoring conditions (without applied electric field). We considered 6 different liquid crystals (8CB, 10CB, 8OCB, SCE12,

CS1024 and 9004 – see Chapter 2.1 and Table 4.1), 4 substrates inducing planar anchoring (MoS_2, mica, PVA, PI) and 2 homeotropic interfaces (air or OTS). The survey included both open films with a deformable air-LC interface and closed cells with rigid boundaries.

Table 4.1:

The phase sequences of studied LC compounds with decreasing temperature

LC	**Phase sequence with decreasing temperature**
8CB	Isotropic ↔ **Nem** ↔ **SmA** ↔ Crystalline
CS1024	Isotropic ↔ **N*** ↔ **SmA** ↔ SmC* ↔ Crystalline
SCE12	Isotropic ↔ **N*** ↔ **SmA** ↔ SmC* ↔ Crystalline
8OCB	Isotropic ↔ **Nem** ↔ **SmA** ↔ Crystalline
9004	Isotropic ↔ **Nem** ↔ **SmA** ↔ SmC* ↔ SmB ↔ Crystalline
10CB	Isotropic ↔ **SmA** ↔ Crystalline

Depending on the LC, different techniques can be used for open film preparation: spontaneous spreading (wetting) of a droplet in the low-viscosity isotropic or nematic phase, or deposition of a droplet (drop-casting) of LC-solvent solution, with or without spin-coating, followed by solvent evaporating. The spontaneous spreading method is applicable to liquid crystals that wet the planar interface. However, it is complicated to obtain droplets with uniform thickness. Non-uniformity results in defect patterns that have a constant period over rather small areas. The drop-casting and spin-coating methods produce more uniform film thickness, but put the solvent in contact with the substrate which may affect the anchoring conditions, especially for rubbed polymer surfaces. Closed cells require a longer fabrication process but offer the advantage that the liquid crystal can be easily filled in the isotropic phase (Chapter 2.4).

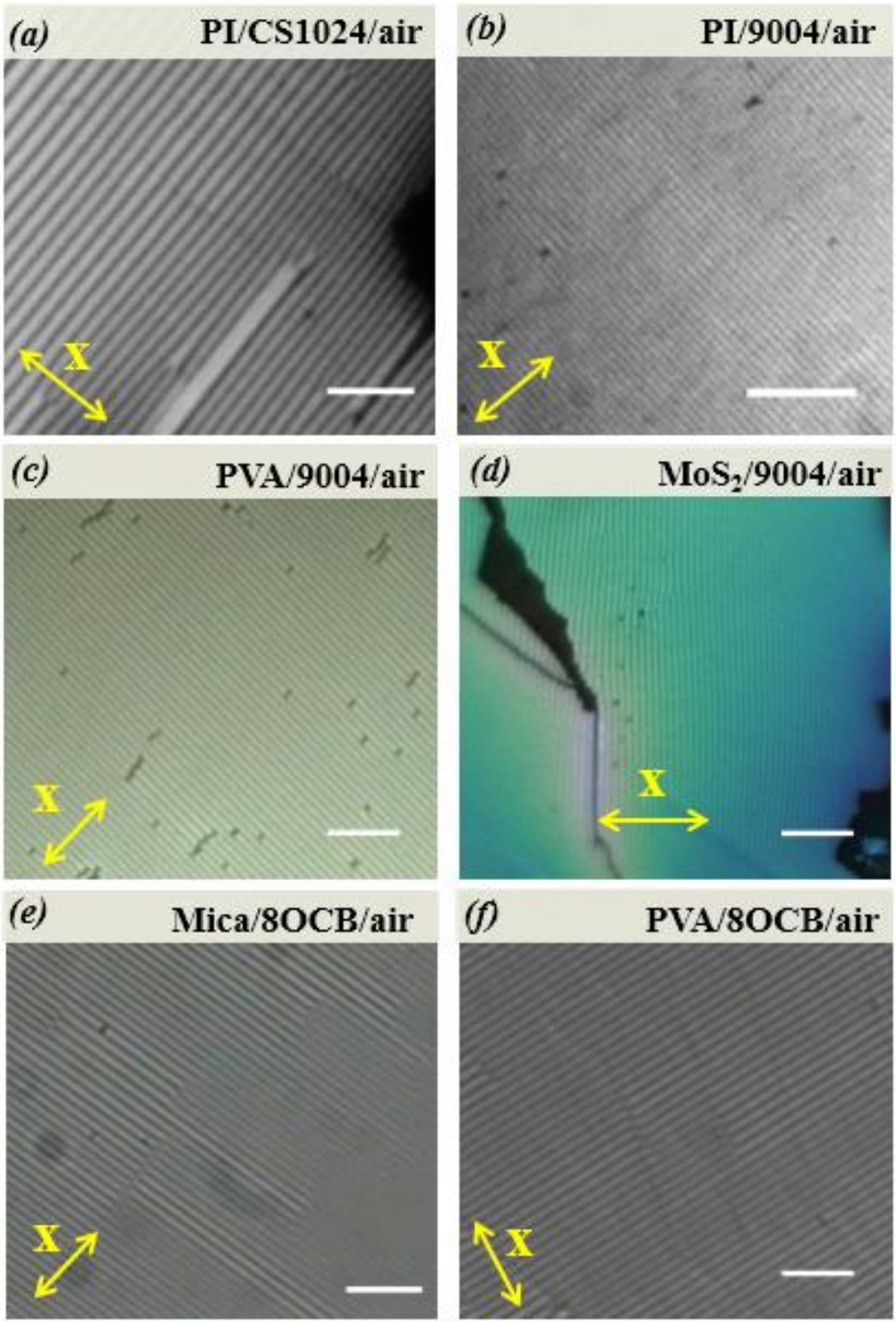

Figure 4.1: SmA textures of various LCs obtained in open cell geometry on different substrates by (a, e-f) wetting and (b-d) spin-coating. Larger LD domains correspond to thicker LC films and are replaced by FCDs after the film thickness exceeds (1-1.5) μm. Arrows indicate the planar anchoring direction *x*. POM images were taken with crossed polarizers. The scalebar on each image is 10 μm.

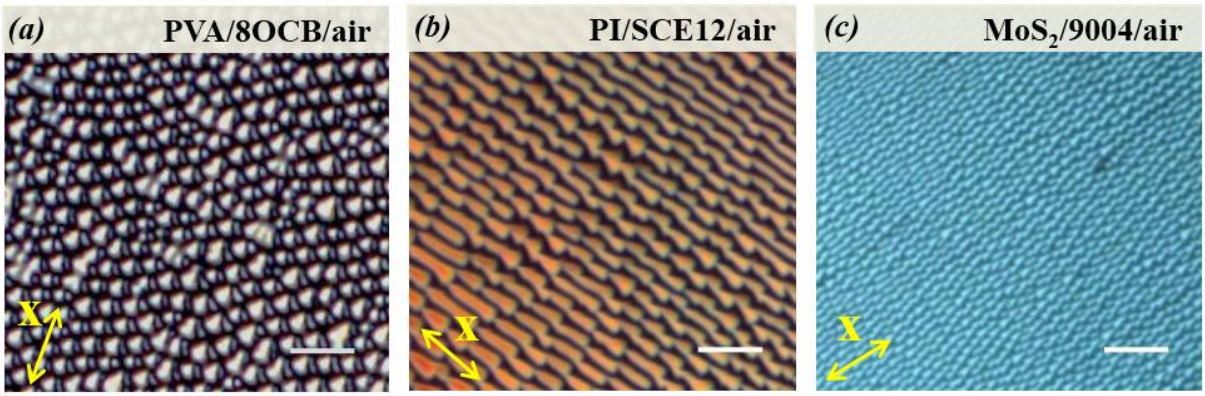

Figure 4.2: FCD textures of various LCs obtained in open cell geometry and film thickness $h > 1.5$ µm on different substrates by (a-b) wetting and (c) spin-coating. Arrows indicate the planar anchoring direction *x*. POM images were taken with crossed polarizers. The scalebar on each image is 10 µm.

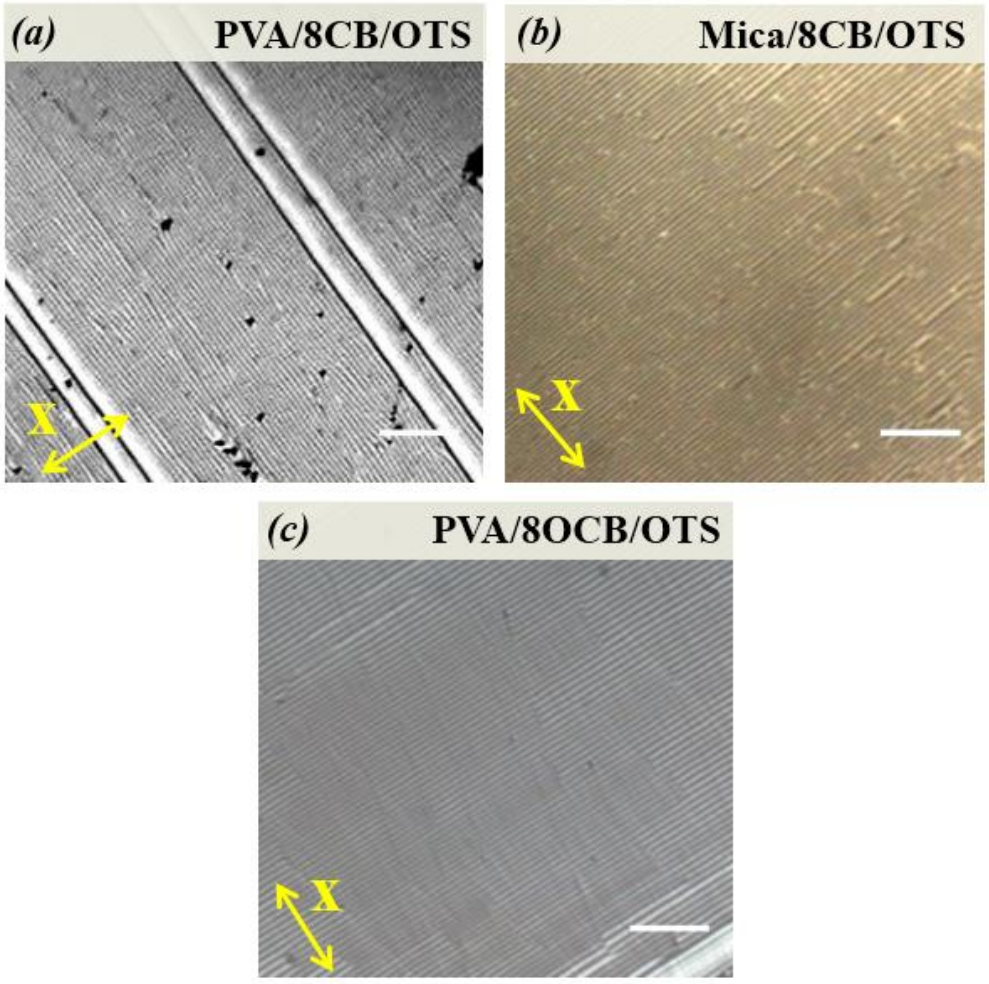

Figure 4.3: LD arrays formed by various LCs confined between rigid boundaries. Rubbed polymer and crystalline substrates were used to induce planar anchoring and silane surfactant (OTS) for homeotropic anchoring. Arrows indicate the planar anchoring direction *x*. POM images were taken with crossed polarizers. The scalebar on each image is 20 µm.

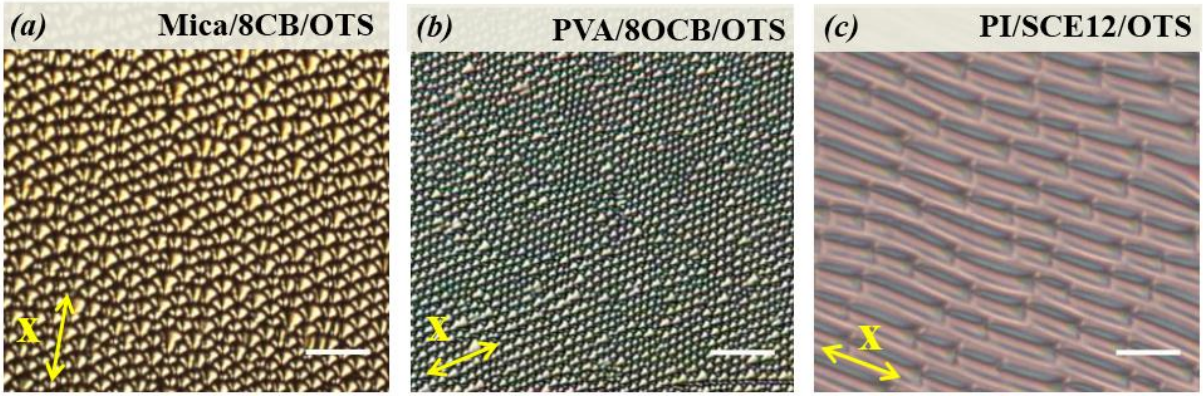

Figure 4.4: FCD textures formed by various LCs confined between rigid boundaries. Rubbed polymers and crystalline substrates were used to induce planar anchoring and silane surfactant (OTS) for homeotropic anchoring. Arrows indicate the planar anchoring direction *x*. POM images were taken with crossed polarizers. The scalebar on each image is 20 μm.

We found that LD arrays and FCDs with various morphology were created in all cases considered, both in open films (Fig. 4.1-2) and closed cells (Fig. 4.3-4), with the remarkable exception of 10CB on polymer substrates (Fig. 4.5). As a general rule, when the LC could be aligned in a uniform texture in the Nem or N* thin films, straight LD arrays invariably appeared at the transition to the SmA. Notice that our survey included LCs with different molecular structure and phase sequence (for instance 8CB and SCE12 in Table 4.1) as well as interfaces with different physical properties (deformable air interface and rigid plates), roughness and degree of order (crystalline mica vs. amorphous polymer surfaces).

The only exception to this rule was 10CB that lacks the Nem phase and shows direct SmA → Iso transition as the temperature is increased (Table 4.1). 10CB films were confined in wedge hybrid cells (PI|10CB|OTS) with thickness (0.5 – 2.5) μm. When cooled down from Iso phase, a uniform non-birefringent texture was observed, with molecules oriented normal to both interfaces. Therefore, the planar anchoring was broken in the SmA phase to the advantage of the homeotropic anchoring. A further decrease of temperature into the crystalline phase led to molecule reorientation with a birefringent texture that persisted when the sample was heated back in the SmA phase (Fig. 4.5). The texture was typical of homogeneous planar cells (see below), suggesting that the homeotropic anchoring was violated. Small-area patches of LDs and FCDs were observed

in this ‘planar’ texture (Fig. 4.5), but the defect morphology was different from that observed for the other systems considered in our survey. Such alignment behavior as function of the temperature was reproduced in repeated cooling/heating cycles. These observations suggest that the presence of the Nem or N* phase at high temperature is important to create defect patterns at the transition to the SmA phase.

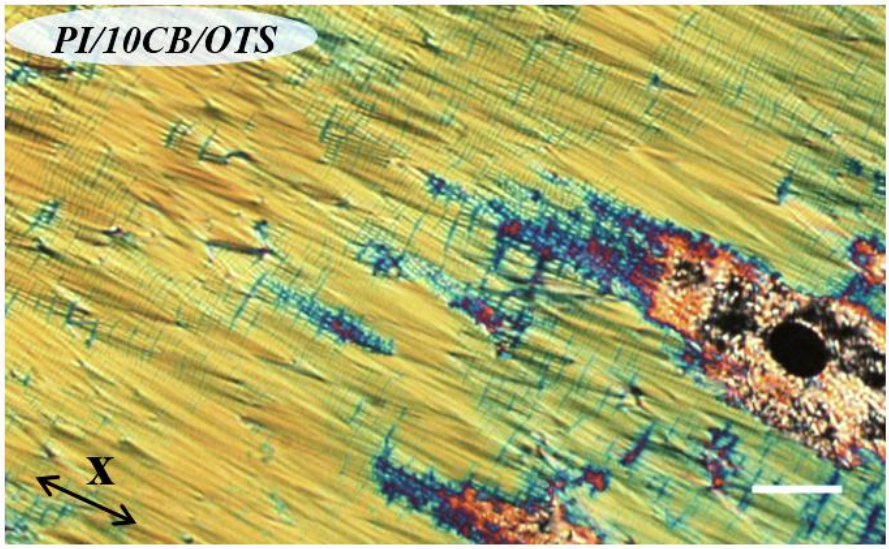

Figure 4.5: POM image of the SmA textures in a 10CB cells with hybrid anchoring conditions. Arrow indicates the planar anchoring direction *x*. The scalebar is 20 μm.

4.2. Period *vs.* thickness curves

Figure 4.6 (a) shows the period *d* as a function of the film thickness *h* of LD arrays formed for various combinations of SmA LCs and interfaces, including open films and closed cells. For closed cells, *h* was measured using an interferometry method in transmission before injecting the LC (i.e. *h* was measured in air) whereas *h* was measured in reflection for open films deposited on a highly reflective Si wafers (Chapter 2.5.1). The thickness measurement was done assuming that the phase of light waves traversing the LC film was proportional to the *h* and zero phase shift upon reflection at the interfaces. In fact, the reflection phase shift may be different from zero and depend on the combination of LC and interface considered (e.g. 8CB/PI or 8CB/PVA), thickness of the polymer coating and presence of ITO electrodes. Therefore, the slope of the *d*(*h*) is accurate but *h* may differ by a small offset between different cases.

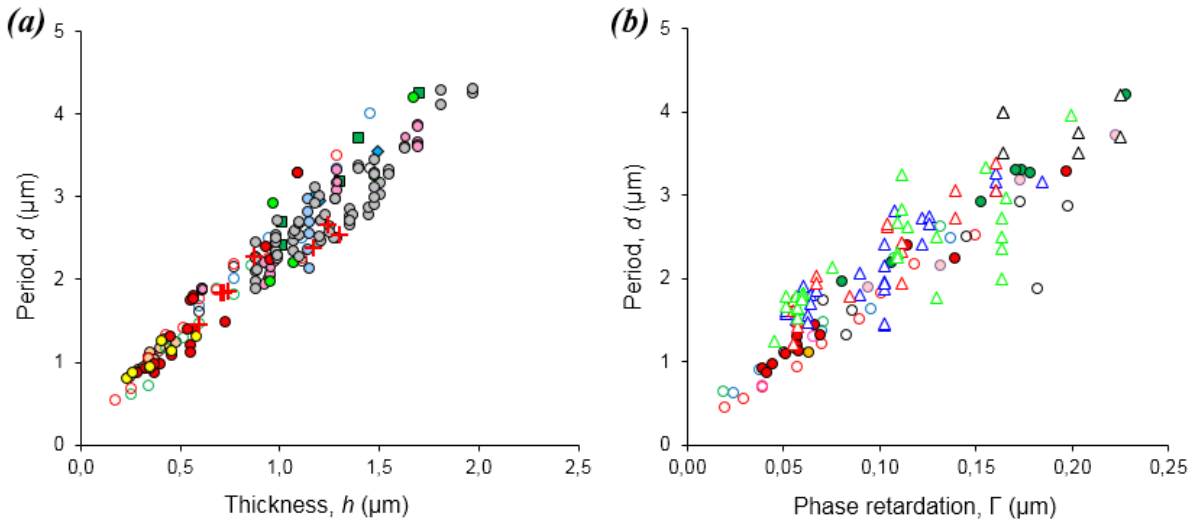

Figure 4.6: (a) Period *d* as a function of the film thickness *h* of LD arrays formed for various combinations of SmA LC and interfaces, including open films and closed cells. (b) Period *d* as a function of the phase retardation Γ measured in the region of the LD array with maximum birefringence. For values of *h* or Γ larger than those shown in the figures, LD arrays were replaced by FCDs. Empty symbols are used for open cells (air interface) and filled symbols – for closed cells (OTS-coated interface): triangles correspond to 8CB on mica, circles are 8CB on PI, squares are 8CB on PVA, crosses are SCE12 on PI and diamonds are 8OCB on PVA. Different colors correspond to different samples.

Figure 4.6 (b) shows the period *d* as a function of the difference in phase retardation $\Gamma = h\delta n$ between ordinary and extraordinary waves measured in regions of the LD array with maximum birefringence δn. This figure includes previously published data on mica|8CB|air films for which a direct measurement of *h* could not be obtained[74]. The comparison reveals strong similarities among LD arrays obtained in various cases:

(a) Both open films and closed cells show a dependence of the type: $d \approx d_0 + 2h$ where $d_0 \approx 0.2$ μm for open cells and $d_0 \approx 0.3$ μm for closed cells.

(b) The period *d* grows up to a maximum value of about 4.0 - 4.5 μm before the LD arrays are replaced by FCDs.

(c) The slope $\partial d/\partial \Gamma$ is close to 15.3 for PI|8CB|air, PI|8CB|OTS and mica|8CB|air. In the first two cases, the dependence of *d* on *h* is known and we can deduce the birefringence from the relation $\partial d/\partial \Gamma = \delta n \cdot \partial d/\partial h$. Namely, $\delta n = 0.13$ that is close to the maximum value for 8CB, $\delta n = 0.165$. Although *h* could not be directly

measured for mica|8CB|air samples, the $\partial d/\partial\Gamma$ slope and maximum period were comparable to those measured for other samples.

Also the stability of LD arrays appeared to depend on the film thickness and temperature. In thin films, LDs formed at the transition remained relatively stable in the Nem phase. In thick films, the LDs were stable close to the transition but tended to merge with neighboring domains and form wider LD as the temperature was decreased. The change was slow and progressive, as if transformation into large LDs required overcoming some sort of constraint or barrier. Very often, the merging produced a new type of linear domains showing a transverse modulation, striated stripes (Fig. 4.7).

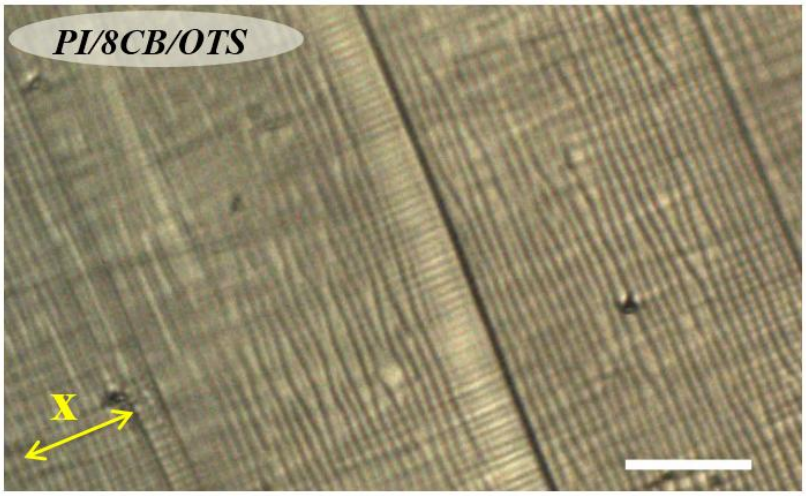

Figure 4.7: POM image of a LD array interrupted by striated stripes formed in PI|8CB|OTS cell. Arrow indicates the planar anchoring direction *x*. The scalebar is 20 µm.

These observations clearly indicate that LD arrays have a common structure when observed at the optical length scale of a few microns and undergo a 1D/2D pattern transition when the thickness exceeds a common critical value. Their behavior seems to be independent on the degree of order that is imposed by the surfaces (i.e.: highly ordered crystalline surfaces *vs* rubbed polymers) or the deformability of the interface (i.e.: soft air *vs* hard OTS interface). It also seems to be independent on the LC properties.

4.3. Field effects in cells with homogeneous planar anchoring conditions

In Chapter 3 we showed that LD arrays can be created when the SmA film is confined to a small thickness under the effect of an external electric field. The key to understand pattern formation was to consider the director deformation in the Nem phase, where splay-bend distortions are confined in a thin surface layer with thickness comparable to the electric coherence length $\xi \propto 1/E$. In this section we further investigate the generality of 1D pattern formation by extending the idea of electric-field induced confinement to LC cells with homogenous planar anchoring conditions.

The LC was sandwiched between two ITO coated glass plates separated by mylar spacers with thickness h = (3.6 – 100) μm, placed on a heating plate and observed through POM with crossed polarizers. We considered homogenous planar anchoring conditions where the easy axes were twisted by 90° ('twisted cell' in Fig. 4.8 (a)) or parallel to each other ('parallel cell' in Fig. 4.8 (b)). In the latter case, we did not see any difference whether the rubbing directions were parallel or antiparallel.

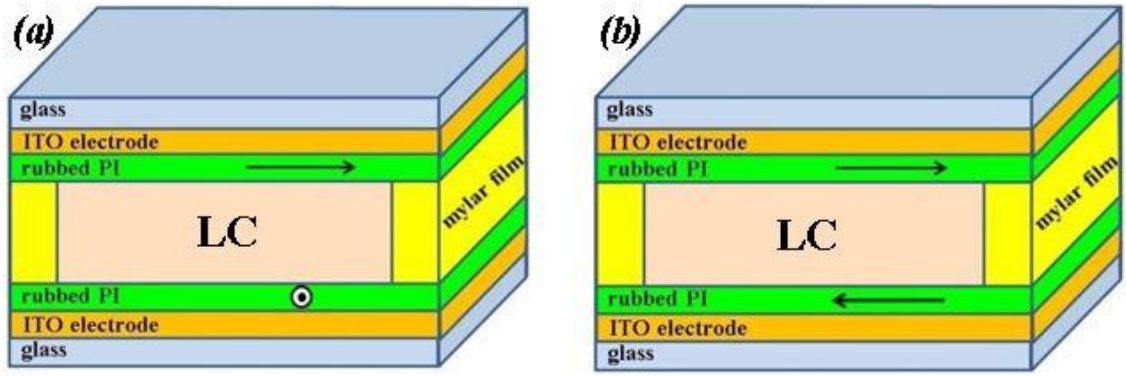

Figure 4.8: Cells with homogeneous planar anchoring conditions. (a) 'Twisted' cell with rubbing directions twisted by 90°. (b) 'Parallel' cell with parallel or antiparallel rubbing directions.

The initial "field-off" texture was relatively free of defects for twisted cells (Fig. 4.9 (a)), whereas it showed elongated FCDs in parallel cells (Fig. 4.6 (b-d)), with a very eccentric ellipse (viewed edge-on in the figures) and hyperbola lying in the surface plane. Eccentric FCDs with this type of orientation are rather common in planar cells. We

considered a range of thickness h = (3.6 – 100) μm. The size of the ellipse decreased as the thickness h decreased while the eccentricity decreased. In sample thinner than about 10 μm, the two branches of the hyperbola were almost parallel to each other and formed an array of lines with various width running along the planar anchoring direction. This type of texture can be seen also in the SmA phase of 10CB confined under hybrid anchoring after heating from the crystal phase (Fig. 4.5).

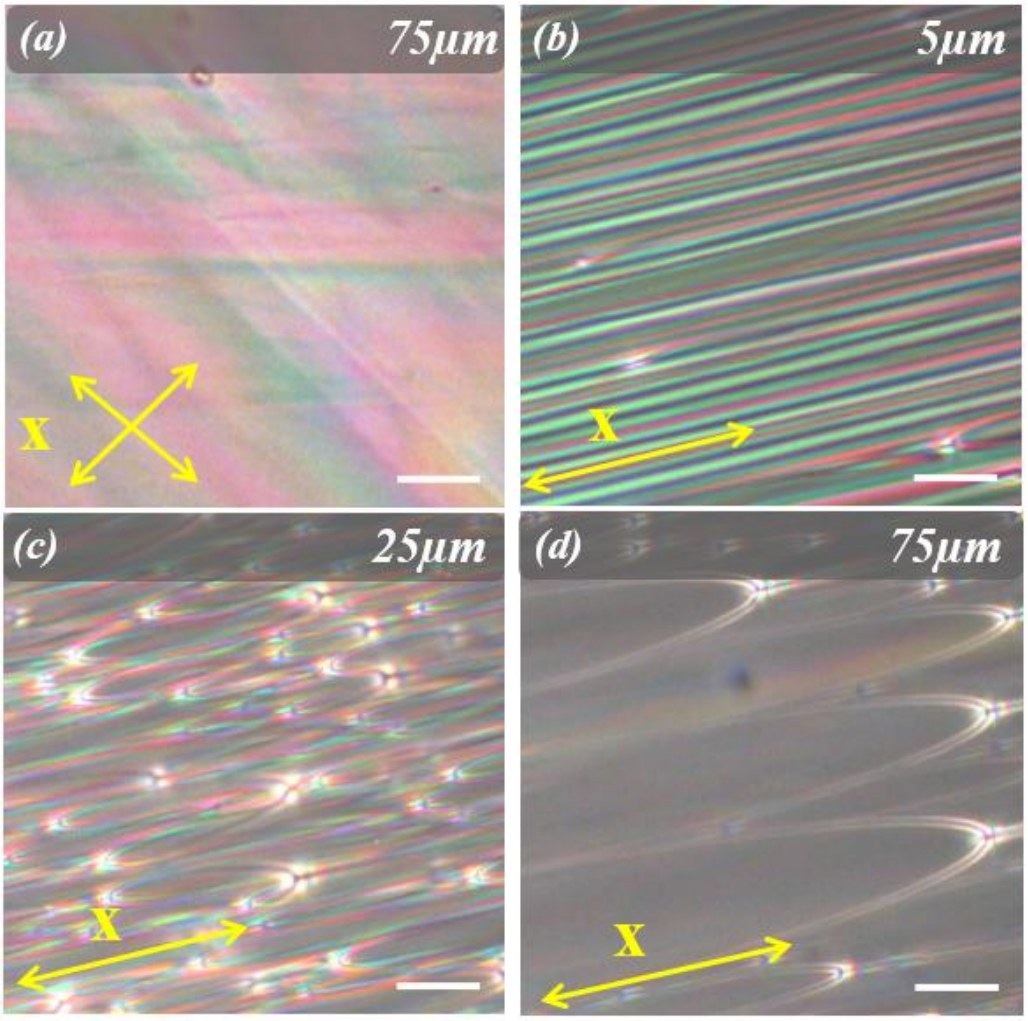

Figure 4.9: POM micrographs of cells with homogeneous anchoring conditions in the absence of a field. (a) Twisted cell. (b-d) Planar cells showing elongated FCDs along the rubbing direction indicated by arrows. The scalebar is 20 μm.

When an AC field was applied in the Nem phase and through the Nem → SmA transition in cells with homogeneous planar anchoring conditions, a LD array was created near each electrode (Fig. 4.10). As already noted for hybrid cells (Chapter 3), LDs grew

perpendicular to the rubbing direction. In twisted cells, two distinct LD patterns were formed at the electrodes, perpendicular to the local planar anchoring direction and therefore to each other.

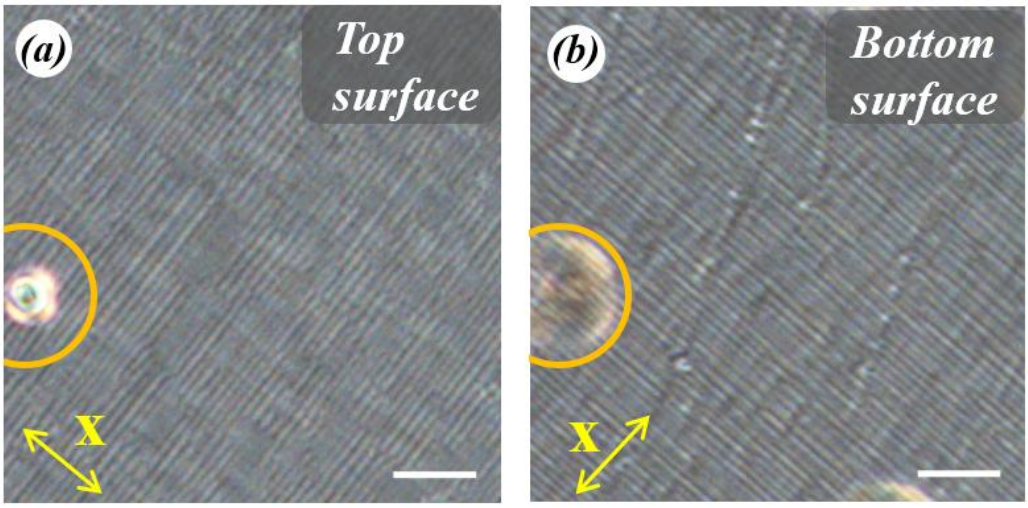

Figure 4.10: POM micrographs showing LD arrays formed at the Nem → SmA transition in a cell with twisted planar anchoring conditions. Arrays are formed near each surface, perpendicular to the local anchoring direction *x*, indicated by arrow, and therefore with each other. The two images were taken at the same position by placing the focus at different depth into the sample. The FCD in the image of the top surface appears defocused in the image of the bottom surface. The AC field was sinusoidal with frequency 5 kHz and RMS voltage 25V. The scalebar is 20 μm.

In the case of parallel cells the top and bottom LD patterns were aligned and superposed, making the optical observation more difficult. Figure 4.11 and 4.12 show FCPM analysis of the LD arrays. We notice in Fig. 4.12 that the arrays are formed in the SmA phase very close to the planar anchoring surface in a layer with thickness of the order of 1 μm, much smaller than the cell thickness *h*.

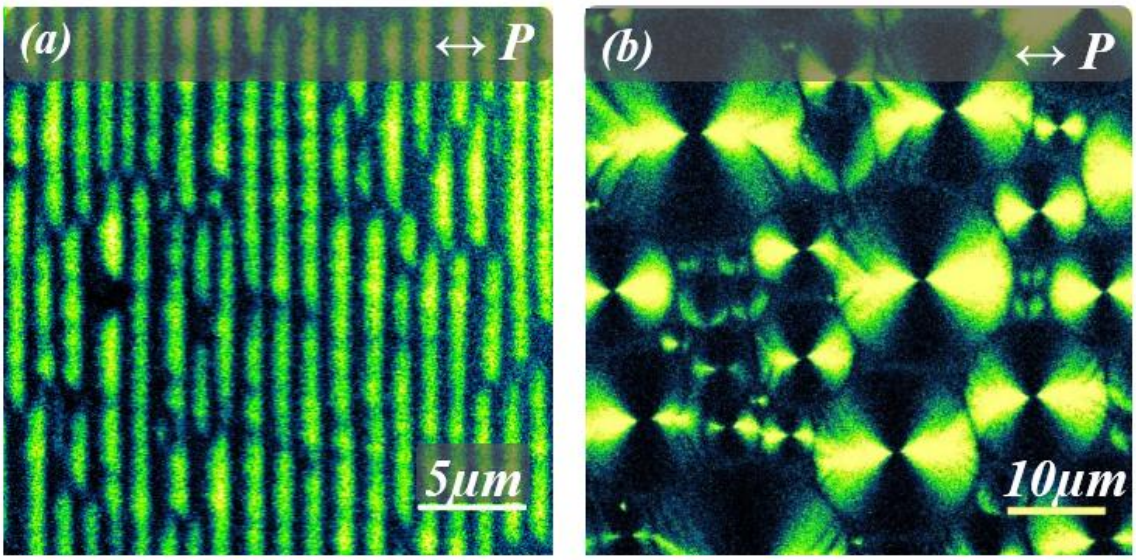

Figure 4.11: (a) FCPM images of LD array obtained by applying a 1 kHz AC voltage with V_{RMS} = 25 V to homogeneous planar cell with thickness h = 92 μm containing a mixtures of 8CB and anisotropic fluorescent dye Nile Red (0.3 mM). (c) FCD texture obtained after turning the field off.

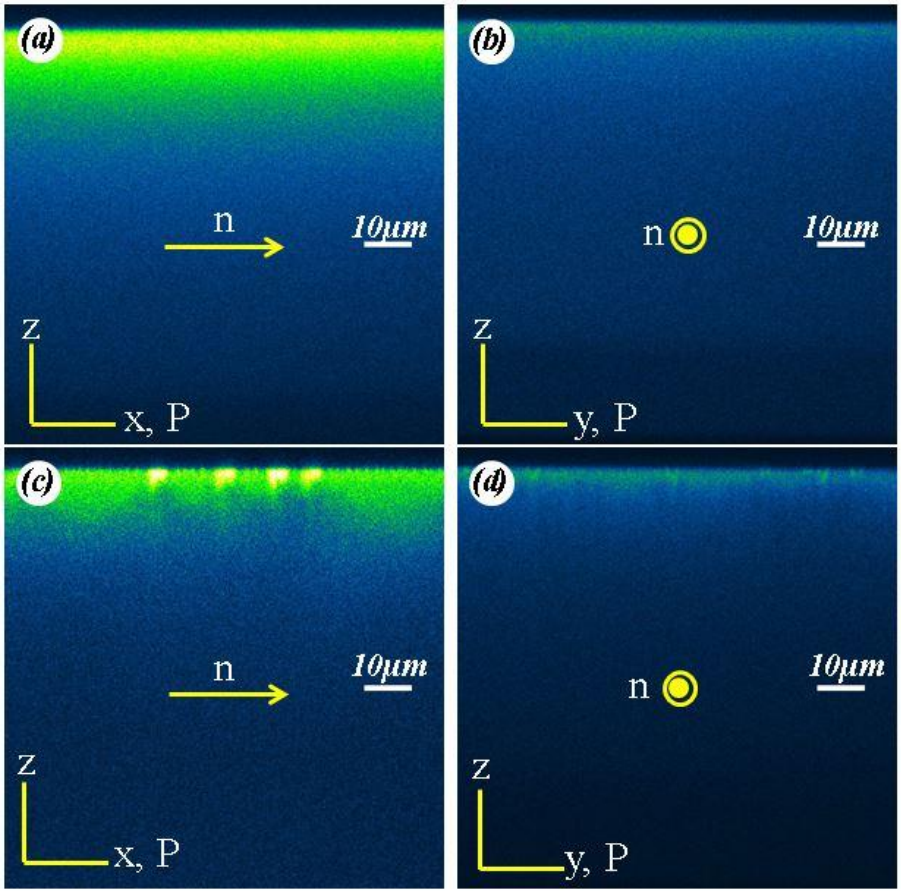

Figure 4.12: (a) FCPM images of LD array obtained by applying a 1 kHz AC voltage with V_{RMS} = 25 V to homogeneous planar cell with thickness h = 92 μm containing a mixtures of 8CB and anisotropic fluorescent dye Nile Red (0.3 mM). (a) Nem phase with polarizer P parallel to the planar anchoring direction x. (b) Nem phase with P perpendicular to x. (c-d) SmA phase showing the LD in a narrow layer close to the planar anchoring surface.

In both twisted and parallel cells, the array period d decreased with increasing AC voltage (Fig. 4.13) and was proportional to the inverse of the electric field: $d = d_0 + V_0/E$ with d_0 = 0.9 μm and V_0 = 0.34 V (Fig. 4.14 (a)). A dependence of the type $d = d_0 + V_0/E$ is consistent with the analysis of the results obtained for cells with hybrid alignment (Chapter 3). In the presence of a field E in the Nem phase, the director is distorted in a splay-bend configuration in a layer with thickness $\xi \approx (K/\varepsilon_0\varepsilon_a)^{1/2}/E$ near each planar anchoring surface, and LDs are created when ξ is sufficiently thin (Fig. 1.19 and Fig. 3.9).

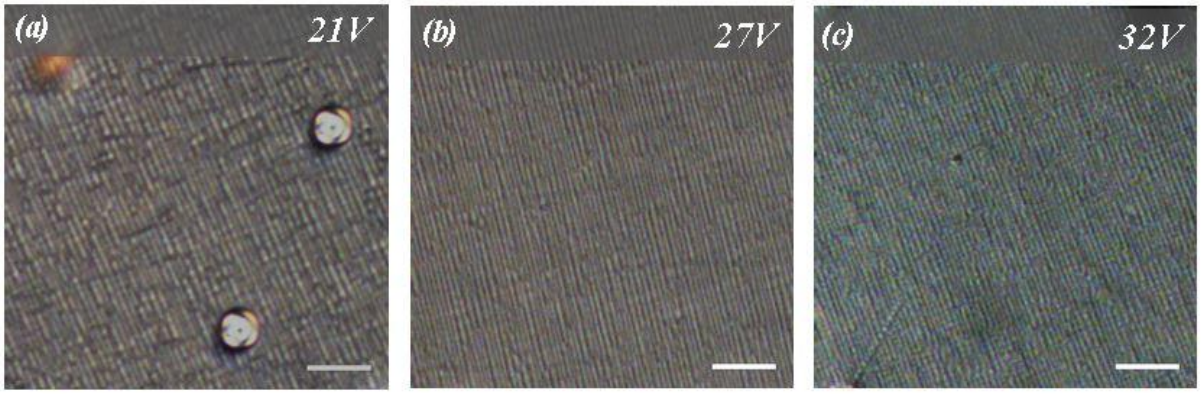

Figure 4.13: POM images of LD arrays formed at the Nem → SmA transition in a cell with homogeneous planar parallel anchoring conditions and thickness h = 75 μm under an applied sinusoidal field with frequency 5 kHz and various RMS voltages. The scalebar is 20 μm.

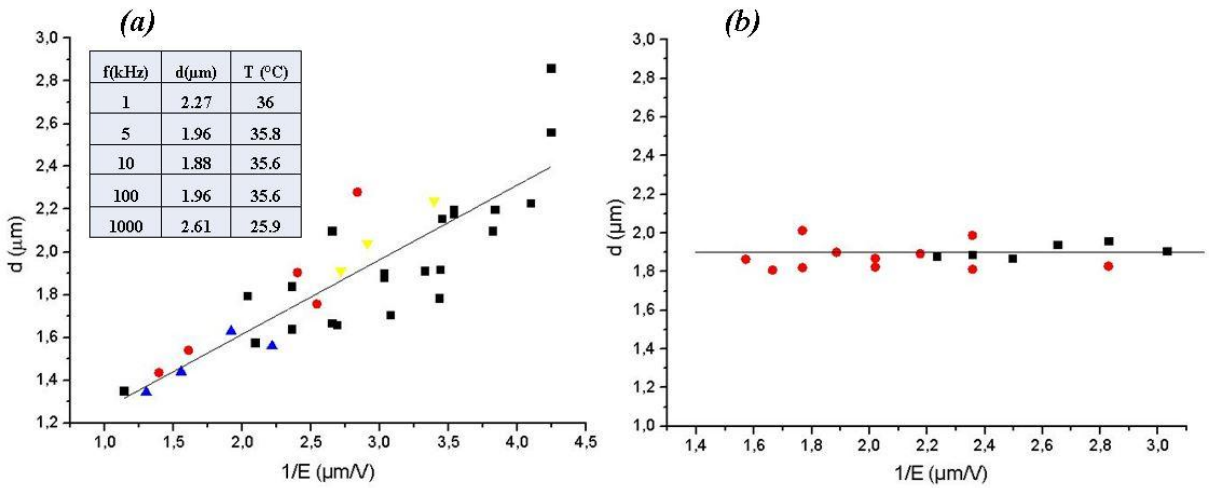

Figure 4.14: Period d as a function of the inverse of the electric field $E = V_{RMS}/h$ for cells with homogeneous planar anchoring conditions. (a) Sinusoidal voltage with frequency f = 5 kHz applied through the Nem → SmA transition. The straight line is a linear fit of the data: $d = d_0 + V_0/E$ with $d_0 = 0.9$ µm and $V_0 = 0.34$ V. The inset shows the dependence of d on f and temperature for a fixed amplitude of 25 V. (b) Field applied in the SmA phase without heating in the Nem phase. Symbols with different colors correspond to different samples.

Notice that V_0 was close to Freedericks' threshold $V_s = \pi (K_{11}/\varepsilon_0\varepsilon_a)^{1/2} < 1$ V of 8CB in the Nem phase. Interestingly, for hybrid cells we obtained $V_0 = 0.62$ V (Fig. 3.8), i.e. the LD period increases twice as fast as in twisted and planar. This difference cannot be simply explained considering the electric field-induced director distortion in the Nem phase. Indeed, for the high voltages $V >> V_s$ required to create LD array in hybrid and parallel/twisted cells, the director distortion is confined to a comparable thickness of the order of ξ, as shown by the calculations presented in Chapter 1 (Fig. 1.19).

When the field variations were performed deep in the SmA phase after creating the LD arrays, d remained constant (Fig. 4.14 (b)), as in hybrid cells (Fig. 3.12)[113]. However, when the voltage was decreased below a certain threshold, an increasingly large area of the LD array was replaced by FCDs until the array was eventually replaced by FCD at zero field (Fig. 4.11 (b)). This is in contrast with the behavior of hybrid cells were the SmA film remained "trapped" in a metastable 1D array pattern even after completely switching the field off. To characterize this behavior we considered wedge cells with homogeneous parallel planar anchoring conditions and thickness in the range (3.6 – 75) µm, and applied a 5 kHz sinusoidal AC field with different RMS voltage V through

the Nem-SmA phase transition. For each applied voltage and temperature, a threshold film thickness was noted above which the FCD covered more than 50% of the sample area. The results show a linear dependence: $V = V_t + E_t h$ (Fig. 4.15). For the three temperatures considered, both V_t and the slope E_t decreased as the temperature increased.

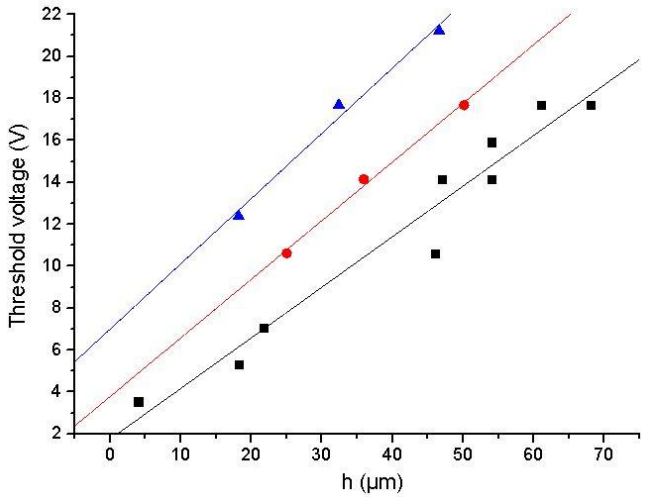

Figure 4.15: Threshold voltage for the LD-FCD transition in the SmA phase as a function of LC film thickness h at a different temperatures. The solid lines are linear fits $V_{RMS} = V_t + hE_t$ with: $V_t = 7$ V, $E_t = 0.31$ V/μm at 32 °C; $V_t = 4$ V, $E_t = 0.28$ V/μm at 33 °C; $V_t = 2$ V, $E_t = 0.24$ V/μm at 34.5 °C. The sine frequency was 5 kHZ.

For all the thickness range considered, h = (3.6 – 100) μm, it was not possible to induce a transition from FCDs to LD arrays or FCD hexagonal lattices when the electric field was applied deep in the SmA phase. Interestingly, the FCD-LD transition could not be applied with a DC voltage (Fig. 4.16).

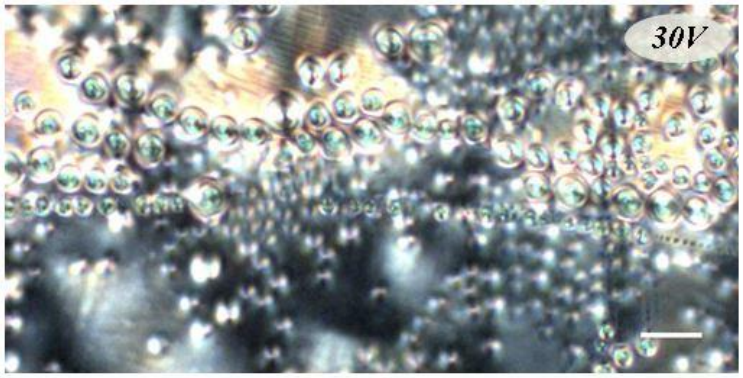

Figure 4.16: POM image showing SmA texture created in a homogeneous planar cell of thickness 75 μm at the Nem → SmA transition under applied DC field of 30 V. The scalebar is 20 μm. Image was taken with crossed polarizers.

The LD size and the temperature where LD appeared also depended on the frequency f of the applied AC voltage (Fig. 4.14 (a), Inset). For 1 – 10 kHz the temperature was almost constant, but the period slightly decreased as the frequency was increased. When the frequency was increased up to 1 MHz, LDs appeared 10 °C below the temperature measured for 1 kHz AC field. The period of LDs also notably increased from 1.9 - 2.0 μm for 10 and 100 kHz to 2.6 μm for 1 MHz (Fig. 4.17). Since the effect of increasing the frequency can be compensated by decreasing the temperature, a possible explanation is that heat was generated in the LC sample at frequencies of the order of 1 MHz.

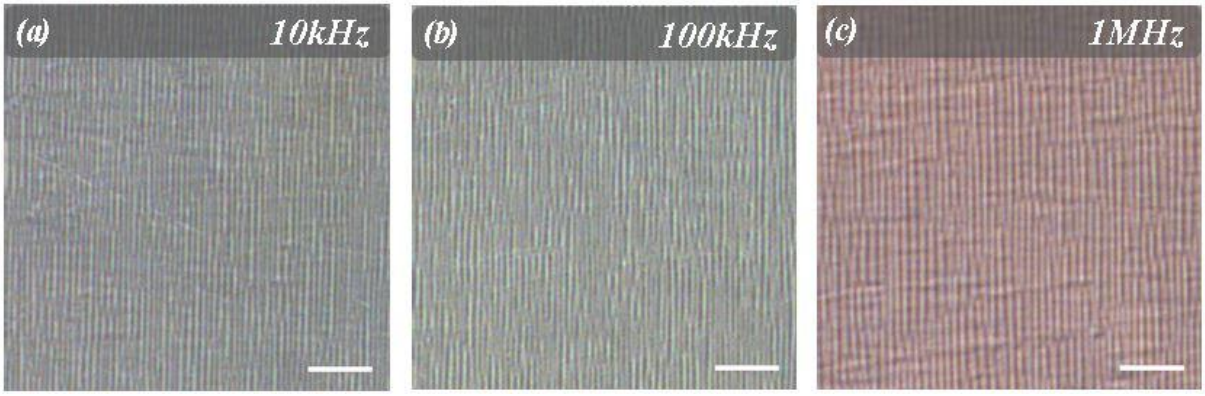

Figure 4.17: POM images showing LD arrays formed at the Nem → SmA transition in 75 μm thick homogeneous planar cell under applied sinusoidal AC field with fixed RMS voltage of 25 V and various frequencies. The scalebar is 20 μm.

4.4. Origin of the 1D/2D transition

In the previous sections we showed that 2D lattices of FCDs and 1D arrays of LDs are formed upon cooling the LC from the Nem to the SmA phase under conditions where the director field **n** is distorted in a splay-bend configuration. The transition between the two pattern types is induced by confining the distortion in a layer with sufficiently small thickness h. In this section we address the nature of this transition.

In Chapter 3 we noted that the 2D lattice is made of close-packed non-toroidal FCDs. The FCD construction satisfy the confocality requirement (Chapter 1.3.4) by

curving the director field in a way that cannot also satisfy a uniform anchoring condition (homeotropic or unidirectional planar) on a flat surface. Therefore, one or both anchoring conditions must be violated in a LC film where a 2D lattice of FCD is formed at the Nem to SmA transition. It has been shown that, for planar anchoring, the surface director deviates from the anchoring direction both in and out of the surface plane (i.e. in the azimuthal and zenital directions)[38]. Clearly, the FCD lattice is formed because breaking the confocality rule ($\nabla\times\mathbf{n}=0$) would cost more free energy than breaking the anchoring.

As the film thickness *h* decreases, deviations from the anchoring directions are expected to become larger as they help balancing the increase of bulk elastic energy created by the increased confinement. This is indeed the behaviour observed for the Nem compound 5CB (lacking the SmA phase) under hybrid anchoring conditions[215]. In contrast, at the transition from the 2D lattice to 1D array, the azimuthal anchoring is *restored* in the LD array. This suggests that the 1D/2D transition has another explanation that may be related to the complex nature of the Nem-SmA transition occurring in the presence of strong director distortions.

In Chapter 1.3.2 we introduced the Landau-De Gennes free energy expansion for the transition from the Nem to SmA phase in the presence of bend ($\nabla\times\mathbf{n}$) and splay ($\nabla\cdot\mathbf{n}$) distortions:

$$f = f_N + a|\psi|^2 + \frac{b}{2}|\psi|^4 + \frac{C_{\parallel}^2}{2}\left|\nabla_{\parallel}\psi - iq_0\mathbf{n}\right|^2 + \frac{C_{\perp}^2}{2}\left|\nabla_{\perp}\psi\right| + \frac{K_{33}}{2}(\nabla\times\mathbf{n})^2 + \frac{K_{11}}{2}(\nabla\cdot\mathbf{n})^2 \qquad (4.1)$$

The bend term $(\mathbf{n}\times\nabla\times\mathbf{n})^2$ (Eq. 1.3) has been simplified considering that $\mathbf{n}\perp(\nabla\times\mathbf{n})$ in a LD array. De Gennes noted the analogy with the transition between normal (*N*) and superconductive (*S*) state of a metal in the presence of an external magnetic field $\mathbf{B}=\nabla\times\mathbf{A}$ [119]. He pointed out that the *N* and *S* states are analogue to the Nem and SmA phase, respectively, and the magnetic field is analogue to the bend field. The transition between the *N* and *S* phase is accompanied by distinctive phenomena that depend on the type of material considered.

In type-I superconductors, the magnetic field is expelled from the SmA phase (Meissner effect) when the field strength is below a temperature-dependent value H_c (Fig. 4.18). By analogy, a type-I LC shows a SmA phase when the bend deformation is below

threshold, while it remains in the Nem phase above the threshold ($|\psi| = 0$). In type-II superconductors, the field enters the material along singular flux lines corresponding to topological defects of the superconducting phase. At the temperature-dependent threshold H_{c2}, the array reaches the maximum density of defects and the metal becomes *N* when the field strength exceeds the threshold. The dense array is known as the Abrikosov lattice[216].

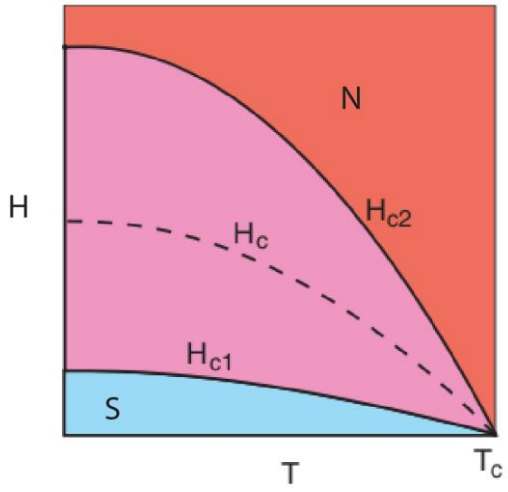

Figure 4.18: Schematic phase diagram of a superconductor showing the transition lines between the normal (*N*) and superconductive (*S*) state as function of the temperature *T* and magnetic field *H*. In an LC, the *N* and *S* phases are analogue to the Nem and SmA phases of a LC, respectively, and $H = |\nabla \times \mathbf{n}|$. In a type-I materials, the H_c line corresponds to the *N*-*S* phase transition. In type-II mater, the *S* and *N* phases are separated by a "vortex" phase (region between H_{c1} and H_{c2} lines) comprising a dense arrays of topological defects.

In this section we explore the possibility that the observed transition from 2D lattices of FCDs to 1D arrays of LDs is a manifestation of the Nem- SmA transition *itself*, under conditions where phenomena analogue to the Meissner effect and Abrikosov lattice formation are expected. We propose that there are *two* transition lines in the *H*-*T* phase diagram of LC compounds showing the 1D/2D transition (Fig. 4.18), in analogy with type-II superconductors. A low-field line H_{c1} marks the transition between the bend-free SmA and a 'mixed' phase where bend distortion is allowed to partially enter the LC material. A high-field line H_{c2} separates the mixed phase from the Nem phase where the SmA order is completely melted. We identify the lattice of FCDs with the bend-free SmA phase as the FCDs result from the confocal construction (bend-free) of a set of (equally spaced) smectic layers. We identify the LD array as the mixed state, although we are not

yet able to directly determine whether it corresponds to an Abrikosov-type lattice or to an "intermediate state" often observed for type-I superconductors[217]. Finally, we identify untextured regions as the Nem phase.

We notice that the transition temperature is expected to be lower or "depressed" in the presence of bend compared to the value T_c without bend (Fig. 4.18). In type-I materials, the bend field is completely expelled at the transition from the SmA to Nem, corresponding to points along the line H_c in Fig. 4.18.

We investigate the dependence of LD arrays on temperature T and thickness h in closed wedge cells with hybrid anchoring conditions (planar on rubbed PI and homeotropic on OTS). These samples were compared to cells with homogeneous anchoring conditions (parallel rubbing direction, Section 4.3) that did not induce bend distortion, for the same values of T and h in the range (0.3 – 3.5) μm. A closed heater with a thick Teflon casing was used to avoid temperature gradients between the bottom interface, closer to the heating element, and the top surface close to the glass window used for POM observations. A controller allowed changing the temperature by 0.1°C steps. Measurements were done 2 hours after changing the temperature to allow sample equilibration.

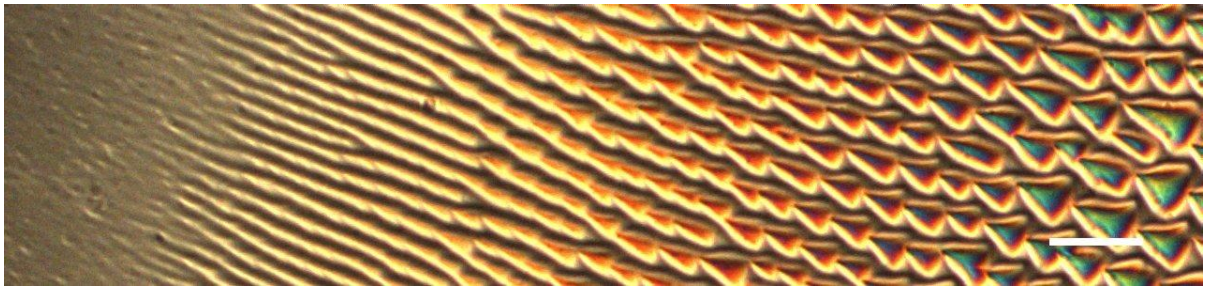

Figure 4.19: POM image showing the FCD appearing in an 8CB wedge cell at 32.1 °C. The scalebar is 20 μm.

As the temperature was decreased from the Nem phase, FCDs were the first to appear in thick part of the sample with $h \geq 1.5$ μm, where the bend distortion was less (Fig. 4.19). The FCDs lattice was observed for $T < (32.1 \pm 0.1)$ °C and disappeared completely above (32.3 ± 0.1) °C, except for the print left on the rubbed polymer surface. For comparison, cells with homogenous planar anchoring conditions showed the transition at (33.80 ± 0.05) °C indicating that the temperature of FCD formation was depressed

compared to the bulk. The FCD lattice grew by first creating a linear patterns with stripes running parallel to the anchoring direction *x* (note that LD are perpendicular to *x*). Since the stripes cannot be extinguished by rotation between the crossed polarizers of a POM, the director did not lie in a vertical plane orthogonal to the polarizers (as observed for LDs). A similar texture was reported by Cladis and Torza who noticed that the stripe size depended on the LC film thickness[200]. As the temperature was decreased, the FCDs grew into initially untextured Nem regions of the sample with smaller thickness, indicating that the material is of type-I and the transition lines H_{c1} and H_{c2} coincide for weak bend deformations. In support of this conclusion, type-I behavior has been reported for 8OCB, which creates 1D arrays similar to 8CB[218] (Fig. 4.6 (a)). This also implies that the LD arrays are similar to the "intermediate state" of type-I superconductors where stripe domains are frequently observed, due to the coexistence of (non-singular) Nem and SmA domains.

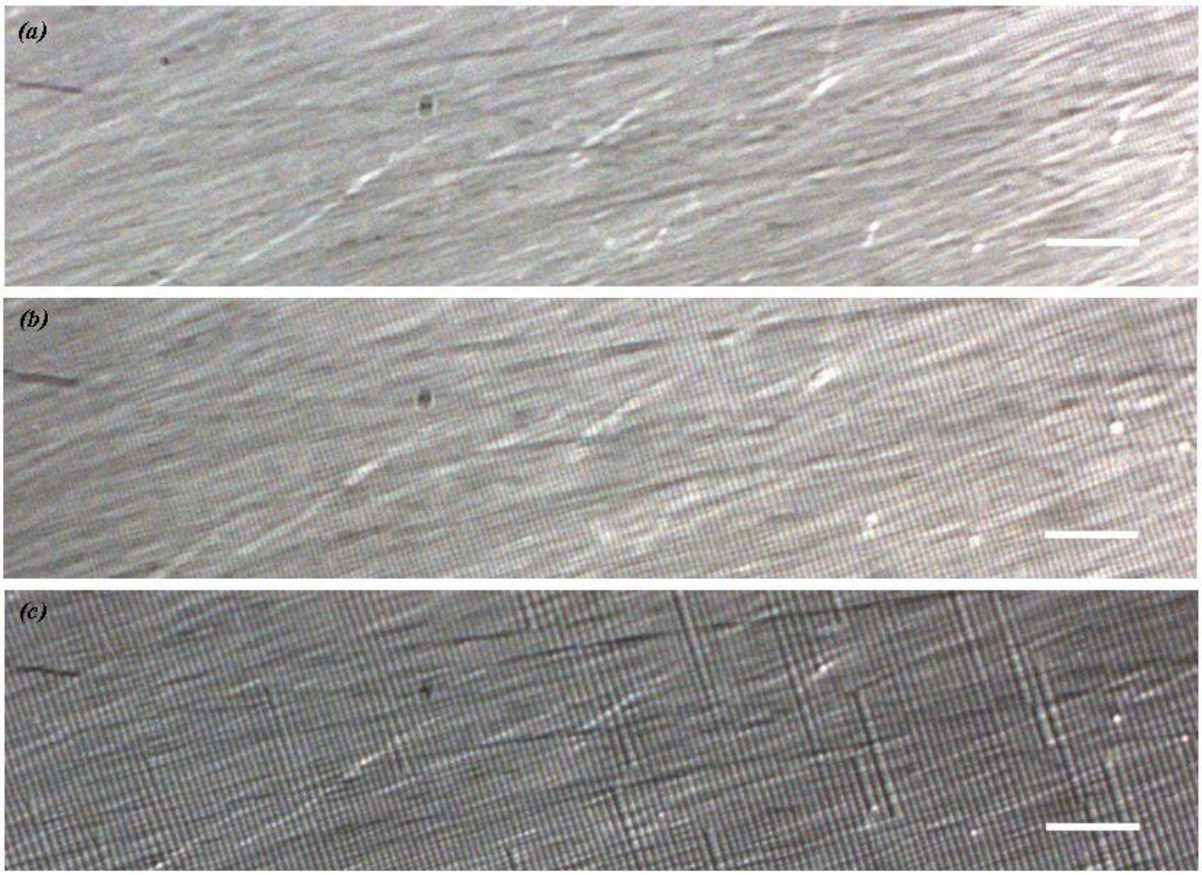

Figure 4.20: POM images of a LD array growing from thick regions (right image side) towards untextured thin regions (left image side) as the temperature was decreased in a closed wedge cell with hybrid anchoring conditions. The same sample region is shown at (a) T = 32.2 °C, (b) T = 32.1 °C and (c) T = 32.0 °C. The scalebar is 20 μm.

As the temperature was further decreased, the FCD lattice stopped expanding and was replaced by a 1D array of LDs in thinner regions of the sample (Fig. 4.20). The LD array appeared at temperature of (32.2 ± 0.1) °C, differing by less than 0.1 °C from the temperature were FCDs were first observed. This shows that the slope of the single Hc1 / H_{c2} transition line for weak bend is very steep as a function of the temperature. It also shows that the bend amplitude H_{c1} for the transition between the bend-free SmA and intermediate state does not depend much on the temperature (see also Fig. 4.21).

The expansion of the LD array as a function of the temperature was less rapid than for FCD (Fig. 4.19), i.e. the slope of the H_{c2} transition line smaller (Fig. 4.21). Interestingly, for a given thickness *h* the period *d* increased as the temperature was decreased (compare Fig. 4.20 (b) and (c)).

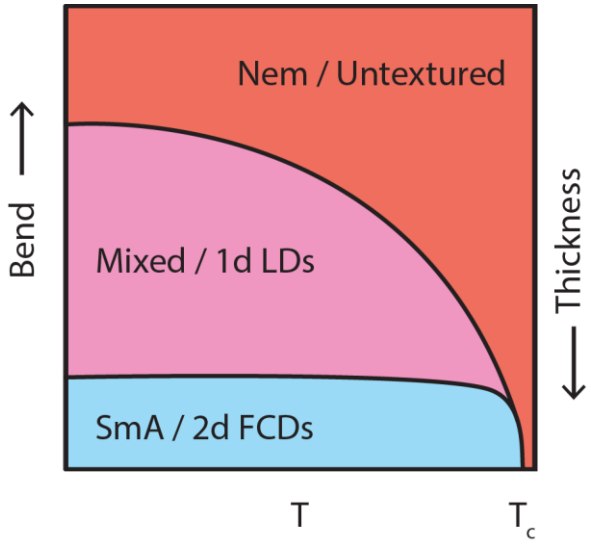

Figure 4.21: Schematic phase diagram of LC compounds showing the 1d/2d transition based on the experimental observation.

Conclusions

The generality of thickness-dependent 1D/2D pattern formation in SmA LC films subjected to hybrid anchoring conditions was confirmed by considering the survey included LCs with different molecular structure and phase sequences, interfaces with different physical properties (deformable air interface and rigid plates), roughness and degree of order (crystalline vs. amorphous polymer surfaces). The studying has also

revealed strong similarities among LD arrays obtained in various cases: the LD period increases in average twice as fast as the LC film thickness and the LD array is replaced by the FCD lattice when reaches a maximum value of about 4.0 - 4.5 μm. The LD period and stability appeared to be dependent on temperature: for a given thickness *h* the period *d* increased as the temperature was decreased, LDs tended to merge with neighboring domains and form wider LDs or striated stripes.

We showed that LD arrays can be created also in planar cells, when the SmA film is confined to a small thickness under the effect of an external electric field. The LD period in twisted and parallel planar cells increases with the inverse of the applied electric field two times slower than in hybrid cells, which cannot be explained by simply considering the electric field-induced director distortions in the Nem phase. Though, the LD period persisted under the field variations in SmA phase for the values larger than the one applied through the Nem – SmA transition, in opposite to hybrid cells, LD arrays created in planar cells were not stable when the field was turned off.

In the last section we addressed a question of the nature of transition from 2D lattices of FCDs to 1D arrays of LDs. Our observations suggest that it cannot be related only to the complex nature of the Nem-SmA phase transition occurring in the presence of strong director distortions. Using the proposed by De Gennes analogy with superconductors[119], we explored the possibility that the observed 2D to 1D transition is a manifestation of the Nem-SmA transition itself, under conditions where phenomena analogue to the Meissner effect and Abrikosov lattice formation are expected. Our investigations of the dependence of LDs and FCDs on temperature and thickness in closed wedge 8CB cells with hybrid anchoring conditions suggest that the material is of type-I and the transition lines between the bend-free SmA phase (FCDs), a ‘mixed’ phase where bend distortion is allowed (LDs) and the Nem phase (untextured regions) coincide for weak bend deformations. Consequently, we assume that the LD arrays are similar to the “intermediate state” of type-I superconductors where stripe domains are frequently observed, due to the coexistence of the Nem and SmA domains.

5. Isotropic and anisotropic nanocrystals in smectic liquid crystal defect patterns

It has long been recognized that guest nanoparticles dispersed in a liquid crystal (LC) host allows tuning key material parameters for electro-optical devices such as optical birefringence, threshold voltage and switching time[96,183]. Guest-host coupling is enhanced and particle segregation can be avoided when LC molecules and nanoparticles have similar shape anisotropy and/or electric polarity. Namely, anisotropic fluorescent dyes[157,158,191,219], ferroelectric nanoparticles[220-222] and nanorods[112,223,224] can show good miscibility and alignment with rod-like LC molecules such as cyanobyphenyls (*n*CB) commonly used in electro-optical devices, and may increase the dielectric anisotropy and stability of the Nem phase[225,226]. A characteristic feature of LCs is the presence of topological defects with a core size of a few nm, inside which the LC order is profoundly altered or completely lost (Chapter 1.4). Defects are long-lived objects with defined length scale, dimension (point, line or walls) and symmetry[133]. The study of their interactions with particles of various sizes and shapes has led to real breakthroughs such as particle-stabilized blue[108,110,227] and twisted grain boundary (TGB)[104,106] phases, defect-assisted molecular assembly of amphiphiles[228] and fabrication of 3D photonic crystals via defect-mediated colloidal assembly[229].

Nanocrystals exhibit unique physico-chemical properties, which can be tuned by modifying their size, shape and composition (e.g. core material, or structure of the nanoparticle capping agent)[182,184,230]. For instance, rod-shaped semiconductor nanocrystals show polarization-dependent absorption and emission[179,231,232]. The self-assembly of nanosized materials has disclosed significant collective properties arising from the nanostructures interaction over large sample areas. Amongst them, a strong photoluminescence with a high anisotropy of semiconductor nanocrystals[233]; polarization-dependent localized surface plasmon resonance (LSPR) of metal nanoparticles (NPs)[76]; spin-dependent electron tunnelling of magnetic-nanocrystal arrays[234], or enhanced p-type electronic conductivity in self-assembled PbTe/Ag_2Te binary nanocrystal superlattices[235]. From the point of view of LC research, one of the most exciting possibility is that: (1) the physical properties of NPs can be tuned by mixing with LCs, (2) the inherent order of organic LCs can be used to guide the assembly of NPs [95,96,146,183,184] and (3) the response

of NPs to external fields can be modulated by introducing a LC matrix with an anisotropic response[95,96,145,146,184].

In the first part of this chapter, 1D arrays formed by SmA LC films with and without electric fields have been used as templating media for controlling the orientation of dispersed anisotropic semiconductor nanocrystals. Namely, colloidal semiconductor core/shell CdSe/CdS dot-in-rods (DRs) with 55 nm length and 7 nm diameter (Chapter 2.2.2) where dispersed in a SmA 8CB (Chapter 2.1) host. The director orientation was determined using polarizing optical microscopy (POM). The localization of DRs and their orientation relative to **n** were determined using fluorescence confocal polarizing microscopy (FCPM), see Chapter 2.5.3 for detailes. By comparing DRs dispersed in 8CB with similar dispersions of spherical core/shell CdSe/ZnS quantum dots (QDs) of a diameter 3.7 nm and anisotropic fluorescent dye Nile Red (NR) (Chapter 2.2.1-2), and pure 8CB samples, we found that anisotropic DR nanocrystals and NR molecules thoroughly align with **n** except in regions where disclination lines are expected, wherein they align along the defects[112]. Electric field directed perpendicular to the defect challenge such defect-induced alignment: DRs tilt away from the defect due to their large permanent dipole moment[236,237]; whereas less polar NR molecules[238] persist in the defect-aligned orientation .

In the second half of the chapter, we studied the evolution of NP/SmA system, i.e. stabilization/destabilization of the LDs as a function of NPs concentration and size. We examined mixtures of isotropic spherical gold nanoparticles (GNPs) of a diameter ranging from 3.8 nm to 50 nm with 8CB in hybrid and homogeneous planar cell geometries. We found out that presence of GNPs leads to LDs destabilization. As the number of particles or/and their size was increased the other type of defects, namely striated stripes, appeared to be favored by the system. Moreover, topological defects present in SmA hybrid cells effectively interact with GNPs, preventing aggregation for the particles concentrations as large as 2 wt % while in the defect-poor SmA homogeneous planar cells aggregation was observed starting from 0.2 wt %.

5.1. Nanoparticle alignment in the absence of fields

Dilute mixtures of NR, DRs or QDs in 8CB with concentration smaller than 1 mM were inserted by capillarity in closed cells with thickness $h < 1.3$ μm in the isotropic (Iso)

phase of 8CB and slowly cooled to the SmA phase (same procedure as for pure 8CB, Chapter 2.2.4). Optical microscopy and FCPM observations showed that particles were uniformly dispersed in the Iso and Nem phases, without aggregation (Fig. 5.1). Anisotropic NR molecules are known to align with their long axis parallel to the director **n**, producing maximum or minimum FCPM intensity when the polarizer *P* is respectively parallel or perpendicular to **n**[239,240]. The same behavior was observed for DRs dispersed in the Nem phase of 8CB confined to homogeneous planar anchoring conditions (Fig. 5.1), i.e. the measured fluorescence intensity was maxsimum when the planar anchoring direction *x* and consequently **n** was parallel to *P* (Fig. 5.1 (a)) and minimum for x, **n**⊥P (Fig. 5.1 (b)).

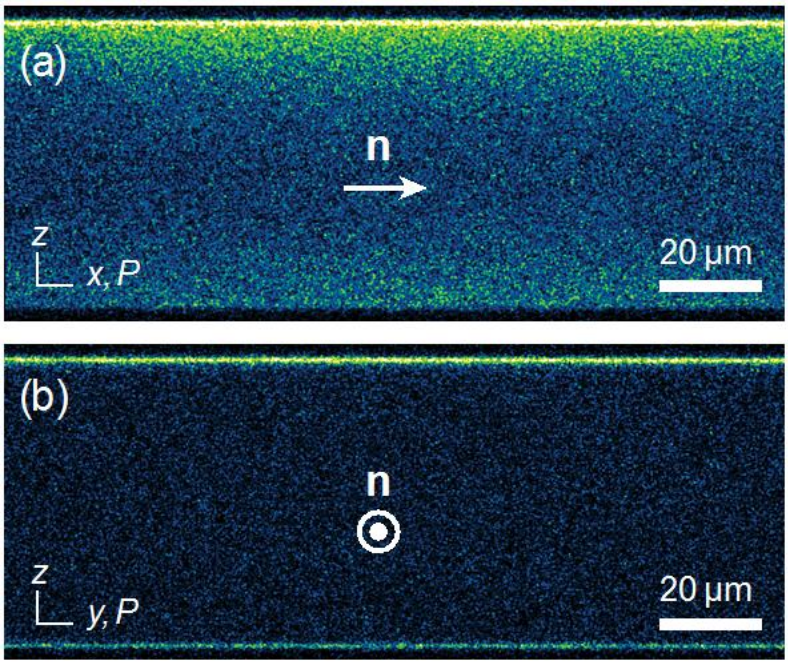

Figure 5.1: FCPM cross sectional images of a uniform planar DR/8CB sample in the Nem phase with the director **n** aligned along the *x* direction. The cell boundaries were coated with PI and rubbed along the direction *x* to induce homogeneous and parallel planar anchoring conditions. Cross sections taken in (a) the *xz* plane with the polarizer *P* parallel to **n** showed a stronger FCPM intensity than (b) *yz* cross sections obtained with *P*⊥**n**. Therefore, DRs aligned with their long axis (and transition dipole) parallel to **n**. Images (a) and (b) correspond to the same sample region, were obtained using equal settings for the laser power, pinhole aperture, intensity gain and all other FCPM parameters, and are shown with the same color scale.

At the transition from the Nem to SmA phase, 1D arrays of LDs appeared, in both NR/8CB and DR/8CB samples (Fig. 5.2). A pattern of alternating dark and bright straight

lines with period d = (0.5 - 1.2) μm, increasing with h [113], was observed also by POM (Fig. 5.3). Dark lines were non-birefringent and corresponded to regions with mainly vertical alignment of the director **n** (at the domain center, $x = 0$ in Fig. 3.4 (a)), whereas bright lines corresponded to regions where **n** was almost parallel to x (at the lateral boundaries with neighboring domains, $x = \pm d/2$)[113].

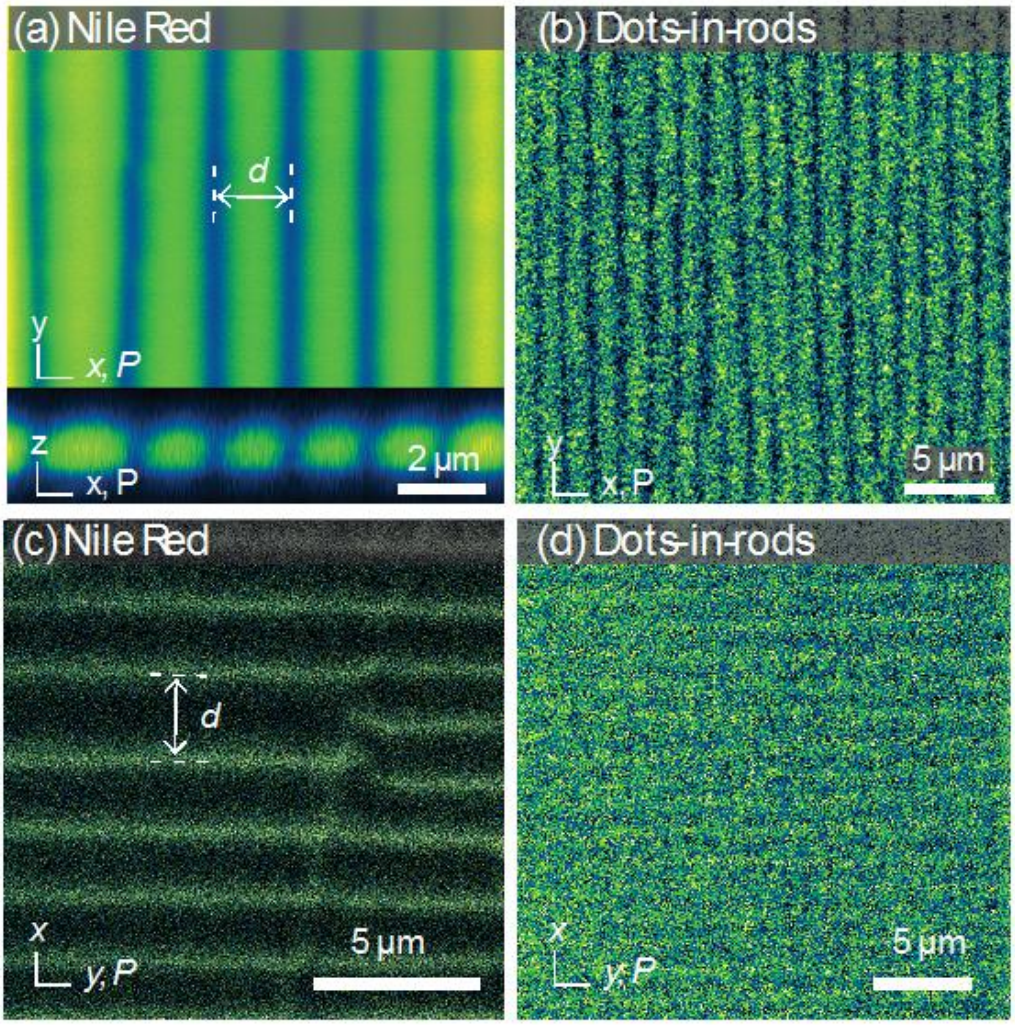

Figure 5.2: FCPM images of dispersed NR (0.3 mM) and DRs (0.1 nM) in SmA 8CB films confined under incompatible anchoring conditions in the absence of electric fields. (a-b) Polarizer P parallel to the planar anchoring direction x. The inset in (a) shows a vertical cross section perpendicular to the defect axis. The top and bottom interfaces imposed parallel and normal anchoring, respectively. (c-d) $P \perp x$. The film thickness was h = (1.0 ± 0.3) μm for NR/8CB and h = (0.6 ± 0.3) μm for DR/8CB.

Comparison of POM images with FCPM images obtained with the polarizer P parallel to the planar anchoring direction x (Fig. 5.2 (a-b)) showed that regions with

mainly vertical **n** corresponded to dark lines in FCPM images, whereas regions with almost planar **n** corresponded to bright FCPM lines. Cross sectional FCPM images taken in the vertical *xz* plane showed that regions with low intensity extended across the whole film thickness (Fig. 5.2 (a), Inset), corresponding to the regions of vertical director alignment observed by POM. These observations suggest that the overall alignment of NR and DRs in SmA 8CB is parallel to the local director **n.** However, when the samples were rotated by 90°, FCPM did not show the uniform low intensity expected for $P \perp \mathbf{n}$ (Fig. 5.2 (c-d)). Regions with almost parallel **n** did become dark and FCPM intensity decreased by more than a twofold factor in DR/8CB samples (Fig. 5.4), but regions with vertical **n** showed a small excess of FCPM intensity. This behavior can be attributed to a local excess of particle concentration in regions with vertical **n** and/or alignment of NR and DRs along the *y* direction (at right angle with **n**). These regions are expected to contain a disclination running along the *y* direction, located on the surface imposing planar anchoring (black dot at point *x,z* = 0 in Fig. 3.4 (a)). FCPM images provide the evidence that the defect is real rather than virtual[75,241] and interacts with nanoparticles[77].

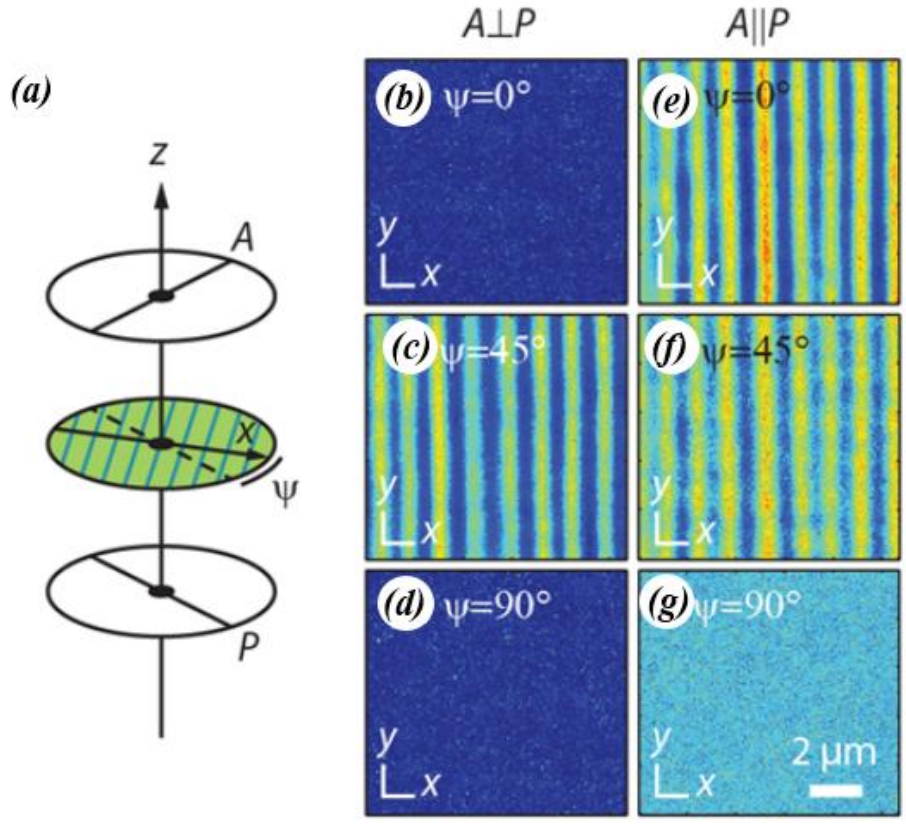

Figure 5.3: POM and lensing effect of a LD array in a thin film of pure SmA 8CB. (a) POM setup: monochromatic green light travelling along the *z* direction passes through the polarizer *P* and analyzer *A*. The direction *x* of planar anchoring forms an angle ψ with *P*

and is perpendicular to the LDs (blue lines). (b-d) Crossed polarizers, $A \perp P$: The sample is uniformly dark when $x||P$ or $x||A$, showing that the director **n** lies in xz plane. When ψ = 45°, a sequence of alternating dark and bright lines appears, corresponding respectively to non-birefringent regions where the average **n** orientation is vertical (along z) and birefringent region with orientation almost parallel x[113]. (e-g) Parallel polarizers, $A||P$: transmitted light is modulated when $x||P$ and uniformly bright when $x||P$. In the former case (e), x-polarized light waves see a modulated refractive index due to the non-uniform director alignment and undergo lensing. In the latter case (g), y-polarized waves are perpendicular to **n** and see a uniform ordinary refractive index.

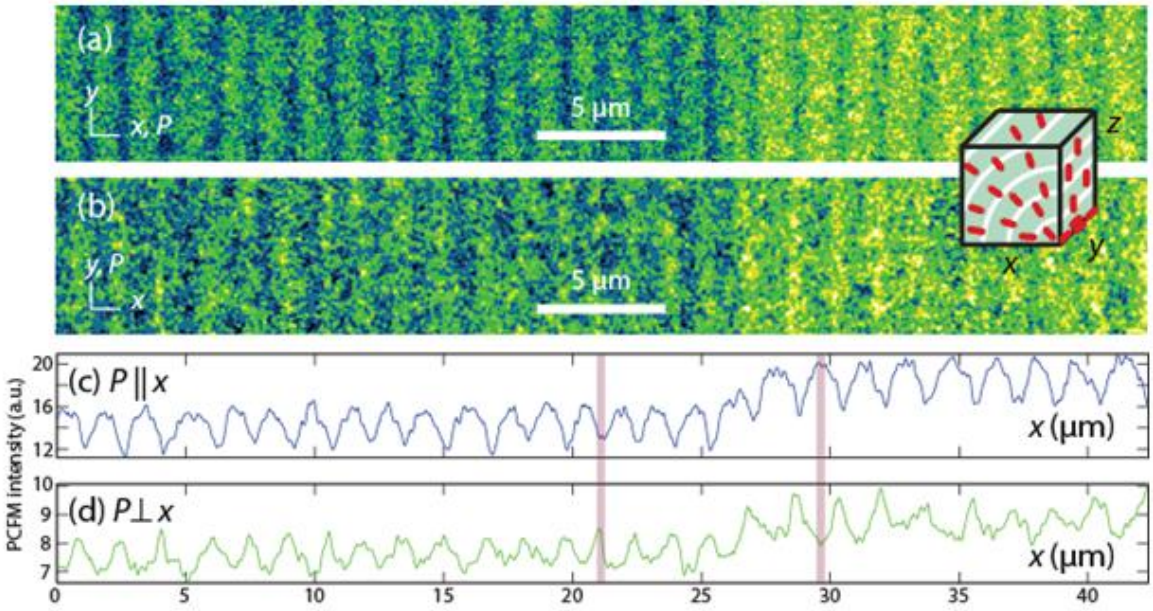

Figure 5.4: (a) FCPM image of a LD array in a 8CB/DRs sample obtained with the polarizer P parallel to the planar anchoring direction x. The dark area to the left was bleached by laser scanning during a previous FCPM image acquisition. (b) The same array observed with $P \perp x$. (c) FCPM intensities measured for the two polarizations and averaged along the y direction. The contrast is reversed in the shaded regions. The inset illustrates the alignment of DRs (red rods) parallel to the disclination at the domain center (bottom right cube edge).

To gain insight on the shape dependence of defect-nanoparticle interaction, dispersions of spherical QD in 8CB have been observed with FCPM (Fig. 5.5). For $P \perp$ **n**, samples appeared uniform and did not show excess FCPM intensity in the vertical **n** regions for QD concentrations reaching the limit value of 1 µM, above which aggregates were formed. Therefore, compared to isotropic particles as for instance QDs, the symmetry interaction between a topological defect and solid particles resulted in nanoparticles oriented parallel to the defects, close to the disclination area, in the case of

anisotropic structures as NRs and DRs. The latter suggests that the disinclination may be composed of a number of topological linear defects of small diameter, namely dislocations. The model of the central defect structure consisted of an array of parallel dislocations was recently proposed as one of the possible scenarios for LDs formed in 8CB open films on PVA[77].

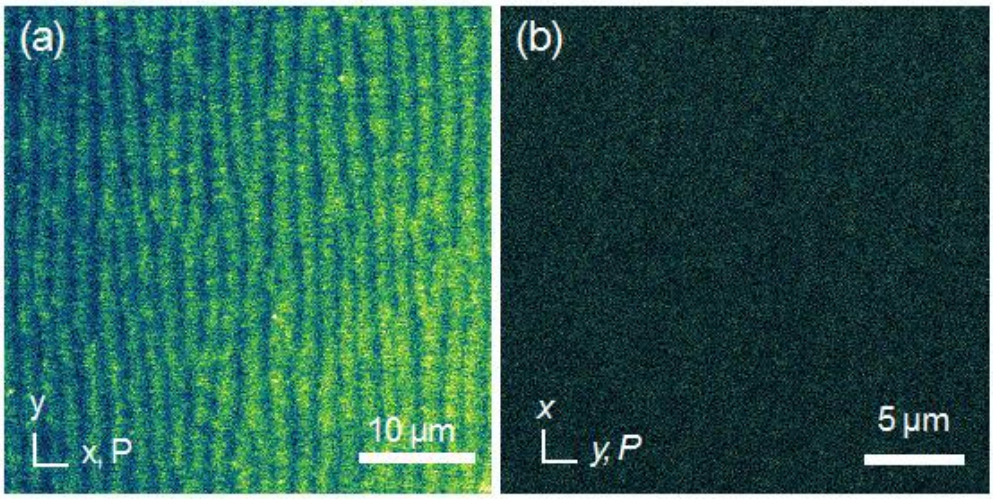

Figure 5.5: FCPM images of dispersed QDs (0.1 µM) in a SmA 8CB film with thickness $h = (0.9 \pm 0.3)$ µm and incompatible anchoring conditions in the absence of electric fields. (a) $P||x$. (b) $P \perp x$.

A 1D space pattern was observed in QD/8CB samples also for $P||x$ (Fig. 5.5), even though QD fluorescence did not show a polarization dependence. This was due to a lensing effect produced by the non-uniform **n** field and refractive index distribution. Indeed **n** is periodically tilted from the vertical along the x direction (Fig. 3.4 (a)). The average refractive index 'perceived' by x-polarized light waves as they cross the film thickness varies from the ordinary value n_0 in regions with vertical **n** (at $x = 0$) to a higher value, close to the extraordinary index n_e, in region with almost planar **n** (at $x = \pm d/2$). Such index modulation creates a lensing effect that focuses light past regions with high refractive index. Lensing was observed by POM also in pure 8CB samples and was completely absent for y-polarized light waves, perpendicular to **n**, that 'encounter' a uniform ordinary refractive index (Fig. 5.3). Lensing also contributes to the FCPM intensity modulation observed for $P||x$ in NR/8CB and DR/8CB samples (Fig. 5.2 (a-b)). However the fact that average fluorescence intensity was twice higher for $P||x$, comparing with $P \perp x$ case (Fig. 5.4) confirms the director alignment with **n.**

5.2. Nanoparticle alignment in the presence of a field

NR/8CB and DR/8CB mixtures were inserted in cells with thickness h = (7 - 15) μm in the Iso phase of 8CB and cooled down to the Nem-SmA transition while applying an AC sine voltage. In the absence of the field the structure corresponds to a lattice of eccentric FCDs, in agreement with the results presented in Chapter 3. When the applied at the transition electric field was $E_{RMS} = V_{RMS} / h < 0.24$ V / μm for NR/8CB and $E_{RMS} < 0.1$ V / μm for DR/8CB, the 2D pattern of FCDs was still observed (Fig. 5.6 (a-b)). When the sample was heated up again to the Nem or Iso phase, then cooled back to the SmA phase with $E_{RMS} > 0.27$ V / μm for NR/8CB and $E_{RMS} > 0.14$ V / μm for DR/8CB, the texture changed into a 1D array of LDs (Fig. 5.6 (c-f)).

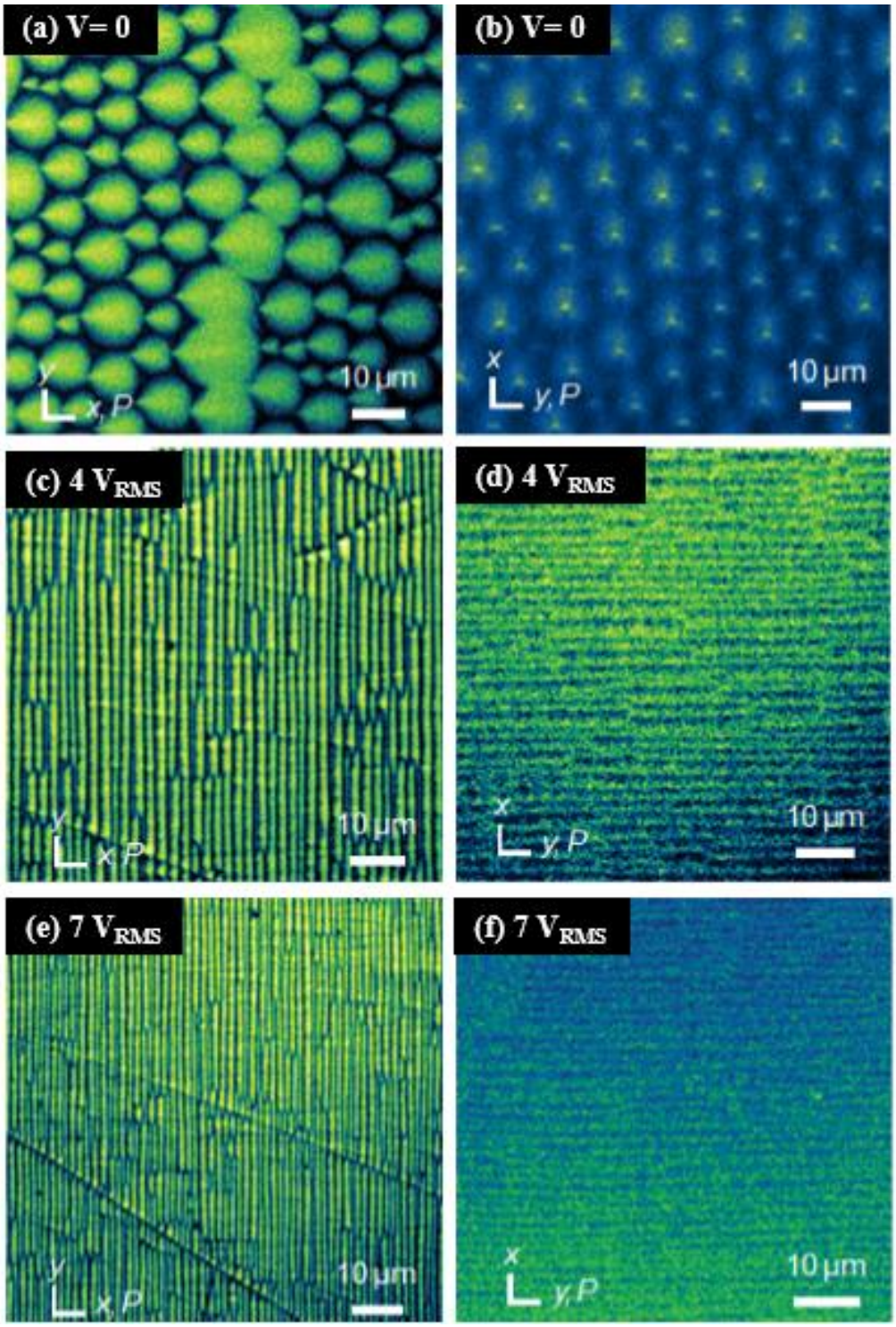

Figure 5.6: FCPM images of 2D/1D patterns obtained by applying a 1 kHz AC voltage with amplitude V_{RMS} in a NR/8CB sample with thickness h = 13 µm. (a, c, e) Polarizer P parallel to the anchoring direction x. (b, d, f) P perpendicular to x.

The arrays period d decreased when E_{RMS} was increased in the Nem or Iso phase before cooling again in the SmA phase (Fig. 5.6, (c, e)). This behavior was previously observed

for pure 8CB and can be understood as a confinement-induced 2D to 1D pattern transition[113] (Charter 3). The director **n** rotates from vertical to planar alignment in a layer with thickness $\xi = V_s/\pi E = (K/\varepsilon_a)^{1/2}/E$ near the interface inducing planar anchoring, where $K = 9$ and $\varepsilon_a \approx 77\times10^{-12}$ F/m for 8CB[242] and the Frederick's transition threshold voltage $Vs = \pi\ (K\ /\ \varepsilon_0\varepsilon_a)^{1/2}$ (Chapter 1.6). Therefore, a sufficiently strong field can confine the director deformation in a surface layer with thickness $\xi < h$, leading to a 2D to1D transition similar to the one obtained by mechanically decreasing *h*. A notable feature of LD arrays formed for $E > 0$, with or without NPs, is that defect formed at the Nem→SmA transition are very stable against field variations and persist for days in the SmA phase even after completing turning off the field. The **n** field inside a LD array is frozen in the particular topology (i.e. types and number of defects) acquired at the transition because creating and removing topological defects amount to overcoming large energy barriers.

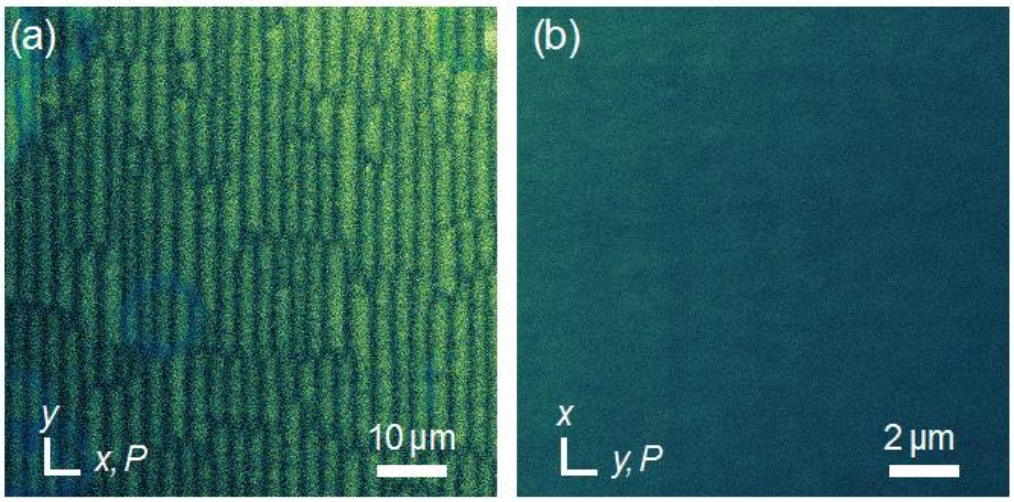

Figure 5.7: FCPM images of an LD array obtained after applying V_{RMS} = 1 V to a DR/8CB sample with thickness h = 7 µm. *x* and *P* are the direction of planar anchoring and polarization, respectively.

LD arrays formed by NR/8CB under applied field showed excess FCPM intensity in regions with vertical **n** when viewed with $P\perp$**n** (Fig. 5.6 (d, f)), similar to that observed in thin samples without field. Therefore, similar topological defect lines interact with NR molecules leading to accumulation and/or alignment along the defect (Fig. 5.2 (c)). In contrast, DRs dispersed in 8CB did not behave as NR molecules: FCPM images obtained with $P\perp$**n** showed a uniform intensity (Fig. 5.7). Evidently, DRs did not accumulate in

space regions with vertical **n** and did not align with their long axis along the *y* direction. Instead, DRs showed the tendency to align along the field. Created under applied electric field the assembly geometry (both the LD array and DRs alignment) persist after switching the field off.

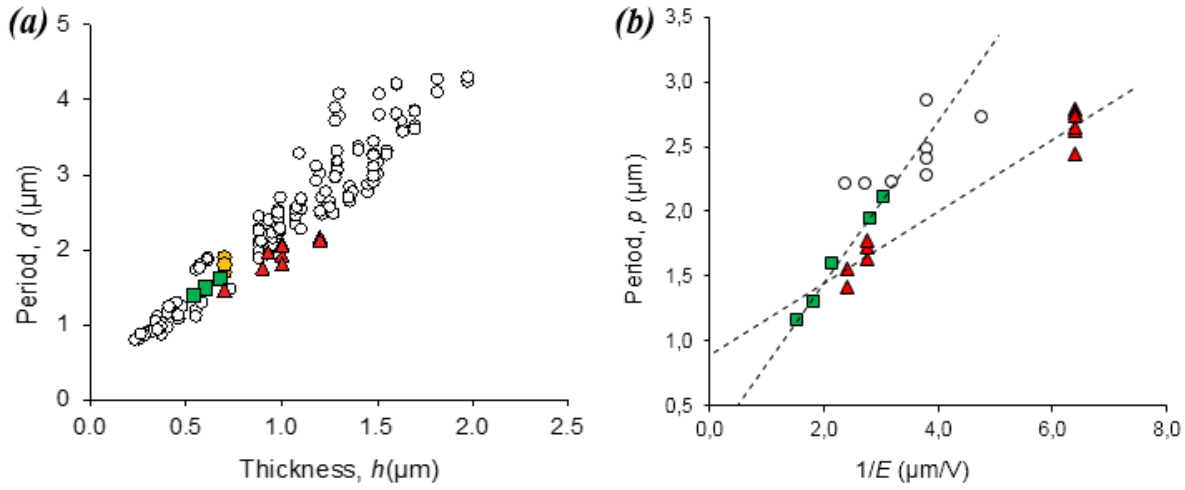

Figure 5.8: Period *d* as a function of sample thickness *h* for LD arrays formed in pure 8CB (empty circles), QDs/8CB (full yellow circles), NRs/8CB (green squares) and DRs/8CB (red triangles) (a) without field and (b) in the presence of a field *E*.

Figure 5.8 shows the period *d* of the LD arrays as a function of the thickness *h* for pure 8CB and NR, DRs and QDs samples. In the absence of fields, dispersed particles did not affect the *d* vs. *h* dependence (Fig. 5.8 (a)). LD arrays result from the balance of bulk elastic and surface anchoring torques, whose strength is expressed by the splay constant *K* and anchoring strength γ, respectively. Therefore, the presence of dispersed particles did not significantly affect *K* or γ. On the other hand, the *d* vs. 1/*E* curve for DR/8CB significantly differed from the curves obtained in 8CB and NR/8CB samples (Fig. 5.8 (b)). Namely, the slope $\partial d/\partial h \propto (K/\varepsilon_a)^{1/2}$ was smaller, suggesting that DRs increased the dielectric anisotropy ε_a of the material. Dispersed anisotropic polar (ferroelectric) and highly polarizable nanoparticles are known to enhance the optical and dielectric anisotropy, as well as lower the threshold for electro-optical switching of LCs[226]. Such evidence represents an explicative example of the large permanent dipole $\mathbf{d}_0$ and/or induced dipole **d** showed by DRs in the direction of the long crystallographic axis (~ 10^2 - 10^3 Debye)[179,236,237] compared to NR (< 10 Debye)[238]. As a consequence, DRs enhance the

dielectric anisotropy ε_a at the relatively low frequency of 1 kHz used in the present work. Moreover, inside the topological irregularities, DRs prefer to align with the field rather than along the defect due to a large gain in electrostatic energy $-E(\mathbf{d}_0 + \mathbf{d}/2)$. Indeed, topological defects trap and align nanosized particles as, upon replacing the defect core with a nanoparticle the free energy is reduced by an amount Kl, where l represents the replaced core length[243]. The alignment of DRs with the field indicates that $E\mathbf{d} > Kl$, therefore the dielectric dipole is $\mathbf{d} > Kl / E$.

In Chap. 4 we showed that 1D arrays can be formed also in cells with homogeneous planar anchoring under application of an electric field through the Nem to SmA transition. Figure 9 shows that also in this case the defects are able to align NRs.

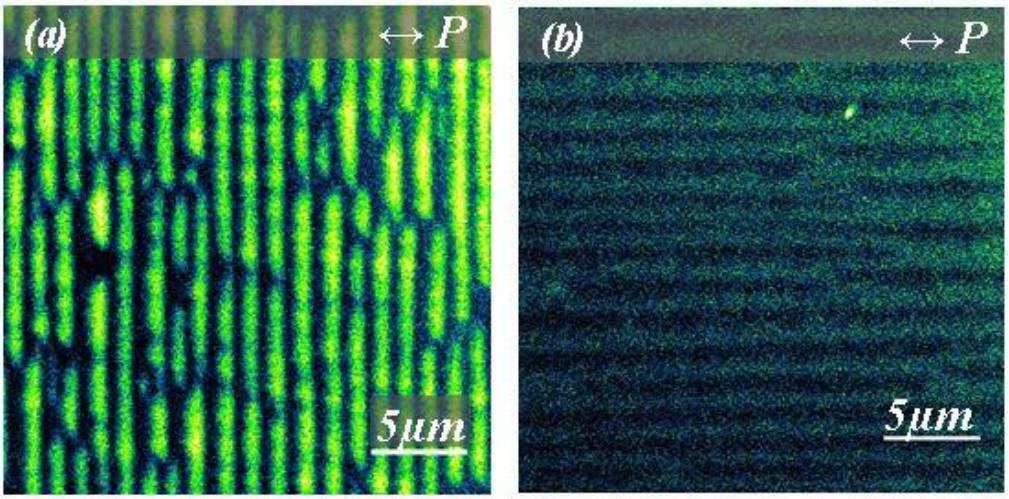

Figure 5.9: FCPM images of 1D/2D patterns obtained by applying a 1 kHz AC voltage with RMS value of 25 V a to SmA 8CB homogeneous planar cell with dispersed NR (0.3 mM). (a) Polarizer P parallel to the planar anchoring direction x. The inset in (a) shows a model of the director distribution in LDs. Molecules is shown as blue rods, SmA layers as lines. **n** is the director, perpendicular to the layers, and h is the thickness of confined region with rotating **n**. (b) $P \perp x$. The sample thickness was $h = 92$ μm.

5.3. The effect of the NP size and concentration on SmA textures

In previous sections the maximum used concentration of 3.7 nm semiconductor QDs in hybrid cells that did not result in aggregate formation and local LC alignment perturbation was 1 μM, which corresponds to 1.3×10^{-3} wt % in 8CB. In GNP/SmA dispersions we increased the particles concentration up to 3 wt % (0.5 mM for the smallest

3.8 nm GNPs) and have tested an effect of the particle size while keeping their concentration constant.

Quasi spherical GNPs with diameter m = (3.8 - 50) nm were dispersed in 8CB at concentrations (0.01 – 3) wt % following the procedure described in details in Chapter 2.2.4. The smallest particles with a size 3.8 nm and 5.8 nm were coated with alkylthiols to avoid aggregation in LC solutions. The other ligands, namely thiols, were used for NPs of diameter m = (10 – 50) nm. Both types of coatings induce homeotropic anchoring of the LC molecules at the NP surface, as has been checked by studying the anchoring of 8CB on a layer of nanoparticles deposited on glass. The obtained mixtures were inserted into closed cells of thickness h = (0.2 – 3) μm by the capillary action while keeping the LC in isotropic (Iso) phase. Pure 8CB samples served as references. We considered two types of closed cells, namely hybrid cells with rubbed PI or PVA layer inducing unidirectional planar anchoring at one interface and OTS coating for homeotropic anchoring at the other interface, and parallel cells with homogeneous planar anchoring (PI or PVA) with rubbing directions parallel to each other. All nanocrystals used in this work, their bulk concentrations c (mass concentration in wt % and molarity), surface density σ (number of particles per 1 μm^2 of a sample of an average thickness 0.5 μm) and the length of a chain made of the number of single particles contained in the sample area of 1 μm^2 are listed in Table 5.1.

Table 5.1:

NPs concentrations in 8CB samples

max QD concentration, c = 0.13×10^{-3} wt %			
Diameter (QD), nm	c, μM	σ, QDs/μm^2	Chain length, nm
3,70	1,00	50	185,00
concentration, c = 0.1 wt %			
Diameter (NP), nm	c, μM	σ, NPs/μm^2	Chain length, nm
3,80	17,54	877	3331,90
5,84	4,83	242	1410,70
10,00	0,96	48	481,13
40,00	0,02	1	30,07
50,00	0,01	0,4	19,25
concentration, c = 1 wt %			
Diameter (NP), nm	c, μM	σ, NPs/μm^2	Chain length, nm
3,80	176,96	8848	33621,88
5,84	48,75	2438	14235,20
10,00	9,71	485	4855,00
40,00	0,15	8	303,44
50,00	0,08	4	194,20
concentration, c = 2 wt %			
Diameter (NP), nm	c, μM	σ, NPs/μm^2	Chain length, nm
3,80	357,53	17876	67929,92
5,84	98,50	4925	28760,91
10,00	19,62	981	9809,08
40,00	0,31	15	613,07
50,00	0,16	8	392,36

5.3.1. Small NPs ($m \leq 10$ nm)

In homogeneous planar cells, the initial relatively free of defects texture (Fig. 4.6 (b)) was not affected by the presence of 0.1 wt % of GNPs, corresponding to 880, 240 and 50 NPs/μm^2 of respective diameter 3.8 nm, 5.8 nm and 10 nm (Fig. 5.10 (a-c)). When the concentration was further increased, small GNPs with m = 3.8 nm behaved in a different way from larger GNPs with m = 5.8 nm and 10 nm. Up to the concentrations of 2 wt % and 18×10^3 NPs/μm^2 no texture change was observed for the smallest particles of 3.8 nm, showing very high mixability in SmA LCs (Fig. 5.10 (d)). For comparison, an

extensive agglomeration of 3.8 nm GNPs in Nem 5CB was already observed at concentration 1 wt %[244].

In SmA films subjected to homogeneous planar anchoring and the same concentration of 2 wt % the aggregation was revealed for larger particles of diameter 5.8 nm and 10 nm (Fig. 5.10 (e-f)). This corresponds to a smaller number of particles per 1 μm^2, than for 3.8 nm, respectively 5×10^3 and 10^3 NPs, suggesting that the effect of NP size on the aggregate formation process is also important, in addition to the influence of NP concentration: for the GNPs of diameter 5.8 nm and 10 nm the first aggregates were observed at about 1 wt % in 8CB (the surface density 2.5×10^3 NP/ μm^2 and 0.5×10^3 NP/ μm^2 respectively), whereas only very few aggregates were observed in homogeneous planar cells containing 3 wt % (27×10^3 NPs/μm^2) of 3.8 nm GNPs.

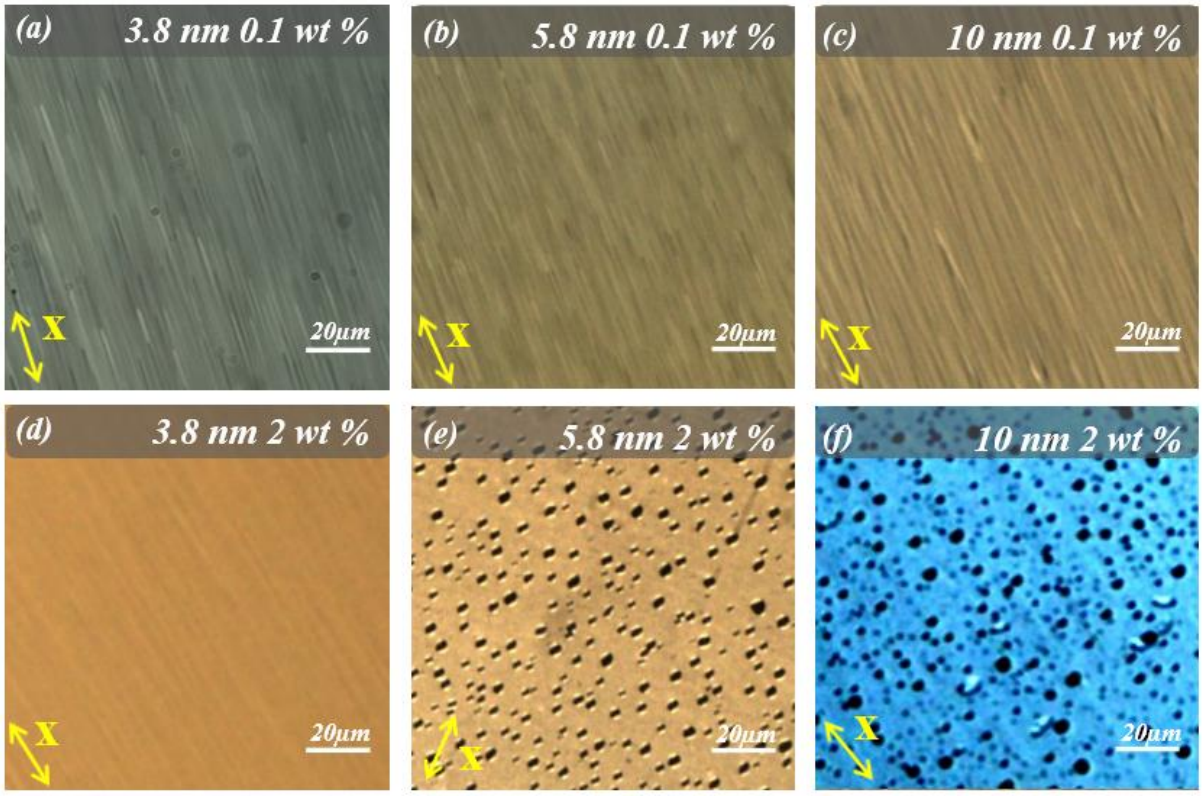

Figure 5.10: POM micrographs showing the SmA textures of homogeneous planar cells formed in (a-c) 0.1 wt %, (d-f) 2 wt % 8CB/GNPs dispersions with different NP diameter: (a, d) 3.8 nm, (b, e) 5.8 nm and (c, f) 10 nm. Arrows indicate the rubbing direction. Images were taken under the crossed polarizers.

In hybrid cells with pure 8CB, the texture is a periodic 1D pattern with straight LDs (Fig. 4.1-2). As in planar cells, adding 0.1 wt % of GNPs with m < 10 nm did not induce aggregation (Fig. 5.10). This is in contrast with hybrid cells containing about 50 QDs/μm^2 of diameter 3.7 nm, where agglomerate formation was observed. The latter suggests a stronger disordering effect of the ligands around the QDs, with respect to the alkylthiols[95]. However, even such small GNP concentration was sufficient to destabilize the LD arrays. After being formed at the Nem-SmA transition, LDs tended to be replaced by striated stripes (Fig. 5.11), a different type of domains with a transverse modulation that is often observed also in pure 8CB. The number of striated stripes increased as time elapsed. About (10 - 20) % of LDs were replaced by striated stripes within a day for GNPs with m = 3.8 nm. The amount of striated stripes appeared to increase with the GNPs size (Fig. 5.11).

LD arrays formed in hybrid cells containing QDs with m = 3.7 nm at concentration 18 times smaller than GNPs of the comparable size were rather stable, i.e. striated stripes appeared at the same rate and number as in pure 8CB. On the other hand, 3.7 nm QDs tend to form agglomerates in hybrid 8CB samples, in contrary to GNPs dispersions subjected to the same conditions.

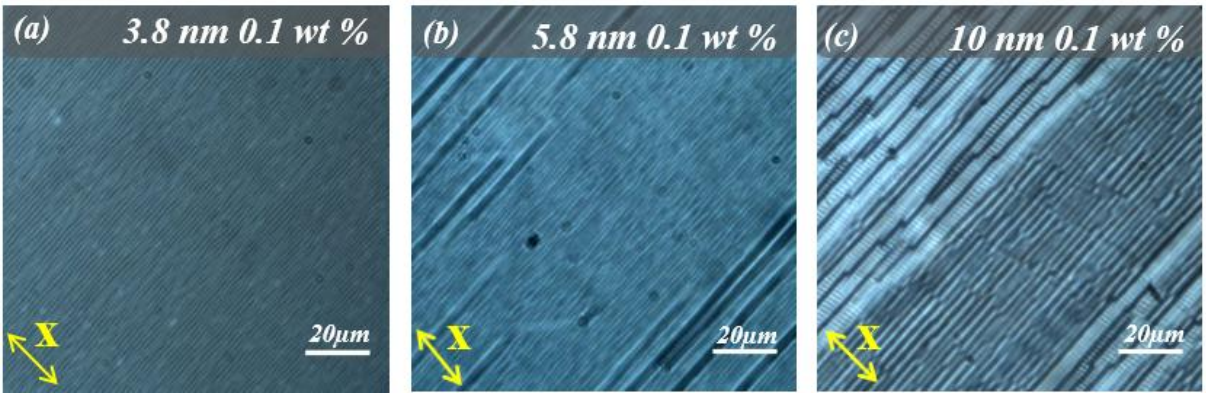

Figure 5.11: POM micrographs taken 5 minutes after LDs appearance, showing the SmA textures of hybrid cells formed in 0.1 wt % 8CB/GNPs dispersions with different NP diameter: (a) m = 3.8 nm, (b) m = 5.8 nm and (c) m = 10 nm. Arrows indicate the rubbing direction. Images were taken under the crossed polarizers.

A further increase of the GNPs concentration in the hybrid cells induce the formation of much larger number of striated stripes. The LD arrays were mainly all replaced by striated stripes after one day, in the cells containing 2 wt % of 3.8 nm GNPs (Fig. 5.12 (a)). Even in the thinnest regions of the sample of about 300 nm and less, where

the optical microscopy resolution does not allow the observation of LDs, striated stripes were formed (Fig. 5.12 (b)).

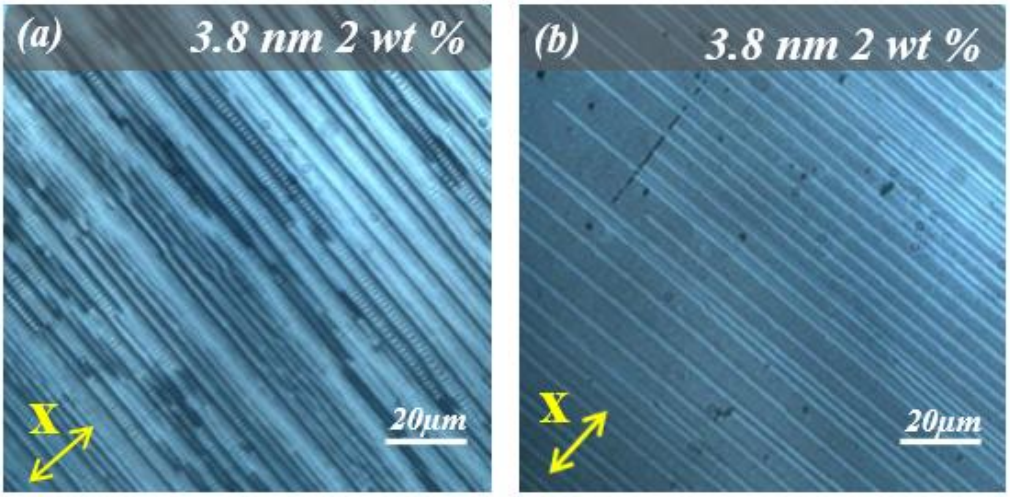

Figure 5.12: POM micrographs showing the SmA textures formed in 2 wt % 8CB/GNPs dispersion of 3.8 nm diameter in hybrid cells of thickness (a) $h \approx 0.8$ μm and (b) $h \approx$ (0.2 - 0.3) μm. Arrows indicate the rubbing direction. Images were taken under the crossed polarizers.

The tendency of striated stripes to appear with time in hybrid closed cells in presence of GNPs of size $m \leq 10$ nm differs from the behavior observed in open films containing GNPs with m = (3.8 – 10) nm or QDs with $m \approx 6$ nm. In this case, the presence of 3.8 nm GNPs with concentrations up to 2 wt %[76,245], which corresponds to a surface density varying between 2600 and 5000 GNPs/μm^2, stabilized the LDs against the formation of striated stripes without time evolution. For a given thickness of LC films, around 300nm, where a large number of striated stripes was formed in pure 8CB, in the presence of NPs the amount of striated stripes was significantly reduced and an array of thin linear defects were formed suggesting an opposite behavior in open cell[76]. Localized surface plasmon resonance (LSPR) measurements have revealed that single NP chains were formed within LDs in 1.3 wt % of 3.8 nm GNPs in open 8CB films[246]. For GNPs of larger size, 5.8 nm, stabilization of LDs has been also observed, but coexisting with aggregates. First results obtained for 10 nm GNPs suggest that stabilization also occurs, but more investigations are necessary.

An important difference between open LC films and closed cells containing NPs is their thickness, which is typically much smaller for open cells, implying different surface

density of NPs for the same bulk concentration *c*, as well as different number of LDs per unit sample area. For a given bulk concentration *c* of nanoparticles, the surface density $\sigma_{NP} = ch$ increases as the thickness *h* increases, while the surface density of LDs decreases $\sigma_{LD} = \frac{1}{d} \approx \frac{1}{2h}$. If we consider a typical open cell thickness of 200 nm, the number of 3.8 nm GNPs per 1 LD which corresponds to *c* = 1.3 wt % and single chain regime in 8CB films was 1.8×10^3. To obtain the same number of 3.8 nm GNPs in one LD in closed cells of typical thickness (0.5 – 1) μm used for creating LD arrays the bulk NP concentration must lie in a range (0.1 – 0.2) wt %. The number of NPs per single linear defect domain corresponding to *c* = 2 wt % in open cells, where LDs were still stabilized, appeared to be very close to the one expected in 500 nm closed cells with *c* = 0.3 wt %. However, in the latter case striated stripes were more stable. Such inverse behavior suggests that the number of trapping areas, most probably topological defects, is different in open and closed cells, being larger for LDs in open films and striated stripes in closed cells.

Our studying of SmA textures of different LCs created using various aligning surfaces and samples geometries revealed strong similarities among LD arrays formed by 8CB in open and close cells. Consequently, we could expect the central area of the LD to be similar in closed cells and open films[77]. In the presence of NPs the area can be modified, possibly with a variation from a central 2D nematic defect to an array of dislocations stabilized by NPs. However the structure close to the curvature walls may be different, due to the surface curvature, which is allowed in open films but not permitted in closed cells. Thus, in closed cells dislocations may be absent in LDs, but present in striated stripes.

5.3.2. Large NPs (*m* = 40 – 50 nm)

In homogeneous planar cells, dispersion of GNPs with larger size *m* = (40 – 50) nm in 8CB films did not affect the samples morphology up to the concentrations of 0.1 wt % (Fig. 5.13 (a)). When the concentration of GNPs was increased to 0.2 wt % (2 and 1 NPs/μm^2 respectively for 40 nm and 50 nm NPs) in LC, aggregates of different sizes were formed (Fig. 5.13 (b-c)). The amount of aggregates increased when we further increased the concentration of GNPs (Fig. 5.14 (d)). Larger aggregates nucleated in the thicker regions of the samples, most likely due to a presence of larger number of NPs in thicker areas.

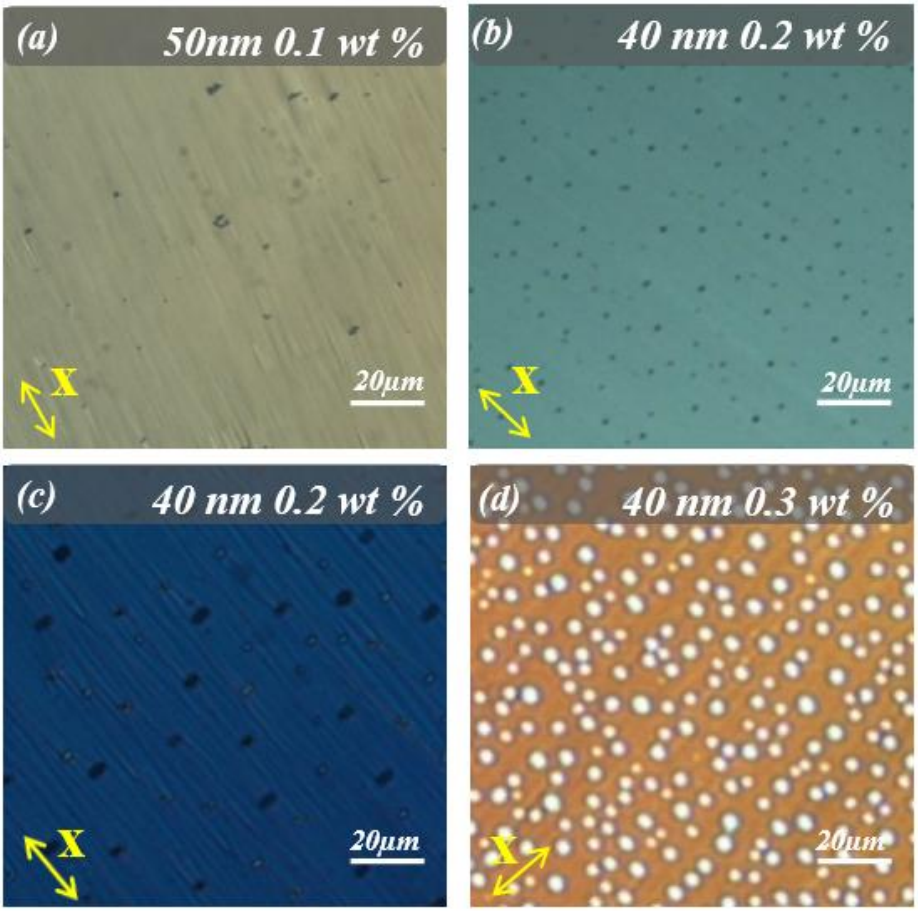

Figure 5.13: POM micrographs showing the SmA textures of homogeneous planar cells formed in 8CB containing (a) 0.1 wt % of GNPs with a diameter 50 nm, the cell thickness $h \approx 0.3$ μm; and 40 nm in diameter GNPs of concentration (b) 0.2 wt %, $h \approx 0.5$ μm, (b) 0.2 wt %, $h \approx 1$ μm and (c) 0.3 wt %, $h \approx 0.8$ μm. The aggregates amount increased with the NPs concentration and their size increased with the cell thickness. Arrows indicate the rubbing direction. Images were taken under the crossed polarizers.

In hybrid cells, the concentration of large GNPs with m = (40 – 50) nm could be increased without creating aggregates up to 1 wt % (8 - 4 NPs/μm^2 respectively), significantly more than in planar cells. The latter may suggest that a large number of favorable areas which can be either highly distorted areas or topological defects present in hybrid cells effectively interact with GNPs, reducing interparticle interactions and preventing aggregation, whereas GNP can diffuse and aggregate more freely in the defect-poor texture of planar cells. However, the trapping occurs for striated structures in closed cells instead of LDs.

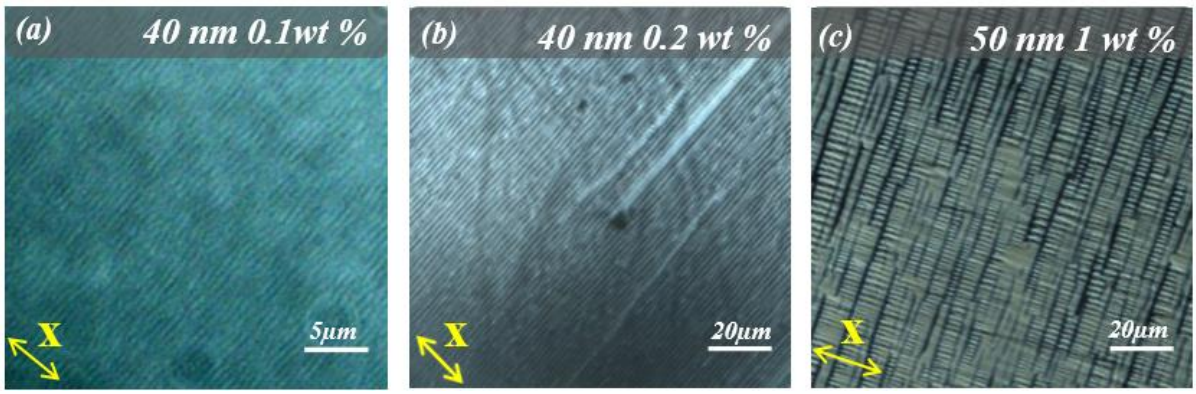

Figure 5.14: POM micrographs showing the SmA textures of hybrid cells formed in 8CB containing (a) 0.1 wt % of GNPs with a diameter 40 nm, (b) 0.2 wt % of GNPs with a diameter 40 nm and (c) 1 wt % of GNPs with a diameter 50 nm. The striated stripes fraction increased with the NPs concentration. Arrows indicate the rubbing direction. Images were taken under the crossed polarizers.

The presence of GNPs with diameter 40 nm and 50 nm has strongly destabilized LD arrays formed in hybrid cells starting from 0.1 wt % concentration. LDs were distorted, appearing not straight even for very small LC film thicknesses of about (300 – 500) nm (Fig. 5.14 (a)). Moreover, the amount of the appeared striated stripes notably increased comparing with cells containing NPs of smaller sizes (Fig. 5.11). The striated stripes fraction increased with the GNPs concentration (Fig. 5.14) and with time (Fig. 5.15). In 30 min about 60 % of an area covered with LDs was replaced by striated stripes and within a day striated stripes constituted about 95% of the sample with GNPs of diameter 40 nm and concentration 0.1 wt % (Fig. 5.15 (b-c)).

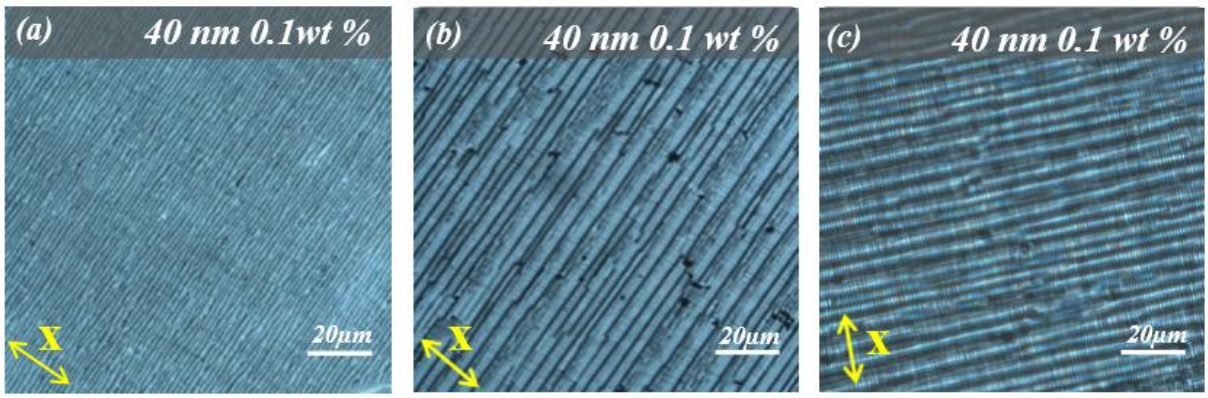

Figure 5.15: POM micrographs showing the dynamic evolution of SmA textures of a hybrid cell formed in 8CB containing 0.1 wt % of GNPs with a diameter 40 nm (a) right after the Nem → SmA phase transition, (b) 1 hour latter and (c) after 1 day. The striated

stripes fraction increased with time, covering about 95 % of the sample area within a day. Arrows indicate the rubbing direction. Images were taken under the crossed polarizers.

The fact that the hybrid cells containing GNPs were not stable with time, i.e. striated stripes were formed not at the Nem → SmA transition but after LDs formation, replacing a LD array, could let us assume that not all the NPs dispersed in 8CB were trapped in a liquid crystal bulk by the defects formed at the phase transition and possibly were moving towards the substrate causing a change of anchoring. However, these striated structures are known to occur in pure 8CB cells (Fig. 4.7), but still unidirectional anchoring. We can thus withdraw this hypothesis. Two other hypotheses can be proposed:

- The topological defects of LD arrays are of small disordered core, and thus large NPs, destabilizing the 8CB structure around the defects core, finally destabilize the overall structure. However, the fact that this phenomenon occurs even for GNPs as small as 3.8 nm and concentrations of 0.1 wt % indicates that this hypothesis cannot explain the observed behavior by itself.
- The number of topological defects or highly distorted areas in the striated stripes is larger than in the LDs. This may explain why the striated stripes are better stabilized by GNPs with large concentrations than LDs.

In open cells it has been shown that all GNPs are localized in the topological defects, forming chains parallel to LDs[76]. In the closed cells such information could not be obtained due to the presence of two substrates, which made the LSPR signal too low for efficient measurements. If we assume that all GNPs are trapped by linear topological defects, in the 0.5 μm thick closed cell where we expect 1 LD domain per 1 μm^2, next values will be obtained:

1 wt % of 50 nm GNPs will make a chain of 0.2 μm (1 line),

2 wt % of 5.8 nm GNPs will make a chain of 29μm (29 lines),

2 wt % of 3.8 nm GNPs will make a chain of 68 μm (68 lines).

These numbers are definitely large, but in LDs of open cells may correspond to the trapping areas associated with dislocations and a large 2D defects, recently revealed on

PVA substrates by combining X-ray diffraction and ellipsometry[77]. A high mixibility with small 3.8 nm GNPs observed in homogeneous planar cells makes it to be not apparent that all GNPs may be trapped into defects in the hybrid cells. It would thus be interesting to increase now the number of larger GNPs in the hybrid cells to check, if the striated stripes still remain stable, without aggregation, whereas aggregates are formed in homogeneous cells. This would be an interesting way of estimating the number of topological defects in closed cells.

In the homogeneous planar cells, the particle size also strongly affects the mechanism of aggregation. For GNPs of diameter 40 nm and 50 nm a large number of aggregates was observed starting from 0.2 wt % of gold in 8CB. However, this occurred to be not the case for GNPs of smaller size, in particular no aggregates were formed by 3.8 nm GNPs of the same 2 wt % concentration, which corresponds to approximately 10000 times more particles contained in LC than it was for NPs of diameter 40 nm. This phenomenon may be due to larger Van der Waals interactions between larger NPs, favoring aggregate formation.

5.3.3. Dark field microscopy (DFM) measurements

To evidence the NPs localization inside the LC patterns created in the hybrid 8CB/GNPs cells DFM observations of were performed. High-contrast DFM images are formed only by the scattered light coming from the sample. In the presence of NPs depending on their size the elastic light-scattering process may be more favorable in interaction with incident light waves. Starting from nanoparticle size of about 30 nm scattering begins to be significant[181]. The scheme and principles of DFM are described in the Chapter 2.5.4.

We have tested the 8CB hybrid cells containing GNPs of different sizes d = (3.8 - 50) nm and pure 8CB cells. No notable difference in DFM images of closed cells filled with LC only and with LC/GNPs dispersions were revealed. For pure 8CB and 8CB with GNPs the regions of the samples consist of the same defect type, such as LDs, striated stripes or FCDs, looked similar (Fig. 5.16).

Presence of the defect texture made DFM to be not informative technique for determining GNPs localization in hybrid cells. The smectic pattern was likely to hide the nanoparticle scattering signal.

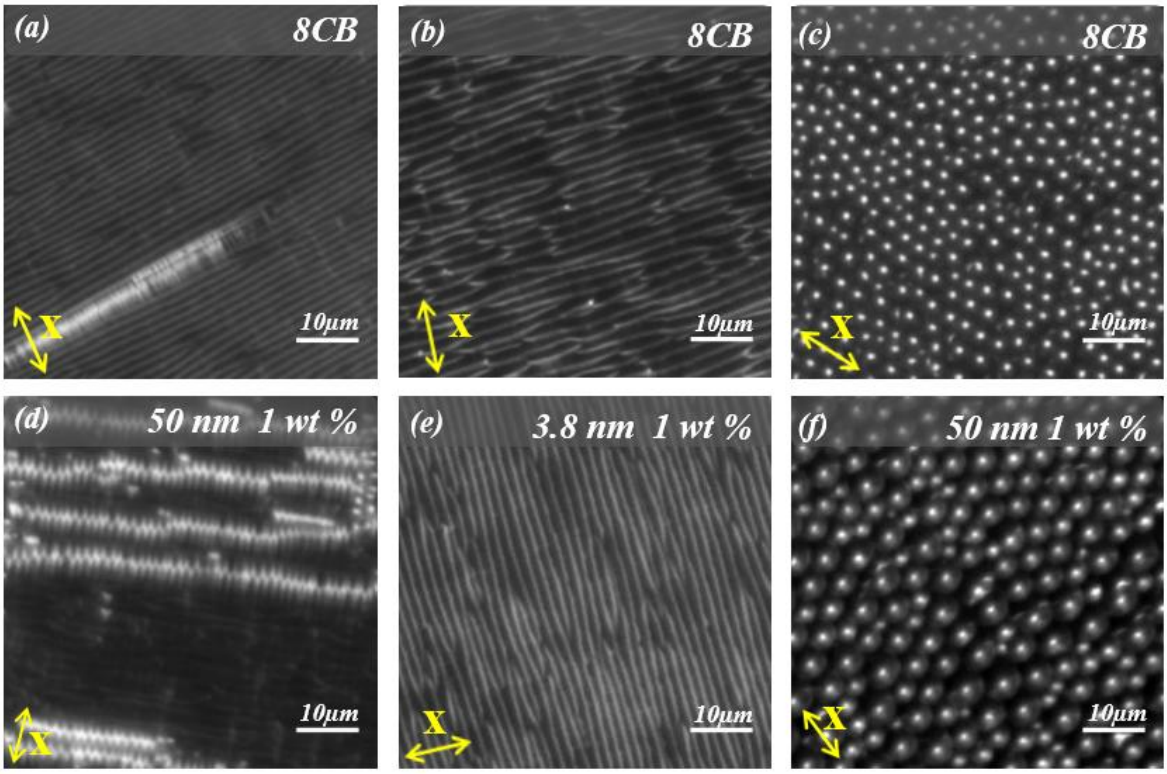

Figure 5.16: DFM images showing the SmA textures of hybrid cells formed in (a-c) pure 8CB and 8CB containing 1 wt % of GNPs with a diameter (d, f) 50 nm and (e) 3.8 nm. Arrows indicate the rubbing direction.

Conclusions

We created highly oriented 1D arrays and 2D lattices of defect domains in SmA LC/nanoparticles dispersions. We found out that anisotropic dye molecules are trapped and oriented by topological linear defects (disclinations), which is in agreement with ref [112], and form 1D periodic linear arrays made of oriented particles perpendicular to the director **n**. We evidenced their localization in the homeotropic regions of the linear defect domains. Both the pattern type (1D/2D) and the period of oriented particles can be controlled and reversibly changed by varying the SmA LC film thickness and/or external electric field.

Analogous to the dye molecules semiconductor DRs are found to be trapped in the 'homeotropic' regions of the linear defect domains and oriented by disclinations perpendicular to the director in the absence of the external electric field. However, when the defects were created by applied electric field, DR alignment was strongly affected by

the field. First, the LD period decreased slowly with increasing E_{RMS} comparing to pure 8CB and NR/8CB samples, suggesting that DRs increased the dielectric anisotropy of the material. Second, DRs were aligning with the field rather than along the defects, due to a large gain in electrostatic energy.

FCPM measurements performed on the samples with spherical QDs of various concentrations (up to 1 μM or 1.3×10^{-3} wt % in LC) suggest no increase of a particles number inside the linear defects, comparing with an average particles concentration in the SmA LC film.

Adding larger concentrations (above 0.1 wt %) of spherical GNPs to hybrid SmA LCs cells leads to destabilization of the LDs and stabilization of striated stripes, while preventing particle aggregation even for large concentration of GNPs. The amount of nucleated striated stripes in hybrid cells and the number of aggregates formed in homogeneous planar cells increase with the size of GNPs and/or with their concentration. Such behavior indicates that in LD arrays formed in closed hybrid cells the amount of topological defects is smaller, comparing to the open cells. As a consequence in presence of GNPs we stabilize a structure rich of topological defects – the striated stripes.

General conclusions

An increasing scientific interest in liquid crystalline materials has arisen from their ability to guide the assembly of colloids[15,229] and NPs[76,95-97,145,184] into well-defined spatial patterns. However, the experimental realization of self-assembling switchable composites remains a significant challenge, as it requires nanoscale controlling of the particles arrangement into the tunable LC matrices using the fundamental interactions between the LC host and nanomaterials and transferring those properties to the macroscopic scale over a few millimeters. This thesis is devoted to the study the SmA LCs which produce 1D and 2D patterns of nanometer size defects[44] with sub-micrometer periodicity and are capable to assemble NPs into ordered structures via defect/NP interactions. The dissertation focuses on two main tasks: to develop a reliable method for creation topological defect patterns with predefined symmetry and periodicity which can be tuned by an electric field application; to assemble NPs of different nature, size and shape into ordered structures within tunable LC defect arrays.

Summarizing the results of this thesis we can affirm that:

Formation of 1D arrays of LDs and 2D lattices of FCDs is a general feature of SmA LC films[38,39,74] subjected to hybrid anchoring conditions, that appeared to be largely independent from the LC chemical structure and phase sequence, physical properties of the interfaces (deformable air interface and rigid plates), roughness and degree of order (crystalline vs. amorphous polymer surfaces).

The morphology of SmA patterns is determined by the thickness of the layer where the LC director rotates from normal to parallel to the substrates orientation. This thickness can be controlled by mechanical confinement or by applied electric fields[113]. LDs are observed when the layer thickness is smaller than about 1.3 μm, while FCDs appear in thicker layers and develop into a close-packed 2D hexagonal lattice for the thickness above 2 μm. We found out that the linear dependence of LD and FCD periodicity on the layer thickness is typical for both open LC films and closed cells.

The electric field application during the Nem-SmA phase transition allows effective controlling the LD periodicity, which linearly increases with the inverse of the electric field.

In the case of hybrid cells the resulting configuration is stable against the electric field variations in the SmA phase and keeps its characteristics after switching the field off. Whereas in the planar cells switching electric field off leads to appearance of FCDs.

The transition from 2D lattices of FCDs to 1D arrays of LDs occurs in the presence of strong director distortions. We suggest that this transition is a manifestation of the Nem-SmA transition itself, according to the analogy with superconductors proposed by De Gennes[119]. The direct investigations of the LDs and FCDs dependence on temperature and thickness in closed wedge cells lead us to assumption that 8CB is the type-I superconductor and thus, the LD arrays should be similar to the "intermediate state" of type-I superconductors.

In SmA LC/nanoparticles dispersions we created tunable periodic defect patterns whose symmetry (1D or 2D) and periodicity could be controlled by the electric fields. We found out that in the absence of the electric field anisotropic dye molecules as well as semiconductor DRs are trapped and aligned by linear defects parallel to LD arrays[112] and are localized in homeotropic regions of the linear defect domains. When 1D patterns were created by applied electric field, the alignment of dye molecules did not change, while DRs were oriented along the field due to a large gain in electrostatic energy. An obtained small slope of the period d vs. E^{-1} dependence, comparing to pure 8CB, suggests that DRs increased the dielectric anisotropy of the material.

No increase of a particles number inside the linear defects, comparing with an average particles concentration in the SmA LC film was evidenced by FCPM measurements performed on the samples with spherical QDs of various concentrations (up to 1 μM or 1.3×10^{-3} wt % in LC matrix).

Destabilization of the LDs and stabilization of striated stripes occurred in hybrid SmA LC cells at concentrations of spherical GNPs above 0.1 wt %. The morphology of SmA phase in hybrid cells prevents particle aggregation even for large concentration of GNPs. An increase of GNPs concentration as well as their size resulted in increase of striated stripes quantity in hybrid cells and a number of aggregates in planar cells. Such behavior indicates that an amount of topological defects should be larger in striated stripes than in LDs of closed cells.

While the study in this thesis demonstrates the possibility of periodic defect patterns creation in SmA LC films with their further tuning by electric fields, the internal defect structure in such system is still unclear and the detailed investigation is necessary. Exploiting the X-ray diffraction measurements can help to reveal the smectic layer arrangement within the defect domains and therefore to understand the number and type of topological defects present. The latter in turn will help to explain the defect/NPs interactions and to foresee an arrangement of nanoobjects of different size, shape, nature and concentrations. It is an important step on a way for creation of composite metamaterials, which would combine the unique properties of nanoscale materials and ordered liquid crystalline phases. Moreover, it will be interesting to study the other sample geometries, possibly with some exotic boundary conditions, where different types of topological defects can be created. For example, a single linear defect can be formed by SmA LCs inserted into capillaries with homeotropic anchoring on the boundaries. Thus, investigation of smectic LCs opens new perspectives for both fundamental science and applications standpoints.

Bibliography

[1] G.M. Whitesides, J.P. Mathias, and C.T. Seto, *Molecular self assembly and nanochemistry*, Science **254** (5036), 1312 (1991).

[2] P. Ball, *The self-made tapestry: pattern formation in nature*. (New York: Oxford University Press, 1999).

[3] P. J. G. Butler, *Self-assembly of tobacco mosaic virus: the role of an intermediate aggregate in generating both specificity and speed*, Philosophical Transactions of the Royal Society of London Series B-Biological Sciences **354** (1383), 537 (1999).

[4] S. Zhang, *Encyclopedia of materials: Science and technology. Molecular self-assembly*. (Elsevier Science Ltd., 2001), pp.5822.

[5] Commission on Engineering and Technical Systems Committee on Synthetic Hierarchical Structures, National Research Council, *Hierarchical structures in biology as a guide for new materials technology*. (National Academy Press, Washington D. C, 1994).

[6] Philip Ball, *Made to Measure: New Materials for the 21st Century*. (Princeton University Press, 1998).

[7] H. I. Smith, M. L. Schattenburg, S. D. Hector, J. Ferrera, E. E. Moon, I. Y. Yang, and M. Burkhardt, *X-ray nanolithography: Extension to the limits of the lithographic process*, Microelectronic Engineering **32** (1-4), 143 (1996).

[8] J. O. Choi, H. S. Jeong, D. G. Pflug, A. I. Akinwande, and H. I. Smith, *Fabrication of 0.1 mu m gate aperture Mo-tip field-emitter arrays using interferometric lithography*, Applied Physics Letters **74** (20), 3050 (1999).

[9] I. J. Djomehri, T. A. Savas, and H. I. Smith, *Zone-plate-array lithography in the deep ultraviolet*, Journal of Vacuum Science & Technology B **16** (6), 3426 (1998).

[10] E. A. Dobisz, T. N. Fedynyshyn, D. Ma, L. M. Shirey, and R. Bass, *Electron-beam nanolithography, acid diffusion, and chemical kinetics in SAL-601*, Journal of Vacuum Science & Technology B **16** (6), 3773 (1998).

[11] M. Campbell, D. N. Sharp, M. T. Harrison, R. G. Denning, and A. J. Turberfield, *Fabrication of photonic crystals for the visible spectrum by holographic lithography*, Nature **404** (6773), 53 (2000).

[12] M. K. Herndon, R. T. Collins, R. E. Hollingsworth, P. R. Larson, and M. B. Johnson, *Near-field scanning optical nanolithography using amorphous silicon photoresists*, Applied Physics Letters **74** (1), 141 (1999).

[13] S. C. Minne, S. R. Manalis, A. Atalar, and C. F. Quate, *Independent parallel lithography using the atomic force microscope*, Journal of Vacuum Science & Technology B **14** (4), 2456 (1996).

[14] Cheolmin Park, Jongseung Yoon, and Edwin L. Thomas, *Enabling nanotechnology with self assembled block copolymer patterns*, Polymer **44** (22), 6725 (2003).

[15] K. Stratford, O. Henrich, J. S. Lintuvuori, M. E. Cates, and D. Marenduzzo, *Self-assembly of colloid-cholesteric composites provides a possible route to switchable optical materials*, Nature Communications **5** (2014).

[16] V. Uskokovic, *Theoretical and practical aspects of colloid science and self-assembly phenomena revisited*, Reviews in Chemical Engineering **23** (5), 301 (2007).

[17] K. C. Grabar, P. C. Smith, and M. J. Natan, *Kinetics and Thermodynamics of Gold Colloid Self-Assembly on Immobilized Polymers*, Abstracts of Papers of the American Chemical Society **209**, 39 (1995).

[18] Y. Zhang, D. C. Li, Y. P. Li, S. Zhang, M. Wang, and Y. Li, *High electric conductivity of liquid crystals formed by ordered self-assembly of nonionic surfactant N, N-bis(2-hydroxyethyl)dodecanamide in water*, Soft Matter **11** (9), 1762 (2015).

[19] S. A. Walker and J. A. Zasadzinski, *Self-assembly of silicate surfactant mesophases*, Advances in Porous Materials **371**, 93 (1995).

[20] C. J. Drummond, S. Albers, D. N. Furlong, and D. Wells, *Photocontrol of Surface-Activity and Self-Assembly with a Spirobenzopyran Surfactant*, Langmuir **7** (10), 2409 (1991).

[21] J. E. Brady and M. P. Turberg, *New Insights into Surfactant Self-Assembly*, Abstracts of Papers of the American Chemical Society **199**, 147 (1990).

[22] D. Han, Y. Park, H. Kim, and J. B. Lee, *Self-assembly of free-standing RNA membranes*, Nature Communications **5** (2014).

[23] Y. S. Velichko, J. R. Mantei, R. Bitton, D. Carvajal, K. R. Shull, and S. I. Stupp, *Electric Field Controlled Self-Assembly of Hierarchically Ordered Membranes*, Advanced Functional Materials **22** (2), 369 (2012).

[24] S. P. Jiang, Z. C. Liu, and Z. Q. Tian, *Layer-by-layer self-assembly of composite polyelectrolyte-nafion membranes for direct methanol fuel cells*, Advanced Materials **18** (8), 1068 (2006).

[25] Y. Ishikawa, H. Kuwahara, and T. Kunitake, *Self-Assembly of Bilayer-Membranes in Organic-Solvents by Novel Amphiphilic Compounds*, Journal of the American Chemical Society **111** (22), 8530 (1989).

[26] T. Vo, V. Venkatasubramanian, S. Kumar, B. Srinivasan, S. Pal, Y. G. Zhang, and O. Gang, *Stoichiometric control of DNA-grafted colloid self-assembly*, Proceedings of the National Academy of Sciences of the United States of America **112** (16), 4982 (2015).

[27] J. Ventura, S. J. Eron, D. C. Gonzalez-Toro, K. Raghupathi, F. Wang, J. A. Hardy, and S. Thayumanavan, *Reactive Self-Assembly of Polymers and Proteins to Reversibly Silence a Killer Protein*, Biomacromolecules **16** (10), 3161 (2015).

[28] W. C. Ruder, C. P. D. Hsu, B. D. Edelman, R. Schwartz, and P. R. LeDuc, *Biological colloid engineering: Self-assembly of dipolar ferromagnetic chains in a functionalized biogenic ferrofluid*, Applied Physics Letters **101** (6) (2012).

[29] R. J. Williams, A. P. Dove, and R. K. O'Reilly, *Self-assembly of cyclic polymers*, Polymer Chemistry **6** (16), 2998 (2015).

[30] S. Marpu, P. K. Upadhyay, D. T. Nguyen, I. W. H. Oswald, R. K. Arvapally, R. A. Petros, Z. B. Hu, and M. A. Omary, *Self-Assembly of Linear Polymers into Phosphorescent Nanoparticles: Optimization toward Non-Cytotoxic Bioimaging and Photonic Devices*, Journal of Physical Chemistry C **119** (22), 12551 (2015).

[31] D. L. Wang, G. S. Tong, R. J. Dong, Y. F. Zhou, J. Shen, and X. Y. Zhu, *Self-assembly of supramolecularly engineered polymers and their biomedical applications*, Chemical Communications **50** (81), 11994 (2014).

[32] M. Tirrell, *Electrostatic self-assembly of polymers and colloids: New routes to new functional materials*, Abstracts of Papers of the American Chemical Society **247** (2014).

[33] M. P. Stoykovich, H. Kang, KCh Daoulas, G. Liu, C. C. Liu, J. J. de Pablo, M. Muller, and P. F. Nealey, *Directed self-assembly of block copolymers for nanolithography: fabrication of isolated features and essential integrated circuit geometries*, ACS Nano **1** (3), 168 (2007).

[34] S. B. Darling, *Directing the self-assembly of block copolymers*, Progress in polymer science **32** (10), 1152 (2007).

[35] J. H. Park, K. H. Kim, Y. W. Park, J. P. F. Lagerwall, and G. Scalia, *Ultra long Ordered Nanowires from the Concerted Self-Assembly of Discotic Liquid Crystal and Solvent Molecules*, Langmuir **31** (34), 9432 (2015).

[36] Y. F. Lan, P. J. Huang, C. Y. Tsai, C. H. Lin, N. Sugiura, Y. Liu, D. M. Xu, and S. T. Wu, *Non-Ideal Optical Isotropy of Blue Phase Liquid Crystal and their Self-Assembly on Electrode Surface*, Molecular Crystals and Liquid Crystals **610** (1), 217 (2015).

[37] J. H. Kim, Y. H. Kim, H. S. Jeong, E. K. Youn, and H. T. Jung, *Highly ordered defect arrays of 8CB (4 '-n-octyl-4-cyano-biphenyl) liquid crystal via template-assisted self-assembly*, Journal of Materials Chemistry **21** (45), 18381 (2011).

[38] Bruno Zappone, Claire Meyer, Leonardo Bruno, and Emmanuelle Lacaze, *Periodic lattices of frustrated focal conic defect domains in smectic liquid crystal films*, Soft Matter **8** (16), 4318 (2012).

[39] Jean-Philippe Michel, Emmanuelle Lacaze, Michel Alba, Marc de Boissieu, Marc Gailhanou, and Michel Goldmann, *Optical gratings formed in thin smectic films frustrated on a single crystalline substrate*, Physical Review E **70** (1) (2004).

[40] Maurice Kleman and Oleg D. Lavrentovich, *Soft Matter Physics. An Introduction*. (Springer, 2003).

[41] Li Quan, *Nanoscience with Liquid Crystals*. (Springer International Publishing Switzerland 2014).

[42] C.T. O'Mahony, R.A. Farell, J.D. Holmes, and M.A. Morris, edited by Juan Carlos Moreno-Piraján (InTech, 2011).

[43] Chuang I., Durrer R., Turok N., and Yurke B., *Cosmology in the laboratory: defect dynamics in liquid crystals*, Science **251**, 1336 (1991).

[44] P. G. de Gennes and J. Prost, *The Physics of Liquid Crystals*. (Clarendon Press, 1995).

[45] Hirohisa Kawamoto, *The History of Liquid-Crystal Displays*, Proceedings of the IEEE **90** (4), 450 (2002).

[46] J. P. Cui, F. Zhou, Q. H. Wang, D. Wu, and D. H. Li, *Transflective Blue-Phase Liquid Crystal Display Using an Etched In-Plane Switching Structure*, Journal of Display Technology **7** (7), 398 (2011).

[47] H. C. Cheng, J. Yan, T. Ishinabe, N. Sugiura, C. Y. Liu, T. H. Huang, C. Y. Tsai, C. H. Lin, and S. T. Wu, *Blue-Phase Liquid Crystal Displays With Vertical Field Switching*, Journal of Display Technology **8** (2), 98 (2012).

[48] G. Kramer, C. S. Oh, and E. Joseph, *Liquid-Crystal Display System for Mass Audience Viewing*, Proceedings of the Society of Photo-Optical Instrumentation Engineers **526**, 113 (1985).

[49] C. T. Hsieh, C. H. Chang, C. Y. Lin, C. Y. Huang, C. J. Hsu, C. J. Tien, and K. Y. Lo, *Dual-View Blue Phase Liquid Crystal Display*, Journal of Display Technology **11** (7), 575 (2015).

[50] S. M. Garner, K. W. Wu, Y. C. Liao, J. W. Shiu, Y. S. Tsai, K. T. Chen, Y. C. Lai, C. C. Lai, Y. Z. Lee, J. C. Lin, X. H. Li, and P. Cimo, *Cholesteric Liquid Crystal Display With Flexible Glass Substrates*, Journal of Display Technology **9** (8), 644 (2013).

[51] S. Kumar, *Discotic liquid crystals for solar cells*, Current Science **82** (3), 256 (2002).

[52] I. C. Khoo, *Nonlinear Optical-Properties of Liquid-Crystals for Optical Imaging Processes*, Optical Engineering **25** (2), 198 (1986).

[53] K. Peddireddy, V. S. R. Jampani, S. Herminghaus, C. Bahr, M. Vitek, and I. Musevic, *Lasing and waveguiding in smectic A liquid crystal optical fibers*, Liquid Crystals Xviii **9182** (2014).

[54] M. Wahle and H. S. Kitzerow, *Liquid crystal assisted optical fibres*, Optics Express **22** (1), 262 (2014).

[55] M. Ghasemi and P. K. Choudhury, *Propagation through complex structured liquid crystal optical fibers*, Journal of Nanophotonics **8** (2014).

[56] P. K. Choudhury, *Liquid crystal optical fibers for sensing applications*, Nanostructured Thin Films Vi **8818** (2013).

[57] P. Mergo, J. Wojcik, B. Janoszczyk, and K. Poturaj, *Preparation of liquid crystal optical fibers*, Selected Papers from the International Conference on Optoelectronic Information Technologies **4425**, 298 (2000).

[58] A. d'Alessandro, L. Martini, L. Civita, R. Beccherelli, and R. Asquini, *Liquid crystal waveguide technologies for a new generation of low power photonic integrated circuits*, Emerging Liquid Crystal Technologies X **9384** (2015).

[59] D. X. Dai, J. Bauters, and J. E. Bowers, *Passive technologies for future large-scale photonic integrated circuits on silicon: polarization handling, light non-reciprocity and loss reduction*, Light-Science & Applications **1** (2012).

[60] F. R. Wang, Y. J. Liu, X. Q. Liu, and W. M. Sun, *Temperature and align effects on efficiency of cholesteric liquid crystal based laser*, High-Power Lasers and Applications Vi **8551** (2012).

[61] K. Mizutani, J. De Merlier, S. Sudo, K. Sato, and K. Kudo, *Liquid crystal mirror-based wavelength-tunable laser module with asynchronous mode cavity*, Ieee Photonics Technology Letters **18** (9-12), 1299 (2006).

[62] T. Matsui, R. Ozaki, K. Funamoto, M. Ozaki, and K. Yoshino, *Flexible mirrorless laser based on a free-standing film of photopolymerized cholesteric liquid crystal*, Applied Physics Letters **81** (20), 3741 (2002).

[63] L.M. Blinov and V.G. Chigrinov, *Electrooptic Effects in Liquid Crystal Materials*. (Springer, 1994).

[64] Ingo Dierking, *Texture of liquid crystal*. (WILEY-VCH Verlag GmbH & Co. KGaA, Weinheim, 2003).

[65] Yun Ho Kim, Dong Ki Yoon, Hyeon Su Jeong, Oleg D. Lavrentovich, and Hee-Tae Jung, *Smectic Liquid Crystal Defects for Self-Assembling of Building Blocks and Their Lithographic Applications*, Advanced Functional Materials **21** (4), 610 (2011).

[66] G. Friedel, *The mesomorphic states of matter*, Annales de Physique **18**, 273 (1922).

[67] J. B. Fournier and G. Durand, *Focal Conic Faceting in Smectic-a Liquid-Crystals*, Journal De Physique Ii **1** (7), 845 (1991).

[68] M. C. Choi, T. Pfohl, Z. Wen, Y. Li, M. W. Kim, J. N. Israelachvili, and C. R. Safinya, *Ordered patterns of liquid crystal toroidal defects by microchannel confinement*, Proc Natl Acad Sci U S A **101** (50), 17340 (2004).

[69] C. Blanc and M. Kleman, *The confinement of smectics with a strong anchoring*, European Physical Journal E **4** (2), 241 (2001).

[70] L. Z. Ruan, J. R. Sambles, and I. W. Stewart, *Self-Organized Periodic Photonic Structure in a Nonchiral Liquid Crystal*, Physical Review Letters **91** (3) (2003).

[71] M. Kleman and O. D. Lavrentovich, *Curvature energy of a focal conic domain with arbitrary eccentricity*, Physical Review E **61** (2), 1574 (2000).

[72] Yun Ho Kim, Dong Ki Yoon, Hyeon Su Jeong, and Hee-Tae Jung, *Self-assembled periodic liquid crystal defects array for soft lithographic template*, Soft Matter **6** (7), 1426 (2010).

[73] Yun Ho Kim, Hyeon Su Jeong, Jung Hyun Kim, Eun Kyoung Yoon, Dong Ki Yoon, and Hee-Tae Jung, *Fabrication of two-dimensional dimple and conical microlens arrays from a highly periodic toroidal-shaped liquid crystal defect array*, Journal of Materials Chemistry **20** (31), 6557 (2010).

[74] Bruno Zappone and Emmanuelle Lacaze, *Surface-frustrated periodic textures of smectic-Aliquid crystals on crystalline surfaces*, Physical Review E **78** (6) (2008).

[75] Bruno Zappone, Emmanuelle Lacaze, Habib Hayeb, Michel Goldmann, Nathalie Boudet, Philippe Barois, and Michel Alba, *Self-ordered arrays of linear defects and virtual singularities in thin smectic-A films*, Soft Matter **7** (3), 1161 (2011).

[76] D. Coursault, J. Grand, B. Zappone, H. Ayeb, G. Levi, N. Felidj, and E. Lacaze, *Linear self-assembly of nanoparticles within liquid crystal defect arrays*, Advanced Materials **24** (11), 1461 (2012).

[77] D. Coursault, B. Zappone, A. Coati, A. Boulaoued, L. Pelliser, D. Limagne, N. Boudet, B. H. Ibrahim, A. de Martino, M. Alba, M. Goldmann, Y. Garreau, B. Gallas, and E. Lacaze, *Self-organized arrays of dislocations in thin smectic liquid crystal films*, Soft Matter (2015).

[78] M. Andersson, V. Alfredsson, P. Kjellin, and A. E. C. Palmqvist, *Macroscopic alignment of silver nanoparticles in reverse hexagonal liquid crystalline templates*, Nano Letters **2** (12), 1403 (2002).

[79] N. R. Jana, L. Gearheart, and C. J. Murphy, *Seed-mediated growth approach for shape-controlled synthesis of spheroidal and rod-like gold nanoparticles using a surfactant template*, Advanced Materials **13** (18), 1389 (2001).

[80] Brandy Kinkead and Torsten Hegmann, *Effects of size, capping agent, and concentration of CdSe and CdTequantum dots doped into a nematic liquid crystal on the optical and electro-optic properties of the final colloidal liquid crystal mixture*, J. Mater. Chem. **20** (3), 448 (2010).

[81] S. Link and M. A. El-Sayed, *Spectral properties and relaxation dynamics of surface plasmon electronic oscillations in gold and silver nanodots and nanorods*, Journal of Physical Chemistry B **103** (40), 8410 (1999).

[82] U. Kreibig and L. Genzel, *Optical-Absorption of Small Metallic Particles*, Surface Science **156** (Jun), 678 (1985).

[83] M. Mitov, C. Portet, C. Bourgerette, E. Snoeck, and M. Verelst, *Long-range structuring of nanoparticles by mimicry of a cholesteric liquid crystal*, Nature materials **1** (4), 229 (2002).

[84] H. Stark, *Physics of colloidal dispersions in nematic liquid crystals*, Physics Reports-Review Section of Physics Letters **351** (6), 387 (2001).

[85] M. Zapotocky, L. Ramos, P. Poulin, T. C. Lubensky, and D. A. Weitz, *Particle-stabilized defect gel in cholesteric liquid crystals*, Science **283** (5399), 209 (1999).

[86] P. Poulin, H. Stark, T. C. Lubensky, and D. A. Weitz, *Novel colloidal interactions in anisotropic fluids*, Science **275** (5307), 1770 (1997).

[87] J. C. Loudet and P. Poulin, *Monodisperse aligned emulsions from demixing in bulk liquid crystals*, Colloid Chemistry 1 **226**, 173 (2003).

[88] H. Stark, J. Stelzer, and R. Bernhard, *Water droplets in a spherically confined nematic solvent: A numerical investigation*, European Physical Journal B **10** (3), 515 (1999).

[89] Mohamed Amine Gharbi, Maurizio Nobili, Martin In, Guillaume Prévot, Paolo Galatola, Jean-Baptiste Fournier, and Christophe Blanc, *Behavior of colloidal particles at a nematic liquid crystal interface†*, Soft Matter **7** (4), 1467 (2011).

[90] P. Kossyrev, M. Ravnik, and S. Zumer, *Branching of colloidal chains in capillary-confined nematics*, Physical Review Letters **96** (4) (2006).

[91] M. Ravnik, M. Skarabot, S. Zumer, U. Tkalec, I. Poberaj, D. Babic, N. Osterman, and I. Musevic, *Entangled nematic colloidal dimers and wires*, Physical Review Letters **99** (24) (2007).

[92] M. Skarabot, M. Ravnik, S. Zumer, U. Tkalec, I. Poberaj, D. Babic, N. Osterman, and I. Musevic, *Two-dimensional dipolar nematic colloidal crystals*, Physical Review E **76** (5) (2007).

[93] I. Musevic and M. Skarabot, *Self-assembly of nematic colloids*, Soft Matter **4** (2), 195 (2008).

[94] L. S. Hirst, J. Kirchhoff, R. Inman, and S. Ghosh, *Quantum dot self-assembly in liquid crystal media*, Emerging Liquid Crystal Technologies V **7618** (2010).

[95] Christophe Blanc, Delphine Coursault, and Emmanuelle Lacaze, *Ordering nano- and microparticles assemblies with liquid crystals*, Liquid Crystals Reviews **1** (2), 83 (2013).

[96] Javad Mirzaei, Mitya Reznikov, and Torsten Hegmann, *Quantum dots as liquid crystal dopants*, Journal of Materials Chemistry **22** (42), 22350 (2012).

[97] Umadevi Shivakumar, Javad Mirzaei, Xiang Feng, Anshul Sharma, Paulo Moreira, and Torsten Hegmann, *Nanoparticles: complex and multifaceted additives for liquid crystals*, Liquid Crystals **38** (11-12), 1495 (2011).

[98] D. Voloschenko, O. P. Pishnyak, S. V. Shiyanovskii, and O. D. Lavrentovich, *Effect of director distortions on morphologies of phase separation in liquid crystals*, Physical Review E **65** (6) (2002).

[99] K. Higashiguchi, K. Yasui, M. Ozawa, K. Odoi, and H. Kikuchi, *Spatial distribution control of polymer nanoparticles by liquid crystal disclinations*, Polymer Journal **44** (6), 632 (2012).

[100] Jonathan Milette, Stephen J. Cowling, Violeta Toader, Cyrille Lavigne, Isabel M. Saez, R. Bruce Lennox, John W. Goodby, and Linda Reven, *Reversible long range*

network formation in gold nanoparticle - nematic liquid crystal composites, Soft Matter **8** (1), 173 (2012).

[101] X. W. Zhang, D. Luo, Y. Li, M. Zhao, B. Han, M. T. Zhao, and H. T. Dai, *PbS nanoparticles stabilised blue phase liquid crystals*, Liquid Crystals **42** (9), 1257 (2015).

[102] Y. Shi, J. Mo, J. Wei, and J. B. Guo, *Chiral assembly and plasmonic response of silver nanoparticles in a three-dimensional blue-phase nanostructure template*, New Journal of Chemistry **39** (3), 1899 (2015).

[103] L. Wang, W. L. He, X. Xiao, F. U. Meng, Y. Zhang, P. Y. Yang, L. P. Wang, J. M. Xiao, H. Yang, and Y. F. Lu, *Hysteresis-Free Blue Phase Liquid-Crystal-Stabilized by ZnS Nanoparticles*, Small **8** (14), 2189 (2012).

[104] M. Trcek, G. Cordoyiannis, V. Tzitzios, S. Kralj, G. Nounesis, I. Lelidis, and Z. Kutnjak, *Nanoparticle-induced twist-grain boundary phase*, Phys Rev E Stat Nonlin Soft Matter Phys **90** (3), 032501 (2014).

[105] M. Lavric, G. Cordoyiannis, S. Kralj, V. Tzitzios, G. Nounesis, and Z. Kutnjak, *Effect of anisotropic MoS2 nanoparticles on the blue phase range of a chiral liquid crystal*, Applied Optics **52** (22), E47 (2013).

[106] G. Cordoyiannis, V. S. R. Jampani, S. Kralj, S. Dhara, V. Tzitzios, G. Basina, G. Nounesis, Z. Kutnjak, C. S. P. Tripathi, P. Losada-Perez, D. Jesenek, C. Glorieux, I. Musevic, A. Zidansek, H. Ameinitsch, and J. Thoen, *Different modulated structures of topological defects stabilized by adaptive targeting nanoparticles*, Soft Matter **9** (15), 3956 (2013).

[107] S. Yabu, Y. Tanaka, K. Tagashira, H. Yoshida, A. Fujii, H. Kikuchi, and M. Ozaki, *Polarization-independent refractive index tuning using gold nanoparticle-stabilized blue phase liquid crystals*, Optics Letters **36** (18), 3578 (2011).

[108] E. Karatairi, B. Rozic, Z. Kutnjak, V. Tzitzios, G. Nounesis, G. Cordoyiannis, J. Thoen, C. Glorieux, and S. Kralj, *Nanoparticle-induced widening of the temperature range of liquid-crystalline blue phases*, Physical Review E **81** (4) (2010).

[109] G. Cordoyiannis, P. Losada-Perez, C. S. P. Tripathi, B. Rozic, U. Tkalec, V. Tzitzios, E. Karatairi, G. Nounesis, Z. Kutnjak, I. Musevic, C. Glorieux, S. Kralj, and J. Thoen, *Blue phase III widening in CE6-dispersed surface-functionalised CdSe nanoparticles*, Liquid Crystals **37** (11), 1419 (2010).

[110] H. Yoshida, Y. Tanaka, K. Kawamoto, H. Kubo, T. Tsuda, A. Fujii, S. Kuwabata, H. Kikuchi, and M. Ozaki, *Nanoparticle-Stabilized Cholesteric Blue Phases*, Applied Physics Express **2** (12) (2009).

[111] D. K. Yoon, M. C. Choi, Y. H. Kim, M. W. Kim, O. D. Lavrentovich, and H. T. Jung, *Internal structure visualization and lithographic use of periodic toroidal holes in liquid crystals*, Nature materials **6** (11), 866 (2007).

[112] Laurent Pelliser, Mathieu Manceau, Clotilde Lethiec, Delphine Coursault, Stefano Vezzoli, Godefroy Leménager, Laurent Coolen, Massimo DeVittorio, Ferruccio Pisanello, Luigi Carbone, Agnes Maitre, Alberto Bramati, and Emmanuelle Lacaze, *Alignment of Rod-Shaped Single-Photon Emitters Driven by Line Defects in Liquid Crystals*, Advanced Functional Materials **25** (11), 1719 (2015).

[113] Iryna Gryn, Emmanuelle Lacaze, Roberto Bartolino, and Bruno Zappone, *Controlling the Self-Assembly of Periodic Defect Patterns in Smectic Liquid Crystal Films with Electric Fields*, Advanced Functional Materials **25** (1), 142 (2015).

[114] Liquid crystal. Wikipedia, *https://en.wikipedia.org/wiki/Liquid_crystal#Nematic_phase*.

[115] A. S. Sonin, *Introduction to the physics of liquid crystals*. (Science Publ., Moscow, 1983).

[116] C. W. Oseen, *The theory of liquid crystals*, Trans. Faraday Soc. **29** (140), 883 (1933).

[117] F. C. Frank, *Liquid crystals. On the theory of liquid crystals*, Discuss. Faraday Soc. **25**, 19 (1958).

[118] M. J. Bradshaw, E. P. Raynes, J. D. Bunning, and T. E. Faber, *The Frank constants of some nematic liquid crystals*, Journal de Physique **46** (9), 1513 (1985).

[119] P. G. De Gennes, *An analogy between superconductors and smectics A*, Solid State Communications **10** (9), 753 (1972).

[120] M. Benzekri, T. Claverie, J. P. Marcerou, and J. C. Rouillon, *Nonvanishing of the layer compressional elastic constant at the smetic-A-to-nematic phase transition: A consequence of Landau-Peierls instability?*, Physical Review Letters **68** (16), 2480 (1992).

[121] J. W. Goodby, M. A. Waugh, S. M. Stein, E. Chin, R. Pindak, and J. S. Patel, *Characterization of a new helical smectic liquid crystal*, Nature **337** (6206), 449 (1989).

[122] R. Stannarius, *Diamagnetic properties of liquid crystals in Handbook of Liquid Crystals*. (1998).

[123] J. Friedel and M. Kleman, *Fundamental Aspects of Dislocation Theory*. (US Government Printing Office, Washington, 1970), p.607.

[124] P. Oswald and P. Pieranski, *Smectic and columnar liquid crystals: concepts and physical properties illustrated by experiments*. (CRC press, 2005).

[125] L. M. Blinov, *Structure and Properties of Liquid Crystals*. (Springer Netherlands, 2011), p.439.

[126] P. Oswald and P. Pieranski, *Nematic and cholesteric liquid crystals: concepts and physical properties illustrated by experiments*. (Taylor & Francis London, 2005).

[127] R. B. Meyer, B. Stebler, and S. T. Lagerwall, *Observation of edge dislocations in smectic liquid crystals*, Physical Review Letters **41** (20), 1393 (1978).

[128] M. Ambrožič, S. Kralj, T. J. Sluckin, S. Žumer, and D. Svenšek, *Annihilation of edge dislocations in smectic-A liquid crystals*, Physical Review E **70** (5), 051704 (2004).

[129] C. E. Williams and M. Kleman, *Dislocations, grain boundaries and focal conics in smectics A*, Le Journal de Physique Colloques **36** (C1), C1 (1975).

[130] K. J. Ihn, J. A. N. Zasadzinski, R. Pindak, A. J. Slaney, and J. Goodby, *Observations of the liquid-crystal analog of the Abrikosov phase* Science **258** (5080), 275 (1992).

[131] I. Dierking, *A review of textures of the TGBA* phase under different anchoring geometries*, Liquid Crystals **23** (1), 83 (1999).

[132] L. M. Blinov, *Structure and properties of liquid crystals*. (Springer Science & Business Media, 2010).

[133] M. Kleman, *Defects in Liquid-Crystals*, Reports on Progress in Physics **52** (5), 555 (1989).

[134] W. K. Schief, M. Kleman, and C. Rogers, *On a nonlinear elastic shell system in liquid crystal theory: generalized Willmore surfaces and Dupin cyclides*, Proceedings of the Royal Society a-Mathematical Physical and Engineering Sciences **461** (2061), 2817 (2005).

[135] G. Friedel, *The mesomorphic states of matter*, Annales de Physique **18**, 273 (1922).

[136] M. Kléman and O. D. Laverntovich, *Soft Matter Physics. An Introduction*. (Springer Science & Business Media, 2003).

[137] M. Kleman, *Points, lines and walls in liquid crystals, magnetic systems and various ordered media*. (Wiley, New York, 1983).

[138] Joseph A. Castellano, *Surface Anchoring of Liquid Crystal Molecules on Various Substrates*, Molecular Crystals and Liquid Crystals **94** (1-2), 33 (1983).

[139] Jong-Ho Son and Wang-Cheol Zin, *Effects of alignment layer thickness on the pretilt angle of liquid crystals*, Applied Physics Letters **97** (24), 243306 (2010).

[140] Noel A. Clark, *Surface memory effects in liquid crystals: Influence of surface composition*, Physical Review Letters **55** (3), 292 (1985).

[141] A. Rapini and M. Papoular, *Distorsion d'une lamelle nématique sous champ magnétique conditions d'ancrage aux parois*, Le Journal de Physique Colloques **30** (C4), C4 (1969).

[142] G. Durand, *Recent advances in nematic and smectic A anchoring on amorphous solid surfaces*, Liquid Crystals **14** (1), 159 (1993).

[143] I. Lelidis and G. Durand, *Electrically-Induced Isotropic-Nematic-Smectic-a Phase-Transitions in Thermotropic Liquid-Crystals (Vol 73, Pg 672, 1994)*, Physical Review Letters **73** (16), 2277 (1994).

[144] Iain W. Stewart, *The static and dynamic theory of liquid crystals. A mathematical introduction*. (Taylor and Francis, New York, 2004).

[145] Hao Qi and Torsten Hegmann, *Liquid crystal–gold nanoparticle composites*, Liquid Crystals Today **20** (4), 102 (2011).

[146] Javad Mirzaei, Martin Urbanski, Kui Yu, Heinz- S. Kitzerow, and Torsten Hegmann, *Nanocomposites of a nematic liquid crystal doped with magic-sized CdSe quantum dots*, Journal of Materials Chemistry **21** (34), 12710 (2011).

[147] Martin Urbanski, Brandy Kinkead, Torsten Hegmann, and Heinz- S. Kitzerow, *Director field of birefringent stripes in liquid crystal/nanoparticle dispersions*, Liquid Crystals **37** (9), 1151 (2010).

[148] C. E. Williams and M. Kleman, *Dislocations, Grain Boundaries and Focal Conics in Smectics A*, Le Journal de Physique Colloques **36** (C1), C1 (1975).

[149] K. Abe, A. Usami, K. Ishida, Y. Fukushima, and T. Shigenari, *Dielectric and fluorescence study on phase transitions in liquid crystal 5CB and 8CB*, Journal of the Korean Physical Society **46** (1), 220 (2005).

[150] Theo Rasing and Igor Musevic, *Surfaces and Interfaces of Liquid Crystals*. (Springer Science & Business Media, 2013).

[151] R. G. Horn, *Refractive indices and order parameters of two liquid crystals*, Journal de Physique **39** (1), 105 (1978).

[152] Ranjini Bandyopadhyay, Dennis Liang, Ralph H. Colby, James L. Harden, and Robert L. Leheny, *Enhanced Elasticity and Soft Glassy Rheology of a Smectic in a Random Porous Environment*, Physical Review Letters **94** (10) (2005).

[153] A. J. Leadbetter, J. C. Frost, J. P. Gaughan, G. W. Gray, and A. Mosley, *The structure of smectic A phases of compounds with cyano end groups*, Journal de Physique **40** (4), 375 (1979).

[154] J. H. Lee, J. H. Kim, and S. D. Lee, *Dynamics of polarization reversal in the surface layer of ferroelectric liquid crystals*, Journal of the Korean Physical Society **32**, S1056 (1998).

[155] J. C. Loudet, P. V. Dolganov, P. Patrício, H. Saadaoui, and P. Cluzeau, *Undulation Instabilities in the Meniscus of Smectic Membranes*, Physical Review Letters **106** (11) (2011).

[156] Ruibo Lu, Shin-Tson Wu, and Keshu Xu, *Fabrication of Surface-Stabilized Ferroelectric Liquid Crystal Display with Stripe-Shaped Domain Structure*, Japanese Journal of Applied Physics **42** (Part 1, No. 4A), 1628 (2003).

[157] I. I. Smalyukh, S. V. Shiyanovskii, and O. D. Lavrentovich, *Three-dimensional imaging of orientational order by fluorescence confocal polarizing microscopy*, Chemical Physics Letters **336** (1-2), 88 (2001).

[158] O. D. Lavrentovich, *Fluorescence confocal polarizing microscopy: Three-dimensional imaging of the director*, Pramana-Journal of Physics **61** (2), 373 (2003).

[159] D. Sun, H. J. Sue, and N. Miyatake, *Optical Properties of ZnO Quantum Dots in Epoxy with Controlled Dispersion*, Journal of Physical Chemistry C **112** (41), 16002 (2008).

[160] V. Myroshnychenko, J. Rodriguez-Fernandez, I. Pastoriza-Santos, A. M. Funston, C. Novo, P. Mulvaney, L. M. Liz-Marzan, and F. J. G. de Abajo, *Modelling the optical response of gold nanoparticles*, Chemical Society Reviews **37** (9), 1792 (2008).

[161] D. Coursault, B. H. Ibrahim, L. Pelliser, B. Zappone, A. de Martino, E. Lacaze, and B. Gallas, *Modeling the optical properties of self-organized arrays of liquid crystal defects*, Optics Express **22** (19), 23182 (2014).

[162] H. Tajalli, A. Ghanadzadeh Gilani, M. S. Zakerhamidi, and P. Tajalli, *The photophysical properties of Nile red and Nile blue in ordered anisotropic media*, Dyes and Pigments **78** (1), 15 (2008).

[163] R. Saxena, S. Shrivastava, S. Haldar, A. S. Klymchenko, and A. Chattopadhyay, *Location, dynamics and solvent relaxation of a Nile Red-based phase-sensitive fluorescent membrane probe*, Chem Phys Lipids **183**, 1 (2014).

[164] G.A. Reynolds and k.H. Drexhage, *New coumarin dyes with rigidized structure for flashlamp-pumped dye lasers*, Optics Communications **13** (3), 222 (1975).

[165] Nobutaka Tanigaki, Claire Heck, Toshiko Mizokuro, Hideyuki Minato, Masahiro Misaki, Yuji Yoshida, and Reiko Azumi, *Doped-Dye Orientation Relative to Oriented Polyfluorene Host Film*, Japanese Journal of Applied Physics **47** (1), 416 (2008).

[166] J. L. Meinershagen and T. Bein, *Optical sensing in nanopores. Encapsulation of the solvatochromic dye Nile red in zeolites*, Journal of the American Chemical Society **121** (2), 448 (1999).

[167] D. L. Sackett and J. Wolff, *Nile Red as a Polarity-Sensitive Fluorescent-Probe of Hydrophobic Protein Surfaces*, Analytical Biochemistry **167** (2), 228 (1987).

[168] Kjeld Pedersen, *Quantum size effects in nanostructures*. (Aalborg University, Aalborg, 2006).

[169] V. Biju, T. Itoh, A. Anas, A. Sujith, and M. Ishikawa, *Semiconductor quantum dots and metal nanoparticles: syntheses, optical properties, and biological applications*, Analytical and Bioanalytical Chemistry **391** (7), 2469 (2008).

[170] Louis Brus, *Zero-Dimensional ' 'Excitons' ' in Semiconductor Clusters*, IEEE Journal of quantum electronics **QE-22** (9), 1909 (1986).

[171] L. E. Brus, *Electron–electron and electron-hole interactions in small semiconductor crystallites: The size dependence of the lowest excited electronic state*, The Journal of Chemical Physics **80** (9), 4403 (1984).

[172] A. L. Efros and M. Rosen, *Random telegraph signal in the photoluminescence intensity of a single quantum dot*, Physical Review Letters **78** (6), 1110 (1997).

[173] S. Hohng and T. Ha, *Near-complete suppression of quantum dot blinking in ambient conditions*, Journal of the American Chemical Society **126** (5), 1324 (2004).

[174] V. Fomenko and D. J. Nesbitt, *Solution control of radiative and nonradiative lifetimes: A novel contribution to quantum dot blinking suppression*, Nano Letters **8** (1), 287 (2008).

[175] B. Mahler, P. Spinicelli, S. Buil, X. Quelin, J. P. Hermier, and B. Dubertret, *Towards non-blinking colloidal quantum dots*, Nature materials **7** (8), 659 (2008).

[176] L. Manna, E. C. Scher, and A. P. Alivisatos, *Synthesis of soluble and processable rod-, arrow-, teardrop-, and tetrapod-shaped CdSe nanocrystals*, Journal of the American Chemical Society **122** (51), 12700 (2000).

[177] Xiao-Yong Wang, Jia-Yu Zhang, A. Nazzal, M. Darragh, and Min Xiao, *Electronic structure transformation from a quantum-dot to a quantum-wire system: Photoluminescence decay and polarization of colloidal CdSe quantum rods*, Applied Physics Letters **81** (25), 4829 (2002).

[178] H. Htoon, J. A. Hollingworth, A. V. Malko, R. Dickerson, and V. I. Klimov, *Light amplification in semiconductor nanocrystals: Quantum rods versus quantum dots*, Applied Physics Letters **82** (26), 4776 (2003).

[179] L. Carbone, C. Nobile, M. De Giorgi, F. D. Sala, G. Morello, P. Pompa, M. Hytch, E. Snoeck, A. Fiore, I. R. Franchini, M. Nadasan, A. F. Silvestre, L. Chiodo, S. Kudera, R. Cingolani, R. Krahne, and L. Manna, *Synthesis and micrometer-scale assembly of colloidal CdSe/CdS nanorods prepared by a seeded growth approach*, Nano Letters **7** (10), 2942 (2007).

[180] F. Pisanello, G. Lemenager, L. Martiradonna, L. Carbone, S. Vezzoli, P. Desfonds, P. D. Cozzoli, J. P. Hermier, E. Giacobino, R. Cingolani, M. De Vittorio, and A. Bramati, *Non-blinking single-photon generation with anisotropic colloidal nanocrystals: towards room-temperature, efficient, colloidal quantum sources*, Advanced Materials **25** (14), 1974 (2013).

[181] J. Perezjuste, I. Pastorizasantos, L. Lizmarzan, and P. Mulvaney, *Gold nanorods: Synthesis, characterization and applications*, Coordination Chemistry Reviews **249** (17-18), 1870 (2005).

[182] Liang-Chy Chien, Hao Qi, Brandy Kinkead, and Torsten Hegmann, *Effects of functionalized metal and semiconductor nanoparticles in nematic liquid crystal phases*, **6911**, 691106 (2008).

[183] Hao Qi and Torsten Hegmann, *Impact of nanoscale particles and carbon nanotubes on current and future generations of liquid crystal displays*, Journal of Materials Chemistry **18** (28), 3288 (2008).

[184] Torsten Hegmann, Hao Qi, and Vanessa M. Marx, *Nanoparticles in Liquid Crystals: Synthesis, Self-Assembly, Defect Formation and Potential Applications*, Journal of Inorganic and Organometallic Polymers and Materials **17** (3), 483 (2007).

[185] Q. Liu, Y. Cui, D. Gardner, X. Li, S. He, and Smalyukh, II, *Self-alignment of plasmonic gold nanorods in reconfigurable anisotropic fluids for tunable bulk metamaterial applications*, Nano Letters **10** (4), 1347 (2010).

[186] K. A. Willets and R. P. Van Duyne, *Localized surface plasmon resonance spectroscopy and sensing*, Annu Rev Phys Chem **58**, 267 (2007).

[187] B. Jerome, *Surface Effects and Anchoring in Liquid-Crystals*, Reports on Progress in Physics **54** (3), 391 (1991).

[188] M. Shigeno, W. Mizutani, M. Suginoya, M. Ohmi, K. Kajimura, and M. Ono, *Observation of Liquid-Crystals on Graphite by Scanning Tunneling Microscopy*, Japanese Journal of Applied Physics Part 2-Letters **29** (1), L119 (1990).

[189] Seung-Ho Lee, Jong-Ho Son, Wang-Cheol Zin, Seung Hee Lee, and Jang-Kun Song, *Self-constructed stable liquid crystal alignment in a monomer-liquid crystal mixture system*, Liquid Crystals **39** (9), 1049 (2012).

[190] Norland Products Incorporate NOA 61, *https://www.norlandprod.com/adhesives/noa%2061.html*.

[191] I. I. Smalyukh and O. D. Lavrentovich, *Three-dimensional director structures of defects in Grandjean-Cano wedges of cholesteric liquid crystals studied by fluorescence confocal polarizing microscopy*, Physical Review E **66** (5) (2002).

[192] Carl Zeiss website, *http://zeiss-campus.magnet.fsu.edu/tutorials/index.html*.

[193] Benjamin T. Diroll, Adriel Koschitzky, and Christopher B. Murray, *Tunable Optical Anisotropy of Seeded CdSe/CdS Nanorods*, The Journal of Physical Chemistry Letters **5** (1), 85 (2014).

[194] Dark-field microscopy JIC, *https://www.jic.ac.uk/microscopy/more/T5_2.htm*.

[195] A. Honglawan, D. A. Beller, M. Cavallaro, R. D. Kamien, K. J. Stebe, and S. Yang, *Topographically induced hierarchical assembly and geometrical transformation of focal conic domain arrays in smectic liquid crystals*, Proceedings of the National Academy of Sciences of the United States of America **110** (1), 34 (2013).

[196] D. K. Yoon, M. C. Choi, Y. H. Kim, M. W. Kim, O. D. Lavrentovich, and H. T. Jung, *Internal structure visualization and lithographic use of periodic toroidal holes in liquid crystals*, Nature materials **6** (11), 866 (2007).

[197] J. B. Fournier, *Curvature elasticity of smectic-Atextures with virtual surface singularities*, Physical Review Letters **70** (10), 1445 (1993).

[198] Emmanuelle Lacaze, Jean-Philippe Michel, Michel Alba, and Michel Goldmann, *Planar anchoring and surface melting in the smectic-Aphase*, Physical Review E **76** (4) (2007).

[199] Wei Guo and Christian Bahr, *Influence of phase sequence on focal conic domains in smectic films*, Physical Review E **79** (6) (2009).

[200] P. E. Cladis and S. Torza, *Growth of a smectic A from a bent nematic phase and the smectic light valve*, Journal of Applied Physics **46** (2), 584 (1975).

[201] Jean-Philippe Michel, Emmanuelle Lacaze, Michel Goldmann, Marc Gailhanou, Marc de Boissieu, and Michel Alba, *Structure of Smectic Defect Cores: X-Ray Study of 8CB Liquid Crystal Ultrathin Films*, Physical Review Letters **96** (2) (2006).

[202] O. P. Pishnyak, Yu A. Nastishin, and O. D. Lavrentovich, *Comment on "Self-Organized Periodic Photonic Structure in a Nonchiral Liquid Crystal"*, Physical Review Letters **93** (10) (2004).

[203] G. Barbero and M. Meuti, *Influence of flexoelectricity on the stable configuration of a nematic layer with opposite boundary conditions*, Journal de Physique **47** (2), 341 (1986).

[204] A. Mazzulla, F. Ciuchi, and J. R. Sambles, *Optical determination of flexoelectric coefficients and surface polarization in a hybrid aligned nematic cell*, Physical Review E **64** (2) (2001).

[205] Nasser Mohieddin Abukhdeir and Alejandro D. Rey, *Defect kinetics and dynamics of pattern coarsening in a two-dimensional smectic-A system*, New Journal of Physics **10** (6), 063025 (2008).

[206] Chester Liu and M. Muthukumar, *Annihilation kinetics of liquid crystal defects*, The Journal of Chemical Physics **106** (18), 7822 (1997).

[207] C. Harrison, D. H. Adamson, Z. D. Cheng, J. M. Sebastian, S. Sethuraman, D. A. Huse, R. A. Register, and P. M. Chaikin, *Mechanisms of ordering in striped patterns*, Science **290** (5496), 1558 (2000).

[208] Christopher Harrison, Zhengdong Cheng, Srinivasan Sethuraman, David A. Huse, Paul M. Chaikin, Daniel A. Vega, John M. Sebastian, Richard A. Register, and Douglas H. Adamson, *Dynamics of pattern coarsening in a two-dimensional smectic system*, Physical Review E **66** (1) (2002).

[209] D. Coates, *Handbook of Liquid Crystals*. (Wiley-VCH, Weinheim, 1998).

[210] W. Guo, S. Herminghaus, and C. Bahr, *Controlling smectic focal conic domains by substrate patterning*, Langmuir **24** (15), 8174 (2008).

[211] K. Sun, Z. Y. Xiao, S. R. Lu, W. Zajaczkowski, W. Pisula, E. Hanssen, J. M. White, R. M. Williamson, J. Subbiah, J. Y. Ouyang, A. B. Holmes, W. W. H. Wong, and D. J. Jones, *A molecular nematic liquid crystalline material for high-performance organic photovoltaics*, Nature Communications **6** (2015).

[212] C. Bowman and A. C. Newell, *Natural patterns and wavelets*, Reviews of Modern Physics **70** (1), 13 (1998).

[213] Bo Li, Yan-Ping Cao, Xi-Qiao Feng, and Huajian Gao, *Mechanics of morphological instabilities and surface wrinkling in soft materials: a review*, Soft Matter **8** (21), 5728 (2012).

[214] A. Mesaros, K. Fujita, H. Eisaki, S. Uchida, J. C. Davis, S. Sachdev, J. Zaanen, M. J. Lawler, and E. A. Kim, *Topological Defects Coupling Smectic Modulations to Intra-Unit-Cell Nematicity in Cuprates*, Science **333** (6041), 426 (2011).

[215] B. Zappone, P. Richetti, R. Barberi, R. Bartolino, and H. T. Nguyen, *Forces in nematic liquid crystals constrained to the nanometer scale under hybrid anchoring conditions*, Phys Rev E Stat Nonlin Soft Matter Phys **71** (4 Pt 1), 041703 (2005).

[216] J. F. Annett, *Superconductivity, superfluids and condensates*. (Cambridge Press, 2004).

[217] P.G. de Gennes, *Superconductivity in metal and alloys*. (Westview Press, 1996).

[218] R. Wang, I. M. Syed, G. Carbone, R. G. Petschek, and C. Rosenblatt, *Bend-induced melting of the smectic-A phase: analogy to a type-I superconductor*, Physical Review Letters **97** (16), 167802 (2006).

[219] N. Gheorghiu, I. I. Smalyukh, O. D. Lavrentovich, and J. T. Gleeson, *Three-dimensional imaging of dielectric patterns in electrohydrodynamic convection of a nematic liquid crystal*, Physical Review E **74** (4) (2006).

[220] M. Kaczmarek, O. Buchnev, and I. Nandhakumar, *Ferroelectric nanoparticles in low refractive index liquid crystals for strong electro-optic response*, Applied Physics Letters **92** (10) (2008).

[221] L. M. Lopatina and J. V. Selinger, *Maier-Saupe-type theory of ferroelectric nanoparticles in nematic liquid crystals*, Phys Rev E Stat Nonlin Soft Matter Phys **84** (4 Pt 1), 041703 (2011).

[222] Maxim V. Gorkunov and Mikhail A. Osipov, *Mean-field theory of a nematic liquid crystal doped with anisotropic nanoparticles*, Soft Matter **7** (9), 4348 (2011).

[223] Qingkun Liu, Jianwei Tang, Yuan Zhang, Angel Martinez, Shaowei Wang, Sailing He, Timothy J. White, and Ivan I. Smalyukh, *Shape-dependent dispersion and alignment of nonaggregating plasmonic gold nanoparticles in lyotropic and thermotropic liquid crystals*, Physical Review E **89** (5) (2014).

[224] Dennis F. Gardner, Julian S. Evans, and Ivan I. Smalyukh, *Towards Reconfigurable Optical Metamaterials: Colloidal Nanoparticle Self-Assembly and Self-Alignment in Liquid Crystals*, Molecular Crystals and Liquid Crystals **545** (1), 3/[1227] (2011).

[225] L. M. Lopatina and J. V. Selinger, *Theory of Ferroelectric Nanoparticles in Nematic Liquid Crystals*, Physical Review Letters **102** (19) (2009).

[226] M. A. Osipov and M. V. Gorkunov, *Effect of nanoparticle chain formation on dielectric anisotropy of nematic composites*, Physical Review E **92** (3) (2015).

[227] H. Kikuchi, M. Yokota, Y. Hisakado, H. Yang, and T. Kajiyama, *Polymer-stabilized liquid crystal blue phases*, Nature materials **1** (1), 64 (2002).

[228] X. Wang, D. S. Miller, E. Bukusoglu, J. J. de Pablo, and N. L. Abbott, *Topological defects in liquid crystals as templates for molecular self-assembly*, Nature materials **doi:10.1038/nmat4421** (2015).

[229] A. Nych, U. Ognysta, M. Skarabot, M. Ravnik, S. Zumer, and I. Musevic, *Assembly and control of 3D nematic dipolar colloidal crystals*, Nature Communications **4** (2013).

[230] A. P. Alivisatos, *Semiconductor clusters, nanocrystals, and quantum dots*, Science **271** (5251), 933 (1996).

[231] I. Hadar, G. B. Hitin, A. Sitt, A. Faust, and U. Banin, *Polarization Properties of Semiconductor Nanorod Heterostructures: From Single Particles to the Ensemble*, Journal of Physical Chemistry Letters **4** (3), 502 (2013).

[232] K. G. Thomas, S. Barazzouk, B. I. Ipe, S. T. S. Joseph, and P. V. Kamat, *Uniaxial plasmon coupling through longitudinal self-assembly of gold nanorods*, Journal of Physical Chemistry B **108** (35), 13066 (2004).

[233] T. Wang, J. Q. Zhuang, J. Lynch, O. Chen, Z. L. Wang, X. R. Wang, D. LaMontagne, H. M. Wu, Z. W. Wang, and Y. C. Cao, *Self-Assembled Colloidal Superparticles from Nanorods*, Science **338** (6105), 358 (2012).

[234] C. T. Black, C. B. Murray, R. L. Sandstrom, and S. H. Sun, *Spin-dependent tunneling in self-assembled cobalt-nanocrystal superlattices*, Science **290** (5494), 1131 (2000).

[235] J. J. Urban, D. V. Talapin, E. V. Shevchenko, C. R. Kagan, and C. B. Murray, *Synergism in binary nanocrystal superlattices leads to enhanced p-type conductivity in self-assembled PbTe/Ag2 Te thin films*, Nature materials **6** (2), 115 (2007).

[236] L. S. Li and A. P. Alivisatos, *Origin and scaling of the permanent dipole moment in CdSe nanorods*, Physical Review Letters **90** (9), 097402 (2003).

[237] Thomas Nann and Jürgen Schneider, *Origin of permanent electric dipole moments in wurtzite nanocrystals*, Chemical Physics Letters **384** (1-3), 150 (2004).

[238] A. Kawski, P. Bojarski, and B. Kuklinski, *Estimation of ground- and excited-state dipole moments of Nile Red dye from solvatochromic effect on absorption and fluorescence spectra*, Chemical Physics Letters **463** (4-6), 410 (2008).

[239] K. Peddireddy, V. S. R. Jampani, S. Thutupalli, S. Herminghaus, C. Bahr, and I. Musevic, *Lasing and waveguiding in smectic A liquid crystal optical fibers*, Optics Express **21** (25), 30233 (2013).

[240] K. Peddireddy, P. Kumar, S. Thutupalli, S. Herminghaus, and C. Bahr, *Myelin Structures Formed by Thermotropic Smectic Liquid Crystals*, Langmuir **29** (50), 15682 (2013).

[241] J. B. Fournier, *Curvature Elasticity of Smectic-a Textures with Virtual Surface Singularities*, Physical Review Letters **70** (10), 1445 (1993).

[242] P. G. De Gennes and J. Prost, *The Physics of Liquid Crystals (2nd Ed.)*, Oxford University Press ed. (Oxford, 1993).

[243] D. Voloschenko, O. P. Pishnyak, S. V. Shiyanovskii, and O. D. Lavrentovich, *Effect of director distortions on morphologies of phase separation in liquid crystals*, Phys Rev E Stat Nonlin Soft Matter Phys **65** (6 Pt 1), 060701 (2002).

[244] Blach J-F, Henninot J-F, Coursault D, and M. Warenghem, Private communication.

[245] Delphine Coursault, UPMC, 2013.

[246] D. Coursault, J. F. Blach, J. Grand, A. Coati, A. Vlad, B. Zappone, D. Babonneau, G. Levi, N. Felidj, B. Donnio, J. L. Gallani, M. Alba, Y. Garreau, Y. Borensztein, M. Goldmann, and E. Lacaze, *Tailoring Anisotropic Interactions between Soft Nanospheres Using Dense Arrays of Smectic Liquid Crystal Edge Dislocations*, ACS Nano (2015).